Summer 2009

An experimental and numerical investigation of flapping and plunging wings

Taylor A. Swanson

Department: Mechanical and Aerospace Engineering

AN EXPERIMENTAL AND NUMERICAL INVESTIGATION OF FLAPPING AND PLUNGING WINGS

by

TAYLOR ALEXANDER SWANSON

A DISSERTATION

Presented to the Faculty of the Graduate School of the

MISSOURI UNIVERSITY OF SCIENCE AND TECHNOLOGY

In Partial Fulfillment of the Requirements for the Degree

DOCTOR OF PHILOSOPHY

in

AEROSPACE ENGINEERING

2009

Approved by

K. M. Isaac, Advisor
David W. Riggins
Fathi Finaish
Darryl J. Alofs
Parthasakha Neogi

ABSTRACT

Micro air vehicles, or MAVs, are of current interest for a multitude of uses to which they, being small, unmanned vehicles, are uniquely suited. Among the proposed uses are exploration, reconnaissance, and communications. They can be deployed inside buildings, where their small size, hovering capability, and maneuverability, are important factors. Due to their small size, they operate at low Reynolds numbers where conventional flying mechanisms are not advantageous. Thus, attempts have been made to learn from natural flyers like insects and birds. Natural flight is accomplished by flapping wings, and this idea has been proposed for certain types of MAVs termed ornithopters and entomopters. This dissertation investigates the aerodynamics applicable to low Reynolds number unsteady flow, and consists of four stages. The first stage is CFD for fixed wings at low Reynolds number. In the second and third stage, experiments are conducted on flapping and plunging wings. The final stage consists of dynamic mesh CFD for a plunging airfoil. The major findings for stage one are the force peak at 20^{o} angle of attack for fixed wings at a Reynolds number of 500, and the prominent leading edge vortex in a highly three-dimensional flow. The experiments revealed vortex shedding and a wake which creates force in the direction opposite to that of the wake. The fourth stage revealed the lift to drag ratio advantage of the leading edge trailing edge switching hovering mode compared to standard hovering mode, and camber was most effective at low reduced frequency (in the range of 0.5 to 2) and large Reynolds number (in the range of 100 to 2,500). Two vortices shed from each edge dominate the flow field in this hovering mode. Reduced frequency was the most dominant independent variable in both the experiments and dynamic mesh CFD.

ACKNOWLEDGMENTS

I wish to thank my advisor, Dr. Isaac, for helping and guiding me in my research these past few years. I also wish to thank the Department of Mechanical and Aerospace Engineering for funding me as a teaching assistant, and the Chancellor's office and the NASA Missouri Space Grant for providing me with fellowships.

The members of my committee deserve recognition for their invaluable insight and assistance over the years.

My family has supported me and encouraged my academic pursuits. The present work would not have been possible without them.

TABLE OF CONTENTS

LIST OF ILLUSTRATIONS

LIST OF TABLES

1. MOTIVATION

Aircraft come in a wide variety, ranging from the large, transcontinental jumbo jets to small, hand held micro aerial vehicles, or MAVs. They range in speed from Mach three for the SR-71 to zero miles per hour for a hovering MAV. This cornucopia of vehicles can assume many disparate roles according to their speed, size, maneuverability, or other salient characteristics.

Micro aerial vehicles possess many such unique characteristics. They are small, difficult to detect, highly maneuverable, and some can hover. This combination of characteristics makes they well suited to perform various duties, including reconnaissance and exploration, thus suiting the needs of the military and NASA. The military can utilize these in the war on terror to investigate remote and dangerous locales while the soldiers remain a safe distance away, relay communications, and detect chemical and biological weapons (see references [36], [106], [26], and [176]). NASA, with its renewed interest in lunar and Martian exploration, can utilize such vehicles to observe the Martian atmosphere and photograph its surface, as in references [43] and [120], and the mission architecture study in reference [183]. Certain other uses of these devices have also been proposed, e.g. border patrol and the Army's Autonomous Rotorcraft Sniper System [12]. MAVs have become so important and popular recently that they have been the focus of a special section in the September 2008 AIAA Journal.

Considering the importance MAVs, an understanding of their aerodynamics is paramount for our nation's defense and space exploration agencies. This understanding begins by learning from nature. Nature has evolved many flyers, namely insects and birds, in the small size range occupied by MAVs and which possess many of the same highly desirable qualities. Vehicles designed to fly like insects are termed entomopters, and vehicles designed to fly like birds are ornithopters.

However, these creatures fly using intricate mechanisms, like flapping and plunging propulsion, many of which are not yet fully understood. Improving our understanding of such mechanisms will allow the design of better entomopters and ornithopters. Hence, the current research will investigate the flow features and forces generated by flapping and plunging wings using computational fluid dynamics (CFD)

and experimental techniques like particle image velocimetry (PIV.) These studies will be conducted over an appropriate range of low Reynolds numbers and reduced frequencies, and will quantify the effect of camber, if any. Also, the differences in forces and flow features generated by semi-elliptical and rectangular wings will be determined.

Previous work from our research group lab includes computations for two dimensional plunging airfoils [63], as well as force measurements ([60], [61]) and flow features ([61], [62]) have been investigated with flow visualization and particle image velocimetry. The present research consists of four phases. The first phase is three dimensional CFD of low Reynolds number (Re=500) wings in a constant freestream velocity at various angles of attack. The second phase consists of PIV experiments of flapping wings. The third phase is similar to the first phase, but with plunging instead of flapping wings, and will include higher reduced frequencies up to 0.45. The flapping experiment reduced frequencies were less than 0.14. Finally, two dimensional CFD of flapping wings will be performed. It is anticipated that this will expand the knowledge base of low Reynolds number wings and of flapping and plunging aerodynamics, which will in turn allow improved MAV designs.

2. REVIEW OF LITERATURE

Insects and birds have developed intriguing flight mechanisms that allow great maneuverability at their low Reynolds numbers. These are of interest to the micro aerial vehicles that also operate at low Reynolds numbers. Thus, this review of literature begins with a discussion of insect and bird flight. Insect flight is accomplished by either of two mechanisms, the Weis-Fogh mechanism or the delayed-stall-rotational-lift-wake-capture mechanism (henceforth to be referred to as the delayed-stall mechanism for brevity.) Table 2-1 lists some common insects and other animals and the mechanism they use. The first section in this chapter describes the Weis-Fogh mechanism and the second section describes the delayed-stall mechanism. Following the explanation of the two mechanisms is a section on birds, and then a section detailing the low Reynolds number aerodynamics of unmanned aerial vehicles. This penultimate section describes flapping and plunging airfoil aerodynamics from an engineering perspective, instead of the biological perspective on the first three sections. The chapter concludes with critical point theory, a technique employed in section 4.1.4.

Table 2-1: Insect flight mechanisms [96].

Weis-Fogh:	Delayed-Stall:
Hover flies, Syrphinae	Birds
Dragonflies, Odonta	Bats
Butterflies, Lepidoptera Rhopalocera	Most flying beetles
Wasp, Encarsia Formosa	Sphinx moths

2.1. THE WEIS-FOGH MECHANISM

Large flying animals, such as most birds, bats, larger insects, and migrating species like locusts, can fly forward rapidly and cannot hover. Their flight is attributable to normal steady flow aerodynamics. However, some smaller animals fly forward slowly and can hover. A biologist named Torkel Weis-Fogh conducted a landmark experimental

study [172] of insect flight published in 1973. In that paper, he identified a new mechanism for insect flight in addition to normal hovering, which has been termed the Weis-Fogh mechanism. This mechanism is commonly used in small insects at low Reynolds numbers; larger hovering animals usually use an essentially steady flow process that Weis-Fogh has termed normal hovering.

In normal hovering, the insect's body is inclined to the horizontal and can be almost vertical, while the wings move through a large stroke angle in the horizontal plane. Some such animals that use normal hovering are the hummingbird, many moths, flying beetles, most wasps, and the bumble-bee. This essentially steady process can produce a lift coefficient of one for Reynolds numbers less than 100. However, since drag is typically larger than lift at these low Reynolds numbers, the animals that use normal flight typically live in the Reynolds number region above 100.

The wing motion in normal hovering resembles a figure eight. Since the wings flip at the edges of the eight, they are at positive angle of attack at all times. Thus, they generate positive lift. This motion generates a substantial downwash, but it is canceled by the vertical component of the wing motion. As a result, the flow is essentially horizontal. Steady state aerodynamics applies. However, Maxworthy [99] points out that Weis-Fogh's steady state conclusion about normal hovering comes from the fortuitous cancellation of unsteady effects when averaged over a complete cycle.

One of Weis-Fogh's primary experiments was high-speed photography of a small wasp, Encarsia Formosa. This animal is used to control pest insects called aphids. It flies at a low Reynolds number of between ten and twenty, and requires a lift coefficient of between two and three. Such a large lift coefficient is impossible at that Reynolds number with steady flow, so the insect's ability to fly is attributed to unsteady flow phenomena. This situation is depicted in Figure 2-1 and described below.

When the insect undergoes rapid forward flight, its body is slightly inclined from the horizontal and its wings beat up and down at an angle. When the insect hovers, its body is steeply inclined and the wings beat horizontally. In part 1 of the figure, the insect's wings are together behind the insect. This is called the clap because the wings are clapped together. Then the wings fling apart with the rear (trailing) edges remaining together, as depicted in part two. Angular separation is then approximately 120^{o}. Part

three shows the first stage of the flip, where the wings rapidly move through approximately 130^{o}. They then flip so that the leading edge is facing up and begin moving back again in part four. Weis-Fogh uses the word flip for this as "it resembles the flipping of a pancake in the air" [172].

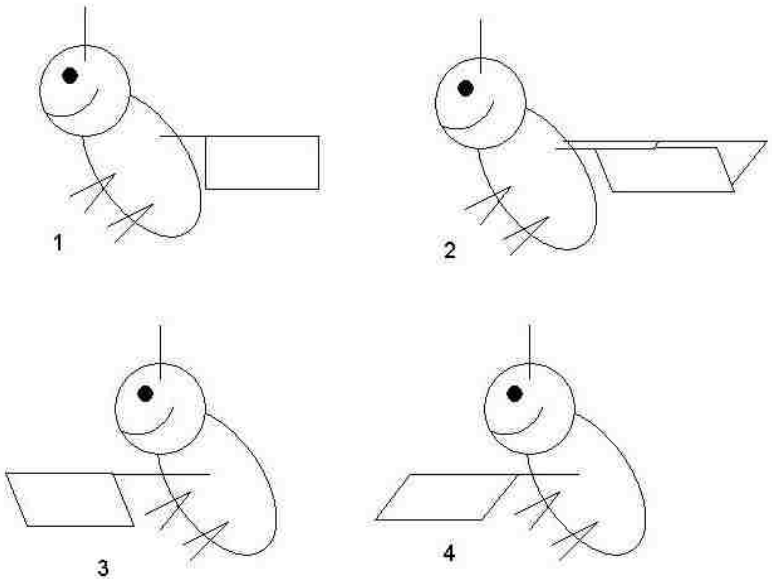

Figure 2-1: Weis-Fogh mechanism.

Since Weis-Fogh is a biologist, he consulted with the famous aerodynamicist Sir Lighthill, who wrote a paper later that year [89] on the aerodynamic problem. Lighthill's paper will be discussed in the next paragraph, and the consultations reported in Weis-Fogh [172] will be discussed in this paragraph. Suction is created when the wings fling open. Air enters the space created between the wings, thus causing vortices and circulation. Those vortices are shed at the end of the fling, and bound vortices around the wings follow the wings during the flip. The presence of this bound vortex allows the wing to move at a lower velocity than would be required to produce that amount of lift in steady flow. This fluid is impulsively started from an initial state without circulation. Since the circulation around the wings is equal in magnitude and opposite in sense, there

is no overall net circulation. At the end of the fling, the following equation gives the circulation, neglecting viscous effects:

$$\Gamma = 0.69\,\omega c^2 \tag{1}$$

where Γ is circulation, ω is angular velocity, and c is chord length. Weis-Fogh has experimentally confirmed this equation. Using this equation, and also frequency inversely proportional to body length (which is the most common relation,) it can be derived that lift by this fling mechanism is also inversely proportional to body length.

Since Lighthill's explanations utilize incompressible, inviscid flow theorems [70], those will be stated prior to discussing Lighthill's article.

Helmholtz's Theorems:

1. A vortex filament's strength does not vary along its length.
2. A vortex filament's starting point and endpoint cannot be in a fluid.
3. The fluid forming a vortex tube will always form a vortex tube of invariant strength as the tube moves.

Kelvin's Theorem: The circulation around a closed curve consisting of the same fluid elements is constant.

In normal flight, a delay between flapping and achieving full lift is caused by Wagner's effect: vorticity shed from the trailing edge requires time to establish circulation around a wing. This does not occur in the Weis-Fogh mechanism due to the clap and fling. Since the wings in this configuration are essentially one body that splits into two pieces, equal and opposite circulation can be generated around them without violating the incompressible, inviscid flow theories above. Here, the vortex around one wing serves as the starting vortex around the other wing.

During the fling, the flow is the irrotational flow caused by the wings angular rotation. Each wing has a circulation of

$$\Gamma = \omega c^2 g(\alpha) \tag{2}$$

where $g(\alpha)$ is a function of angular separation. Lighthill calculates this using a complex variable mapping and determined it to be 0.69, as stated in the above discussion of Weis-Fogh's article. Having established this circulation, the theories require that circulation to remain constant. This gives lift without vortex shedding.

However, Lighthill extends the analysis to include viscous effects, such as vortex shedding and reversed flow bubbles. With vortex shedding, the flow pattern behaves as that from irrotational flow caused by boundary motion plus the flow that the vorticity would generate if the boundary were at rest. A leading edge bubble of reversed flow is expected in the Weis-Fogh mechanism because the tangential velocity component reaches its maximum and then decelerates. However, this is counteracted by the strong inflow into the separation caused by the fling. Also, the reversed flow bubble may actually be beneficial: its thickness alters the apparent leading edge shape and enhances circulation.

Wing tip vortices are present in the Weis-Fogh mechanism. The inviscid flow theorems require that vortex lines must be closed, and this is accomplished by a tip vortex. This vortex is a circular arc as it follows the circular motion of the insect's wings.

Two important comments can now be made about the Weis-Fogh mechanism. Since the circulation around these wings does not violate the inviscid flow laws, this mechanism generates lift even when viscosity is not present. Also, the exact wing shape matters little. All that does matter is that there is an object around which circulation can form.

Maxworthy [99] conducted a flow visualization experimental investigation of the Weis-Fogh mechanism in two and three dimensions, focusing on understanding viscous effects. The use of two fluids, water and glycerin, allows tests to be conducted at either of two Reynolds numbers (32 and 13,000, respectively.) The leading edge separation vortex formed at the beginning of the fling contains almost all of the wing's circulation, and its magnitude is larger than predicted by assuming inviscid flow. Inviscid theory underpredicts this circulation later in the fling because a viscous fluid accumulates vorticity in the separation vortex. This circulation is greater at the lower of the two Reynolds numbers.

In three dimensions, the Weis-Fogh mechanism has several qualitative similarities to the two dimensional case. Flow separation occurs at every exposed edge during the fling. Also, a vortex appears on the bottom surface and reduces overall lift. This does not occur at the higher Reynolds number. Rather than concentrating into a vortex, the vorticity remains close to the bottom surface. Perhaps the most important of the three dimensional effects occurs at the beginning of the flip. The main leading edge vortex created during the fling from each wing joins, forming a tip vortex connecting the wings. This is ring shaped, and is fed by vorticity from the leading edge separation bubbles. Then, the wing flips, moves in the other direction, and circulation changes sign. Resulting from this motion, the vortex ring flips from the upper surface to the lower surface. It then moves downward, thus lifting the insect. However, a smaller vortex ring is created from the inner wing tip and moves upward, decreasing lift. Maxworthy concludes his article by presenting models of the fling mechanism, which match with experimental results. In a review article, Maxworthy [100] discusses all three topics of the present section and a bit more: normal hovering, the Weis-Fogh mechanism, and the viscous and three-dimensional effects.

Sun and Yu [139] conducted a CFD study of the Weis-Fogh mechanism at Re = 15. It was concluded that the clap and fling at the extreme of the motion does produce a vortex ring with downward momentum, and thus a lift peak. However, this vorticity dissipates rapidly and does not affect the remainder of the stroke. The mean lift during the main part is sufficient to support the body.

2.2. THE DELAYED-STALL MECHANISM

Only very small insects utilize the Weis-Fogh mechanism. Larger insects utilize the delayed stall mechanism. Here, a leading edge vortex on the wing's upper surface provides greater circulation, and therefore lift, than would be obtained without it. However, this effect only occurs over a limited distance, such as three or four chords [32]. After this distance, the vortex becomes unstable and detaches; this is called stall. However, this can be prevented by a stabilizing mechanism.

There are two such mechanisms, spanwise flow and downwash [38]. Outward spanwise flow combines with the vortex swirl creating a spiral leading edge vortex and also directs vorticity outward to the wing tip where it forms a tip vortex. Thus, the leading edge vortex does not grow too large and separate. With these stabilizing mechanisms, the leading edge vortex is able to provide enhanced lift over a great distance. A discussion of the role of PIV on model flapping wings and how this could be used to resolve the controversy of which mechanism stabilizes the LEV is given by Lauder [82].

Wang [168] provides a recent review article on insect flight that concentrates on the delayed stall mechanism. Not all insects utilize the Weis-Fogh mechanism to fly. However, all flying animals a crucial similarity: flying insects, birds, and bats, all produce very similar lift forces per muscle mass [96]. The quasi-steady mechanism of Weis-Fogh does not include unsteady effects that are necessary for lift generation. Additionally, the experimental methods in Weis-Fogh's work cannot reveal many of the effects that occur in realistic flight. As such, the delayed-stall mechanism has been proposed [32].

Dickinson and Götz [32] conducted an experimental study of a model wing in a sucrose solution. Time dependent lift and drag force measurements were recorded and flow visualization performed for a Reynolds number range of 79-236 and over a range of angle of attack from -9^o to 90^o. Increasing angle of attack increases lift, but it also increases lift to drag ratio. However, in this Reynolds number range, lift is a much more important parameter than the lift to drag ratio. Wagner's effect predicts that circulation, and thus lift, takes several chord lengths of travel to develop. However, insects develop their lift quickly, probably due to viscous effects. Specifically, this may be attributable to the delayed stall mechanism. Here, a leading edge vortex, which is larger than the stable separation bubble, remains attached to the upper surface at angles of attack greater than 13.5^o and low Reynolds number. This leading edge vortex is a low pressure region, and it also increases effective camber, so it can increase lift by either of those two mechanisms.

This study reveals several seemingly anomalous force peaks, especially at the ends of the motion where stroke reversal occurs. An explanation of this is given in a later

article by Dickinson, et al [34]. Rotational lift is generated by the Magnus effect: because of the rotating motion, velocity is higher on one side, enhancing circulation and thus creating a force in that direction. Emblemsvag and Candler [41] confirm the flow features reported by Dickinson et al, and report forces with the same trends, but two-thirds the magnitude. It was also found that thinner wings promote flow separation.

Three-dimensional effects, namely axial flow, may stabilize this vortex [34] [170]. This leading edge vortex will eventually be shed, but this takes a greater distance than is traveled by most insect wings. Thus, the short travel distance, around three chord lengths [31], allows insect wings to increase their coefficient of lift above the steady values.

At these high angles of attack, it is convenient to deal with a single circulatory force acting roughly perpendicular to the airfoil rather than lift and drag [31]. This single circulatory force creates these forces. A force peak occurs at angle of attack of 60^{o}, and acts perpendicular to the surface for angles of attack greater than 10^{o}.

Whereas the previous study focused on linear translation at various fixed angles of attack, M. Dickinson's next study [30] added wing rotation as occurs in the transition from downstroke to upstroke. This was an experimental investigation, as was the previous study. Three locations for the rotational axis were studied: near the trailing edge, centered, and near the leading edge. Of those, rotating about the trailing edge was found to be the most beneficial. Furthermore, the wing on the upstroke interacts with the wake left from the downstroke. This upstroke/downstroke interaction may be beneficial as the inter-vortex stream in the wake increases the wing's velocity relative velocity and angle of attack. This can be thought of as recovering energy lost during the previous stroke. Lift is further augmented during the flip by the generation of a vortex that is then captured by the wing's upper surface. Wang et al [170] proposes an additional rotational mechanism explanation, namely the Magnus effect, whereby rotation leads to different velocities and hence pressures on the two sides of the wing.

Sane and Dickinson provide an explanation for how the magnitude of these two mechanisms changes with angle of attack [130]. As angle of attack increases, the angular change from downstroke to upstroke decreases, and thus rotational lift decreases. However, wake capture is enhanced as angle of attack increases since more shed vorticity

from the previous stroke impacts the wing. Although rotating about an axis near the trailing edge increases total lift, it decreases the amount of rotational lift [129]. In this reference, a quasi-steady model that accurately predicts the time history of force generation, excluding wake capture, is presented. Ramamurti and Sandberg, in a finite element study [122], and also the CFD work of Sun and Tang [138], have confirmed the influence of rotational timing on force development, with advanced rotation generating the most force. Chasman and Chakravarthy [20], in an experimental and numerical study of pitching and plunging, revealed a complicated series of vortices consistent with this mechanism.

However, there is some dispute regarding these rotational mechanisms. In an experimental study on the hawkmoth, Ellington et al [40] determined that it is delayed stall, and not rotational effects, that accounts for the insect's lift. This conclusion was reached due to the flow visualization results showing the growth of circulation at the beginning of the downstroke. After rotation, the wing does not capture the vortex caused by rotation; but instead, another leading edge vortex develops due to translation.

More details regarding the influence of this wake is provided in reference [14]. When a wing initially intersects the wake from the previous stroke upon stroke reversal, lift is increased. The equation below provides a relationship between the vorticity change rate and force. The oncoming vorticity causes an increased vorticity growth rate, and thus lift. However, later in the motion, the downwash from the wake decreases the wing's circulation and reduces lift. Wake interaction consists of a complicated series of vortices, as follows. At the beginning of the downstroke, a leading edge vortex develops and a translational starting vortex appears. This vortex is initially attached to the wing, as is an under wing shear layer. Soon into the motion, the wing sheds the translational starting vortex. A rotational starting vortex develops at the trailing edge during the flip. Then, during the upstroke, the wing moves through both the leading edge vortex and the rotational starting vortex. This increase in vorticity accelerates the growth of a new leading edge vortex. A new under wing shear layer forms, and the process repeats with the next flip. Wang et al [170] confirms these results. They found that the unsteady effects of vorticity growth and wake interaction lead to changes in lift forces.

$$\vec{F} = -\rho \frac{d\vec{\gamma}}{dt} + m' \frac{d\vec{u}}{dt} \tag{3}$$

$$\vec{\gamma} = \int_{R\infty} \vec{r} \times \vec{\omega}\, dR \tag{4}$$

where m' is displaced fluid mass, $\vec{\omega}$ is vorticity, and $\vec{\gamma}$ is the first moment of vorticity.

The flow patterns around live hovering fruit flies were investigated by Dickinson and Götz [33] with flow visualization and laser interferometry. The major result of this study was the discovery of a vortex loop formed by the vorticity generated and shed during each downstroke and flip. This loop begins to form at the beginning of the downstroke behind the insect's body. When the wings flip, their bound vorticity is shed into the loop that then slides down the insect's body and away into the wake. This structure is roughly heart shaped. Circulation was not seen to develop during the upstroke. This may be attributable to an "additive Wagner effect" wherein the vortex shed during the flip prevents the buildup of circulation during the upstroke. Hence, there is one power stroke, the downstroke, and one recovery stroke, the upstroke. Using the relationship for momentum generated by a vortex ring, an equation relating ring circulation and the insect's force was derived. That equation produced realistic estimates.

That same year, 1996, Dickinson wrote a review article [31] on aquatic locomotion and the analogies with aerial locomotion. A major theme of that article was the link between forced produced by wings/fins and the wake structure. Any force that acts on the animal is balanced by an equal and opposite change in the wake's momentum, as per Newton's Laws. This is illustrated by the following figure, Figure 2-2, where it is clear that there is downward momentum in the wake. Figure 2-3 depicts the delayed stall mechanism.

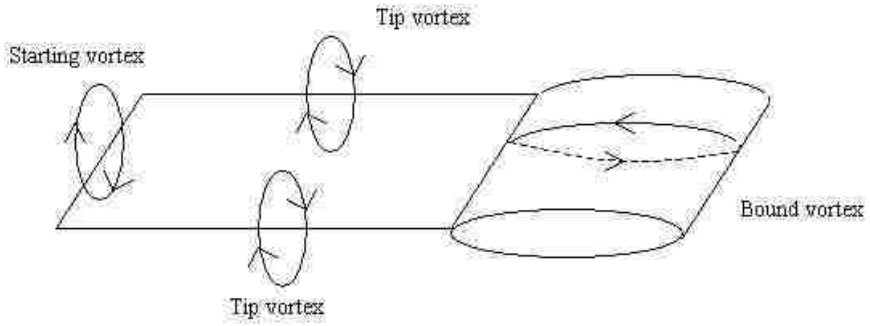

Figure 2-2: Vortices and wake on a wing.

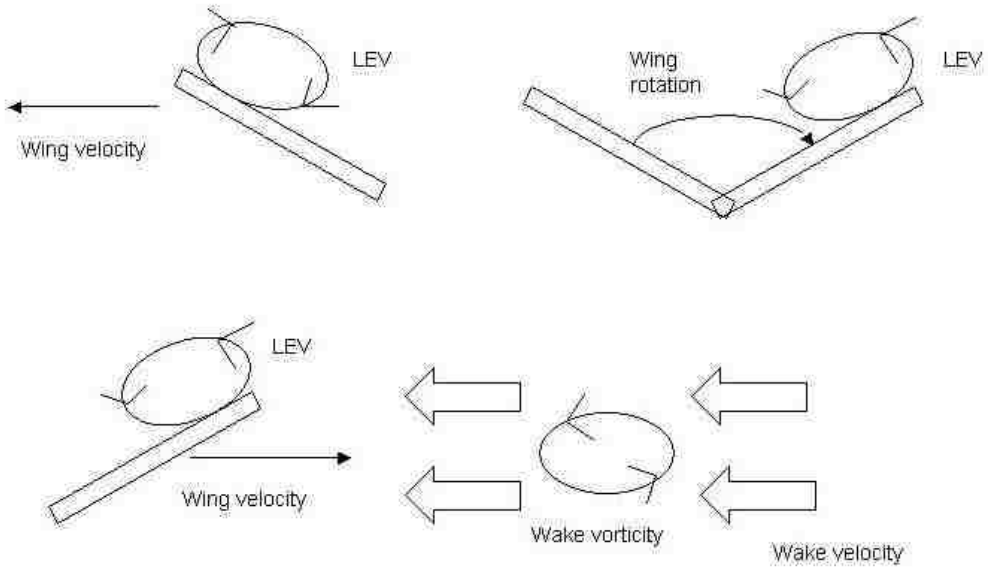

Figure 2-3: Delayed stall rotational wake capture mechanism.

Dickinson [31] identifies two parameters that determine if unsteady effects are important. They are the advance ratio and the reduced frequency. The advance ratio is the ratio of the body's velocity to the airfoil's velocity. The reduced frequency is the reciprocal of the advance ratio. These two parameters are defined as follows:

$$J = \frac{u}{2 A f R} \tag{5}$$

$$\sigma = \frac{2 A f R}{u} \tag{6}$$

where J is advance ratio, u is the body's velocity, A is the stroke amplitude, f is the flapping frequency, A is the flapping amplitude, R is the wing's length, and sigma is reduced frequency.

In contrast to the above discussion of reference [34], Birch and Dickinson [15] discovered that the vortex induced downward flow, and not the axial flow that stabilizes the vortex on a delta wing, stabilizes the spiral leading edge vortex on a fruit fly wing. This downwash, by reducing the effective angle of attack, prevents leading edge vortex growth to the point of detachment. This makes the leading edge vortex so stable that it is the vortex magnitude, and not the vortex stability, that limits the animal's flight performance. PIV measurements also indicated spanwise flow on their model wing caused by chordwise vorticity. This, in turn, forms a tip vortex and joins downstream with the shed leading edge vortex. However, the fruit fly operates at a low Reynolds number, much lower than, for example a hawkmoth, so different mechanisms may come into play for different animals due to Reynolds number effects. With a lower Reynolds number, there is less axial flow.

As alluded to at the end of reference [34], the next paper in the series [130] investigates the use of altering wing kinematics for maneuvering. Many wing trajectory parameters may be adjusted: stroke amplitude, angle of attack, flip timing and flip duration, and the shape and magnitude of stroke deviation. Optimum stroke amplitude, angle of attack, and wing tip trajectory were determined.

Sane and Dickinson [130] experimentally investigated those parameters with their dynamically scaled wing. The results will now be summarized. Increasing flip duration improves performance, and the flip should be symmetric of delayed. Stroke deviation degrades performance. Radial forces are produced, and the wing is traveling through the downwash of the previous stroke. Thus, when the wing deviates downward, it is affected more than then it deviates upward. Delayed stall becomes more important as stroke amplitude increases because the leading edge vortex provides lift over a greater distance. Rotational effects contribute more of the lift at lower stroke amplitude. Optimal lift

occurs at 45^{o} angle of attack, 180^{o} stroke amplitude, 10% flip duration, and flipping in advance of stroke reversal by 5%. Altering from this pattern causes less lift on one side than on another, thus allowing maneuvers.

Two other papers support the discussion in the previous paragraph. Further underscoring the sensitivity of insect flight dynamics, Fry et al. [48] found that the animal's lift is highly constrained by the need to balance forces and torques to keep the animal stable. He also found that fruit fly wings deviate in such a manner that they describe a U shaped trajectory. Also, Milano and Gharib [103] used a genetic algorithm to find the set of parameters yielding maximum lift. This is a more sophisticated optimization method than that applied in reference [130]. The results of this optimization reveal that the wing would travel the greatest distance that it can before shedding the leading edge vortex. Hence, the lift generated by this vortex acts on the wing for a longer distance.

Wang et al [170] confirms these results. In a study comparing two-dimensional CFD and three-dimensional experiments, forces were found to depend on the square of stroke amplitude. However, the forces depend more sensitively to the phase between stroke angle and angle of attack. This reference [170] also confirms one of the results of reference [31], in that periodic force generation is achieved after only two strokes.

Reynolds number effects are prominent, and flow features present in one insect at one Reynolds number may not be present in another insect at a different Reynolds number [16]. At Reynolds number of approximately 5,000, the leading edge vortex is stabilized by axial flow, which drains energy into a tip vortex. This is similar to the flow features over the leeward side of a delta wing. The resulting spiral vortex does not occur at lower Reynolds numbers. Birch et al [16] studied the leading edge vortex at Reynolds numbers of 120 and 1,400 and found a small region of fast spanwise flow in the leading edge vortex core at Re=1,400, but not at Re=120. This indicates the strong dependence of flow features on Reynolds number. Circulation increases from the root of the wing out to 60% of the wing's length. It then decreases because the leading edge vortex separates and forms a tip vortex. Thus, vorticity generated at the leading edge is transported into the wake. The wing generates less lift at the lower Reynolds number because viscous forces are more prominent than at the higher Reynolds number. These viscous forces

may be the reason that a spiral vortex does not occur at this Reynolds number. However, Ellington et al [40] has observed an axial flow stabilized spiral leading edge vortex on a hawkmoth, a relatively high Reynolds number insect.

Most of the previous discussion dealt with hovering flight. Dickson and Dickinson [29] investigated the behavior of lift and drag coefficients in forward flight. In their experiments, a wing simultaneously revolved at constant angular velocity and translated forward. Lift and drag coefficients are not constant throughout the stroke, as they are in hovering; thus, the quasi-steady model previously discussed requires modification. Dickson and Dickinson found that the tip velocity ratio, the ratio of the chordwise velocity component at the tip caused by translation and revolution, determines how lift and drag coefficients depend on advance ratio and stroke position. For angles of attack greater than 30^{o}, the coefficients of lift and drag both decrease as the tip velocity ratio increases. For lower angles of attack, coefficient of drag increases with tip velocity ratio. The authors indicate that the tip ratio is a more important parameter than the advance ratio, and that equal force coefficients result from equal tip ratios. Also, the tip velocity ratio is useful for comparing forces during forward flight to forces during hovering flight. When the tip velocity ratio is negative, coefficients of both lift and drag are greater than their hovering counterparts. The reverse is true for positive tip velocity ratios. Proportionalities for the lift and drag ratios are given in the two equations below.

$$C_L \propto \sin(\alpha)\cos(\alpha) \tag{7}$$

$$C_D \propto \sin^2(\alpha) \tag{8}$$

It has been suggested [7] that honeybees do not utilize the above mechanisms, with their long strokes and attached leading edge vortices. Instead, honeybee's stroke lengths are shorter and their flapping frequency is higher. With shorter stokes, unsteady forces generated during stroke reversal dominate over the translational forces. However, these short strokes are less efficient than longer strokes, and it is speculated that the insect chooses this inefficient mode of flight for other considerations, like maneuverability, foraging, etc.

Wang [169] investigated two time parameters and how they relate to vortex formation, vortex shedding, and force development. Three regions on a graph of force versus distance were attributed to: the diffusion of vorticity in the boundary layer immediately upon starting the motion, formation of an attached leading edge vortex, and a quasi steady region of vortex shedding. This wing generated thrust, since its lift force was tilted in the forward direction. Also, a vortex wake developed with vortices rotating in the opposite directions to a von Karman wake. There was a velocity component in the direction opposite the wing's motion, thus generating thrust. Thrust only occurs in a time window confined by an upper and lower bound attributed to the shedding of the leading edge vortex and the growth of the trailing edge vortex, respectively. A wing should flap at such a frequency that the leading edge vortex has time to form, but not so long that the vortex has been shed. Two major conclusions were reached in this article. First, the optimal advance ratio is dictated by maximizing the angle of attack without stalling. This corresponded to angle of attack between 45^{o} and 60^{o}, with an advance ratio between 0.16 and 0.27. Second, the optimal reduced frequency is between the two time scales mentioned above, and is inversely proportional to wing length.

Usherwood and Ellington conducted a two-part study ([159] and [160]) of revolving wings. The former study dealt with hawkmoth wings, while the latter study employed four wings, including both insect and bird. This allows the wing to experience higher flow velocity at the tip than at the root, and allows the experimenter to investigate the downstroke and upstroke without the flip between the two. This study confirms many aspects of the delayed stall mechanism described above. Spiral leading and trailing edge vortices, stabilized by spanwise flow, are present on these steadily revolving wings. Thus, they are steady flow phenomena. This leading edge vortex is the force generating mechanism, and forces are essentially unaffected by leading edge shape, twist, and camber. Van Den Berg and Ellington [161] provide flow visualizations of the leading edge vortex separating at 75% span, joining the tip vortex, and then forming a wake.

Dragonflies are one of the few gliding insects. Wakeling and Ellington [167] have documented the exceptionally high performance of dragonfly wings. As indicated from their ability to glide, dragonfly wings generate substantial lift in a steady flow process, much more so than any other insect wing can. This performance is attributable

to many morphological considerations. Dragonfly wing leading edges are sharp, which promotes separation. Also, dragonfly wings have corrugations that trap vortices and alter the wing's effective shape. Finally, hairs extend outside the boundary layer and act as turbulators.

Tamai et al [148] studied three dragonfly-like airfoils at the micro aerial vehicle appropriate Reynolds number of 34,000. These airfoils were streamlined, corrugated, as in a dragonfly, and a flat plate. The corrugated airfoil performed well and resisted stall since its corrugations created unsteady vortices and tripped the boundary layer. Thus, higher velocity air farther from the surface was brought closer to the surface, and flow separation is delayed.

Taylor et al [151] also studied the flapping frequency in both aquatic and aerial locomotion. His work largely supports the work of Wang [169]. Taylor et al speculate that evolution has driven both swimming and flying animals to cruise at a Strouhal number, from 0.2 to 0.4, that maximizes efficiency. Strouhal number is defined in equation 9, where f is flapping frequency, A is wake amplitude, and U is freestream velocity. This corresponds to maximizing the amplitude of shed vortices. It has also been postulated, by Lentink and Gerritsma [85], that insects fly at a Strouhal number close to the Strouhal number of natural vortex shedding. This is termed frequency locking. This same study also underscored the importance of wing shape, with aft camber being important for flapping flight.

$$St=fA/U \tag{9}$$

2.3. BIRD AERODYNAMICS

The major fluid mechanical difference between insects and birds is the Reynolds number at which they fly [38]. Birds, being larger than insects, operate at a larger Reynolds number, such as 20,000-100,000, compared to 10,000 for the largest insets. These higher Reynolds numbers allow transition to turbulence. A Reynolds number of 10,000 is sufficient to promote transition at the sharp leading edge of an insect wing. The leading edge vortex looses cohesion at Re=10,000, and becomes less well organized

above that number. Increased mixing due to turbulence disrupts the intense velocity gradients present in the leading edge vortex, and the two-dimensional form results. Periodic vortex shedding, with a concomitant lift reduction, begins to occur at a Reynolds number of 20,000. From Re=10,000 to 100,000, which is birds, axial flow stabilizes the leading edge vortex, but for Reynolds numbers less than 1,000, which is insects, the vortex is stabilized by downwash.

Templin [152] investigated the flight characteristics of all known types of flying animals, including pterosaurs. Rayner [127] has also investigated flight charactersistics and wing beat kinematics and how they impact performance. Momentum stream tube theory was applied and used to determine such things as range, maximum weight, and cruising speeds. This approach was validated in the article. It was further determined that most flight characteristics depend on two parameters, mass and wing span. Liu et al [93] mathematically modeled bird wing kinematics as Fourier series for three characteristic angles as functions of time.

Liu [92], in an article describing how CFD can be used in biology, studied the leading edge vortex as an example problem. Liu confirms the stabilizing roll of axial flow in the leading edge vortex at these Reynolds numbers and concludes that the axial flow is generated by a spanwise pressure gradient generated by the leading edge vortex.

Flying animals leave vortices in their wakes. Spedding et al [136] and Hedenström et al [54] conducted PIV experiments on bird wakes. The former study determined that closed vortex loops shed during the downstroke produce vortex rings in the wake. A downwash of fluid exists between these vortex rings and is of sufficient momentum to keep the bird aloft. The upstroke is mostly inactive regarding the production of force and vortices. This study also gives some typical numbers for bird flight, namely reduced frequency of k=0.6, forward velocity of u=10 m/s, flapping frequency of f=10 Hz, and chord length of c=0.10 m. The unsteady vortex wake was also investigated by Philips, et al [117], who used it to determine flapping power requirements.

Hedenström et al [54] experimented on four bird species in a wind tunnel and determined vorticity and circulation both decrease with increasing flight speed. Further,

they define a normalized circulation, $\frac{\Gamma}{u\,c}$, which equals half of the time-averaged lift coefficient. Tobalske et al [154] also studied bird flight at various speeds, but whereas Hedenström et al [54] concentrated on fluid mechanics, Tobalske et al [154] concentrated on kinematics. Low aspect ratio wings have the same kinematics at high (>9 m/s) and low (<9 m/s) speeds. High aspect ratio wings have a wing tip reversal on the upstroke for low speeds, but no wing tip reversal for high speeds.

The second part of the two-part Usherwood and Ellington study ([159] and [160]) mentioned in the insect section dealt with revolving insect and bird wings. This study points out the similarity between bird and insect wing aerodynamics. They are both insensitive to changes in camber, roughness, and aspect ratio. Furthermore, force coefficients for the insects and birds in this study were quite similar.

Hummingbirds, which hover at a Reynolds number of 3,000, are not like regular birds in two major respects [171]. First, they are the only bird that can hover for prolonged periods. Second, both their downstroke and upstroke produce lift. The downstroke produces 75% of the lift and the upstroke produces 25%. This asymmetry is attributed to a difference between birds and insects. Unlike thin and flexible insect wings whose camber can reverse, bird wings are rigid. Thus, their camber on the upstroke is essentially negative, accounting for the reduced effectiveness of the upstroke.

Hummingbirds have an important similarity with insects, namely they both have a large leading edge vortex, and therefore delayed stall. In hummingbirds, this vortex only occurs during the downstroke and is shed at the transition to upstroke. However, Ellington [38] and Altshuler et al [8] investigated hummingbird wings at Re=5,000 in a revolving wing experiment and found flow over a hummingbird's wing remains attached. Revolving wings mimics the flapping motion with larger velocity at the tip than at the root. Thus the hummingbird generates more lift and less drag than the insect leading edge vortex mechanism. The likely cause for this is feathers acting as turbulators, which destroy the leading edge vortex. Performance is so good that lift to drag ratios of 8 to 16 can be generated.

2.4. SMALL AIRCRAFT AERODYNAMICS

Table 2-2 lists the Reynolds numbers for several common flying objects. Ellington [39] presents an in-depth analysis of insect based micro-air vehicles (MAVs) incluidng mass supported, power requirements, maximum flight speed, and other performance parameters. This paper bridges the gap between biology and aerospace engineering. Two other such papers are Spedding and Lissaman [137] and Freymuth [47]. The former concentrates on design problems, like low Reynolds number performance degradation and increased susceptibility to turbulence, while the latter explains how dynamic stall can be advantageous to highly maneuverable aircraft.

Table 2-2: Reynolds numbers for various flying objects.

Object	**Reynolds Number**
Insects	10^2 - 10^4
RC Airplanes	10^3 – 10^6
Birds	10^4 – 10^6
General Aviation	10^6 – 10^7
Large Airplanes	10^7 – 10^8

A recent review of small vehicle aerodynamics is given by Mueller and DeLaurier [104]. This article focuses on the aerodynamics of wings at Reynolds numbers less than $2x10^5$ and oscillating wing propulsion. The article also provides a justification for flapping wing propulsion, since it generates lift and thrust without substantial weight. Most micro aerial vehicles are around 10cm long and fly at speeds around 10 meters per second [148]. Mueller and DeLaurier [105] identified several important issues for the design of MAVs. They are: the effect of camber and planform shape, how motion and pitch affect thrust and lift, and how planform shape and flexibility affect dynamic stall, separation, and attached flow. Many of these issues will be addressed here, but others, like flexibility and aeroelasticity, are beyond the scope of this work. For an example of aeroelasticity and a closed loop control system designed for a flexible wing, see Ho et al .

Mueller's and DeLaurier's review article [104] also details some flow features at low and intermediate Reynolds numbers. Standard, classical theories work well in the passenger rated aircraft whose Reynolds numbers are greater than 500,000. Below this Reynolds number, performance deteriorates due to laminar boundary layer separation. Most Micro Aerial Vehicles, or MAVs, operate in the Reynolds number range from 30,000 to 200,000, where an airfoil's thickness is important and affects separation. After separation, this shear layer usually does not transition before reattachment. For Reynolds numbers from 70,000 to 200,000, the flow is laminar and has a large separation bubble. This bubble shortens at higher Reynolds numbers, thus improving performance.

In the aerospace literature, "low Reynolds number (Re_c)" means a Reynolds number less than 4,000,000. This is substantially higher than the $Re_c = 500$ in Section 4.1. Re_c is Reynolds number based on chord length. Three Reynolds number ranges are described in McMasters and Henderson [102]: subcritical, where $Re < 400{,}000$, critical, where $400{,}000 < Re < 500{,}000$, and supercritical, where $Re > 500{,}000$. The flow over a low Reynolds number wing is dominated by the laminar separation bubble, and is discussed in two review articles, Lissaman [90] and Carmichael [18]. A laminar boundary layer is not able to overcome an adverse pressure gradient, so it separates. This separated boundary layer forms a free shear layer and is more susceptible to transition. Free shear layers are unstable and transition more easily than boundary layers. After transitioning to turbulent flow, increased entrainment causes reattachment. The shear layer is able to overcome the adverse pressure gradient and then reattaches to the wing's surface as a turbulent boundary layer. However, for Reynolds number less than 50,000, there is insufficient distance for this reattachment to occur. In the subcritical regime, open separation without reattachment can occur at high angles of attack [102]. Since pressure is low in laminar separation bubbles, they increase the airfoil's drag and reduce its performance. Higher Reynolds number wings will have smaller bubbles and better lift to drag ratios [132].

Jian and Ke-Qin [66] used CFD and flow visualization to investigate the flow field over low aspect ratio elliptical planform wings. They found three vortices in the separated region: primary and secondary separated vortices, and tail vortex. The primary separated vortex constantly sheds from $\alpha = 0^o$ to 30^o, but the secondary separated vortex

only sheds at 5^o. It moves upstream as angle of attack increases. For angles of attack greater than 30^o, the primary separated vortex becomes stationary above the wing. While the primary and secondary separated vortices are fixed, the tail vortex continuously grows and sheds. The stationary vortex consists of counter rotating vortices, and only on low aspect ratio wings; they are shed on high aspect ratio wings. The tip vortex is responsible for the stationary vortex behavior. Its vertical component causes separated vortices to move with the wing, this causing the separated vortex to be stationary for angles of attack of 33^o and higher.

The laminar boundary layer's post separation behavior dictates the increased drag and decreased lift at low Reynolds number [104]. For these Reynolds numbers, the boundary layer remains laminar and separates into a shear layer. This layer does not reattach for Reynolds number less than 50,000, but does for higher Reynolds numbers, thus forming a transitional separation bubble. Called a long bubble, stall occurs when this bubble reaches the trailing edge. Since the flow is unsteady downstream of this bubble, hysteresis can occur. The CFD simulations of Davis and Carter [25] revealed some cases with one primary bubble and some cases with a secondary counterrotating bubble inside the primary. More details on transitional separation bubbles appear in reference [58].

Fitzgerald and Mueller [42] conducted a laser velocimetry and hot wire experiment on the transitional separation bubble on a low Reynolds number wing. Reverse flow occurs in this bubble, but has no effect on the growth of boundary layer parameters of displacement, momentum, and energy thickness. Reversed flow does affect the magnitude of these thicknesses and shape factor.

Choi and Lee [20] provide a model for transitional separation bubble transition in which the Reynolds number at transition was found to depend on the Reynolds number at separation and the Thwaites parameter. This separation bubble can burst in either of two ways [98]. The first occurs when the long bubble cannot remain attached against an adverse pressure gradient, so it separates. The separated bubble then transitions, where the increased mixing allows the much shorter bubble to reattach. The second form of bursting is when this short bubble cannot be maintained and grows continuously.

Elimelech et al [37] propose a three phase transition to turbulence process for airfoils at Reynolds numbers from 5,000 to 60,000. The first phase has a laminar wake that is stable for a few chord lengths; the second phase has a well ordered vortex street wake, and in the third phase, the vortex street becomes unstable and a bubble occurs on the suction surface. As the magnitude of reversed flow reaches a certain value, a global instability occurs. Thus, the shear layer transitions and reattaches, and stationary vortices are shed.

Lian and Shyy [87] also investigated transition at Reynolds numbers from 10^4 to 10^5. As angle of attack increase, separation and transition positions move upstream. The strong adverse pressure gradient causes transition. At angles of attack just prior to stall, the laminar separation bubble becomes shorter and thinner. Reynolds number was found to affect this process. Increasing Reynolds number increases turbulence intensity and shortens the separation bubble.

The literature in the Reynolds number range from 0-1,000 is scarce, but is much more plentiful for airfoils in the range from 10,000 to 1,000,000. The lowest Reynolds number study found in the literature was Kunz and Kroo [75], at a Reynolds number of 1,000. Laitone [79], [80], and [81], has experimentally investigated cambered rectangular plate wings at Reynolds numbers as low as 20,000. Cambered plate wings bent to 5% camber with sharp leading edges were found to give higher lift/drag ratios compared to a NACA 0012 section wing. Slightly cambered and flat plate wings are less sensitive to Reynolds number variations than the NACA 0012. The sharp leading edge is beneficial as it continuously sheds vortices which reduce the size of the separated region. Momentum lift, lift generated by the wing redirecting the flow, was observed for the bent plate, and it allowed $C_L>1$ after stall. Null and Shkarayev [108] also investigated the effect of camber on circular planform airfoils at Reynolds numbers ranging from 50,000 to 100,000. 3-9% camber was found to be optimal, with the optimal amount of camber increasing as speed decreases. Slower speeds necessitate higher angles of attack, and more camber promotes attachment at these higher angles.

Kunz and Kroo [75] conducted numerical simulations of the two-dimensional Navier-Stokes equations at Re_c ranging from 1,000 to 10,000 to study the effects of camber, thickness, and leading edge and trailing edge shapes. Lift coefficient was found

to increase with decreasing Re_c, but lift to drag ratios decrease with decreasing Re_c since drag increases. Section geometric parameters also affect performance. Drag increases and lift coefficient decreases as thickness increases. Thus, thickness should be small. Camber distribution is also important, with 2% camber found to be optimal. Since the boundary layer thickness increases as Reynolds number decreases, the effective wing shape is altered. Effective camber is reduced as angle of attack increases. The thick boundary layer is responsible for large regions with little pressure change, and also a displacement effect that delays separation.

Sunada et al [141] in an airfoil study confirm the results of Tamai et al [148], who investigated dragonfly-derived wings. Their experimental investigation of airfoils at a Reynolds number of 4,000 show that sharp trailing edges and corrugations increase the lift to drag ratio by reducing drag. This is related to the transitional separation bubble's thickness. In a later study, Sunada [142] systematically examined twenty airfoils with an aspect ratio of 7.25 and at the same Reynolds number as the previous study. Here, the influence of sharp leading edges and corrugations was confirmed, and the effect of slight (5%) camber was also determined to be beneficial.

An overview of the aerodynamics and design considerations appropriate for the low Reynolds number regime is provided by Selig [132]. There are three considerations: a convex pressure recovery, lack of large adverse pressure gradients near the trailing edge, and a transition point that moves forward as angle of attack increases. Selig et al. [131] discussed the laminar separation bubble and its effects on lift forces in wings at Reynolds numbers from 40,000 to 150,000: nonlinear lift and lift hysteresis. The movement and growth of the laminar separation bubble causes both of these effects. As angle of attack increases, the laminar separation bubble on the upper surface grows, thereby increasing displacement thickness and introducing negative camber. The separation point also moves toward the leading edge. When the angle of attack is too high, reattachment becomes impossible and the bubble bursts, causing stall. The growth and movement of the bubble when angle of attack decreases is not symmetric with the increasing angle of attack behavior, resulting in hysteresis. Tripping the boundary layer would mitigate some of these effects and would result in a bubble that shrinks and moves

upstream as α increases. Biber et al. [13] have designed an airfoil successfully meeting the design considerations mentioned above at $Re_c = 50{,}000$.

Hsiao et al. [59] have conducted flow visualization of tip vortices on wings at $Re_c = 100{,}000$. These vortices create a suction region over the wing which dominates lift production at high angles of attack, greater than 10^o. Tip vortices are also beneficial because they promote flow attachment along the upper surface, thereby delaying stall. However, this effect is only present in low aspect ratio wings, as they are too far removed at higher aspect ratios. The effect of a tip vortex is only felt in the immediate vicinity for aspect ratios of eight and larger, according to experiments at Reynolds numbers from 70,000 to 300,000 [1]. Not all effects of the tip vortex are beneficial; its downwash reduces the effective angle of attack and causes induced drag [163].

Flow features behind the airfoil also affect forces. As α increases, the separation point on the suction surface remains stationary, whereas that on the pressure surface moves aft [76]. This asymmetric flow separation at the trailing edge alters pressure distribution causing a high lift curve slope at low angle of attack at $Re_c = 300{,}000$ [76]. In a study [128] performed at $Re_c = 200{,}000$, the separation point was found to be stationary only in a range of α around 2^o. Generally, as angle of attack increases, the separation point, transition point, and turbulent reattachment point all move towards the leading edge. Since the reattachment point moves forward faster than the reattachment point, the bubble shrinks. An airfoil with a bubble that shrinks and moves forward as angle of attack increases will exhibit a gentle stall. An airfoil at $Re_c = 50{,}000$ was successfully designed with this gentle stall [13].

A wing's drag is given by the below equation consisting of two terms [104]. The first is the parasite drag coefficient at zero lift and the second is the induced drag due to lift. AR is aspect ratio, the wingspan squared divided by planform area, and e is Oswald efficiency. This equation indicates that a large aspect ratio, such as three or more, is preferable as it will reduce drag and increase range. However, lower aspect ratio wings have their advantages, including at low Reynolds numbers. Tip vortices influence the flow over the entire span, thus contributing to lift and a high angle of attack before stall. Additionally, Viieru et al [163] found that induced drag from the tip vortex increases total drag, but that the effect, at moderate angles of attack, can be alleviated with endplates.

$$C_D = C_{D0} + \frac{C_L^2}{\pi AR e} \tag{10}$$

The effects of camber and planform on flow features and force generation in a low Reynolds number flow have been studied [114], [68]. For thin wings, camber was found to be beneficial in the range of Reynolds number from 60,000 to 200,000, as it promotes flow attachment [114]. The lift curve slope was not affected by planform shape and Reynolds number, despite differing wake structures, at Reynolds numbers of 8,000 and 24,000 [68]. A semi-ellipse wing produces a less coherent trailing vortex structure than a rectangular wing [68]. However, at a similar Reynolds number (200,000) and aspect ratio (0.5 to 2), Cosyn and Vierendeels [24] found lift characteristics are similar for cambered plates and flat plates. Drag was also similar until flow over the flat plate separates, again showing that camber promotes flow attachment.

2.5. FLAPPING AND PLUNGING WING AERODYNAMICS

Micro air vehicles (MAVs) have recently received great attention due to their unique capabilities, including hovering, indoor flight, and maneuverability. Their maximum dimension is less than 15cm, and weigh less than 100g. Many MAVs, micro air vehicles, use flapping wing propulsion, as this form of propulsion is advantageous over traditional forms at low Reynolds numbers [104]. Pines and Bohorquez [118] discuss the need for MAVs and the flow physics that limits their performance. The ornithopter, which flies like a bird, was identified as showing the greatest promise. Types of small scale propulsion and power are also discussed. Insect-like MAVs, or entomopters, are analyzed by Ellington [39]. Ramamurti and Sandberg [124] propose vehicle designs inspired by insect flight and fish swimming mechanisms.

Flapping wing aerodynamics is usually studied with experimental or numerical methods; analytical methods are only rarely applied to this problem. Vest and Katz [162] developed a potential flow model capable of analyzing unsteady, three-dimensional flows. A time area averaged momentum stream tube model capable of predicting cruise

velocity, power, and efficiency for flapping flight is provided by Liu [95]. The same author, in a different work [94], proposes various scaling laws for fixed and flapping wing aircraft and biological flyers. DeLaurier [27] developed a strip theory in which the wing is divided into strips, each of which produces forces and moments in response to plunging and pitching. The effect of stalled strips is incorporated. Among the few analytical solutions available in the literature are integral equation solutions ([73], [174], and [135],) a conformal mapping procedure [21], and a singular perturbation method [65].

A mechanism by which plunging wings produces thrust is the Knoller-Betz effect [67]. The plunging motion of an airfoil creates an effective velocity at an angle to the freestream. Since the force is predominately perpendicular to the freestream, both a lift and a thrust component exist. This is illustrated in Figure 2-4.

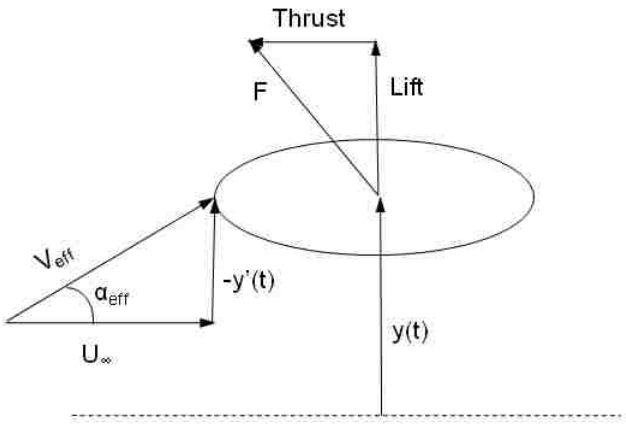

Figure 2-4: Knoller-Betz effect.

Freymuth [46] identifies three hovering modes: mode 1, also called water treading mode, which is leading edge trailing edge switching, and mode 2, also called normal hovering or figure eight mode, in which the leading edge is not switched. Mode 3 is an oblique version of mode 2 with a deflected wake. Thrust generation from a reverse von Karman vortex street was observed for all modes. A reverse von Karman wake is where vortices are of the opposite sense of a normal wake, produces a jet like velocity profile.

The wake behind flapping airfoils can be quite complex. Von Ellenrieder et al [164] noted a complicated wake structure as vortices shed, stretch, and combine. The LEV and TEV, trailing edge vortex, shed near the mean point and extreme points of the heaving motion, respectively, and form a series of interconnected loops. When the Strouhal number exceeds 0.3, an additional TEV is shed. Strouhal number has been found to affect thrust production, with thrust only occurring in certain ranges. For example, Triantafyllou et al [158] found a preferred range of $0.25 \leq St \leq 0.35$. Efficiency, defined as $\eta=TV/E$, where T is thrust, V is velocity, and E is input power, achieves its optimum at a Strouhal number in the above range which maximizes wake spatial amplification. A later study [9] gave a slightly different Strouhal number range, and also determined how the reverse von Karmam vortex street is formed. The LEV sheds on alternating sides of the airfoil, convects downstream, and interacts with the TEV; this happens twice per cycle. Wang [169] also discusses frequency selection and the time scales for vortex formation, and in particular, how the ideal frequency should be between the time scales defined by shedding of the leading edge vortex and growth of the trailing edge vortex.

Platzer et al [121] provide a review paper on the physics of thrust and lift generation for flapping wings. For pure plunging at high Reynolds numbers, thrust is developed from the shedding of trailing edge vortices, but at low Reynolds numbers, thrust generation comes from the shedding of both leading and trailing edge vortices. These form a reverse von Karman street with a jet profile [166]. Lee et al [84] propose a type of thrust generation distinct from the reverse von Karman vortex street. Thrust is generated at the end of the upstroke, where vortex pairing and vortex staying occur. A jet is created between these paired vortices, thus creating thrust. DeLaurier and Harris [28] identified two mechanisms for thrust production: leading edge suction, which works even at $\alpha = 0^o$, and the streamwise component of the wing's normal force. For the three dimensional case, a series of alternating vortex rings, which form a reverse von Karman wake in cross section, is formed, and the dynamic stall vortex interacts with the tip vortex [121]. Two oblique jets caused by vortex structures form downstream of flapping wings [35]. Another three dimensional effect is spanwise flow, which increases velocity

differences between the upper and lower surface of a flapping wing, thereby increasing lift [56].

Additional visualizations of the complicated three dimensional wake consisting of intertwined vortex rings are provided by Parker et al [112]. Both the leading and trailing edge vortices formed from a pair of co-rotating vortices. Lai and Platzer [77] performed flow visualization of the vortex street and found that the non-dimensional plunge velocity, which is the reduced frequency multiplied by non-dimensionalized plunge amplitude, is the governing parameter. Thrust was generated when this parameter exceeds 0.4. Two vortices of the same sense are shed per half stroke for a non-dimensional plunge velocity around 0.2, while only one vortex is shed per half stroke for non-dimensional plunge velocity around 0.6. Their visualizations show trailing edge vortices forming the wake, and Young and Lai [180] also indicate wake structures depend on trailing edge effects. However, they also note that leading edge effects control forces for reduced frequencies less than four. In particular, vortices shed into the wake look like mushrooms; when pointed upstream, drag is produced, and when pointed downstream, thrust is produced. Chandar and Damodaran [19] show thrust production benefits of a sharp trailing edge. A large radius leading edge prevents the LEV from growing too large and shedding prematurely, and a sharp trailing edge promotes jet formation [83]. Young and Lai [180] also note multiple vortices shed per half stroke, and explain it as resulting from the interaction between the natural bluff body shedding frequency and the shedding imposed by plunging. This is termed vortex lock-in [181]. However, Lewin and Haj-Hariri [86] and Lua et al [96] determined that both leading and trailing edge vortices interact and form the wake. At high frequencies, the wake transitions to a chaotic flow through the quasi-periodicity and phase locking scenarios, as described in Blondeaux et al [17]. Five wake types were reported by Lua et al [96]. When vortices from the leading edge merge with vortices from the trailing edge, three types of wake are possible: deflected, von Karman, and reverse von Karman. When vortices do not merge, the wake is either dissipated or neutral. The deflected wake is caused when, at high reduced frequencies, vortices shed from the trailing edge interact nonlinearly [78]. Anderson et al [9] also propose the equivalent importance of both edges. When this leading edge vortex is attached to the upper surface of a pitching and plunging airfoil, lift

force is reduced, but lift increases when it sheds [125]. However, Tuncer and Platzer [156] reveal the thrust generating benefits of a large leading edge vortex, even though it reduces efficiency.

In addition to the controversy over the dominance of leading edge or trailing edge effects is the controversy over the governing parameter for plunging wings. Some researchers, like Lai and Platzer [77], indicate that the governing parameter is the non-dimensional plunge velocity. Others, such as Young and Lai [180] and Lewin and Haj-Hariri [86], indicate that both reduced frequency and non-dimensional plunge velocity are important. Strouhal number is directly proportional to the non-dimensional plunge velocity. The angle of attack also plays a role in a combined parameter, with Ramamurti and Sandberg [125] showing a dependence of thrust on the product of reduced frequency and angle of attack, rather than both individually.

Von Ellenrieder et al [165] discuss frequency selection and three dimensional flow features for flapping wings. Flow visualizations for purely plunging and purely pitching airfoils are provided by Freymuth [45]. Parameter selection for optimal thrust generation has received extensive attention, including the work of Anderson et al [9] and Young and Lai [179], among others. Anderson et al [9] provide a list of parameters for optimal thrust generation, including Strouhal number from 0.25 – 0.40, heave amplitude close to chord length, angle of attack from 12^o – 25^o, and pitch leading heave by a phase angle of 75^o. Young and Lai [179] found a decrease in efficiency at high reduced frequencies because of vortex shedding away from the centerline at the trailing edge and lack of time for the leading edge vortex to form. Isogai et al [64] associate low efficiency with substantial flow separation, as additional work is performed against the suction region [156]. A variational method for minimizing power in flapping flight has been developed and used to derive optimal conditions [53]. Nagai et al [107] discuss the three aerodynamic force mechanisms at work in flapping flight: delayed stall, rotational lift, and wake capture and how they vary as functions of stroke plane angle and advance ratio.

The effects of kinematics and geometry have also received extensive attention. Some examples are the work of Ansari et al ([10] and [11],) and Okamoto and Azuma [109]. Young et al [182] investigated a dragonfly wing over a wide range of kinematic parameters, including flapping frequency, flapping amplitude, and Reynolds number. In

particular, the timing of pitch relative to stroke reversal is governed by a trade off. Advanced rotation allows for increased lift, but drag also increases, and the shedding of a strong starting vortex reduces lift. Thus, it is preferable to advance pitch by a small amount, around 5%. Pitching about the mid-chord provides the best compromise between ejecting vortices shed from the leading and trailing edges during stroke reversal. The starting vortex shed from the leading edge after stroke reversal inhibits the development of the new leading edge vortex, and should thus be ejected at high speed. Similarly, startup and stopping vortices shed from the trailing edge reduce lift and should be ejected. The best compromise is to flip at mid-chord. Regarding wing geometry, a large aspect ratio increases both thrust coefficient and efficiency, and a straight leading edge is preferred [35]. An airfoil has been optimized for efficient thrust generation [83]. It looks like a tadpole, with a thick leading edge to prevent the formation of a large leading edge vortex, and a thin trailing edge to create a large pressure difference and thus thrust.

High thrust and high efficiency frequently occur at different and conflicting kinematics, e.g. Tuncer and Platzer [157]. High thrust occurred at high reduced frequency and high amplitude, while high efficiency occurred at low reduced frequency and high amplitude.

One of the primary outstanding issues is the stabilizing mechanism for the leading edge vortex, LEV, a low pressure region which has been identified as the cause for sustained lift generation in flapping wings. Lauder [82] provides a discussion of the two contending ideas. Ellington et al [40] proposes spanwise flow convects vorticity away from the LEV towards the tip, where it joins the tip vortex and forms a vortex ring. This prevents the LEV from growing too big and shedding. The tip vortex, in addition to delaying separation, also increases lift ([134] and [57].) Maxworthy [101] derives pressure and velocity distributions in a leading edge vortex. The pressure distribution, caused by balancing the centrifugal force and the vorticity distribution, causes axial flow. Consider a rotating wing whose tip experiences greater velocity than its root. A velocity distribution thus exists along the length of the leading edge vortex, and this causes a pressure distribution. This pressure distribution then causes axial flow through the leading edge vortex, thereby stabilizing it. Liu and Kawachi [91] observed axial flow in

the leading edge vortex over 60-70% of the wing span. At this point, instabilities cause the leading edge vortex to break down, separate, and join the tip vortex.

Birch and Dickinson [15] propose that stabilization comes from the tip vortex creating downwash and lowering the effective angle of attack. Shyy and Liu [133] also address the controversy over the stabilizing mechanism of the LEV. The mechanism proposed by Ellington, axial flow, and the mechanism proposed by Dickinson, downwash, appear to both be applicable at their respective Reynolds number ranges. Axial flow is more prominent at higher Re; however, LEVs on wings at lower Reynolds number remain attached because the weaker LEV is less susceptible to breakdown.

Both the LEV and TEV consist of two smaller, co-rotating vortices which merge in the early stages of flow separation [111]. A detailed description of the vortex system on a flapping wing is provided by Ramasamy and Leishman [126]. At Re = 15,500, multiple vortices were found on the wing's suction surface. As soon as an LEV sheds, another takes its place, resulting in many vortices moving aft along the wing (see aldo Tarascio [150].) The LEV, despite having substantial axial flow, is unstable and sheds. However, since there is always at least one on the wing, high lift is maintained. Root and tip vortices also shed, after which they move toward each other and down, causing lift.

The leading edge trailing edge switching mode has received far less attention than the standard hovering or standard plunging modes. Force generation for a wing in this mode has been examined by Sunada et al [140]. Four vortices are present: a primary vortex at both the leading and trailing edges, and two smaller vortices. Tang et al [149] performed computations both for the normal hovering mode and the leading edge trailing edge switching mode, and found the latter to be beneficial at low Reynolds numbers. For example, Tang et al [149] report a 38% increase in average lift with the leading edge trailing edge switching mode compared to normal hovering at Re=100. Liu and Kawachi [91] investigated this mode as one of their validation cases. Their investigation revealed a primary leading edge vortex which grows throughout the stroke and sheds during the flip. This vortex is responsible for force generation, with lift being greatest right after shedding.

2.6. CRITICAL POINT THEORY

Critical point theory was developed by Oswatitsch [110] and Lighthill [88] for surface flows, but has been extended to wake flows and flows along symmetry planes ([115], [153], [177], and [178].) It is useful for analyzing flow features in CFD post-processed images and also particle image velocimetry (PIV) images. Critical points arise in systems of first order ordinary differential equations. The mathematical theory behind critical points is derived by Chong et al [23] and Tobak and Peake [153], who derive a pair of autonomous ordinary differential equations for velocity components near a surface. Singular, or critical points, are points where skin friction or vorticity become zero, or alternatively, where streamline slope is indeterminate. Local solutions to the continuity and Navier-Stokes equations can be found as series expansions about singular points. There are three main types of critical points, namely focus, node, and saddle. Biffurcation lines, while obviously not points, are also used [177].

Critical points can be stable or unstable. They also have meanings for the flow in their vicinity. Nodes occur where streamlines converge, and indicate separation (N^-); they also occur where streamlines diverge, and indicate attachment (N^+). The negative and positive superscripts are also referred to as stable and unstable, respectively. Saddle points, S, are where streamlines intersect. Lines emanating from them, called separatrices, separate one set of skin friction lines from another set; typically separated are sets of skin friction lines emanating from neighboring nodes. The occurrence of a saddle point is a necessary, but not sufficient, criteria for separation. Local, or open, separation does not have a saddle point on the bifurcation line, while global, or closed, separation does. Foci occur where there is an inward (F^-) or outward (F^+) swirling of streamlines, meaning separation and attachment, respectively. Foci extend outward into the fluid as a vortex filament; thus, foci imply vortices. If a focus occurs, a saddle point also occurs. This allows for global separation, where a bifurcation line proceeds from a saddle into a focus. Bifurcation lines are lines to which skin friction lines are asymptotic. Positive bifurcation lines, BL^+, indicate attachment with streamlines diverging from it. Negative bifurcation lines, BL^-, indicate streamlines merging to a single line and then separating. See Figure 2-5 for sketches of these critical points.

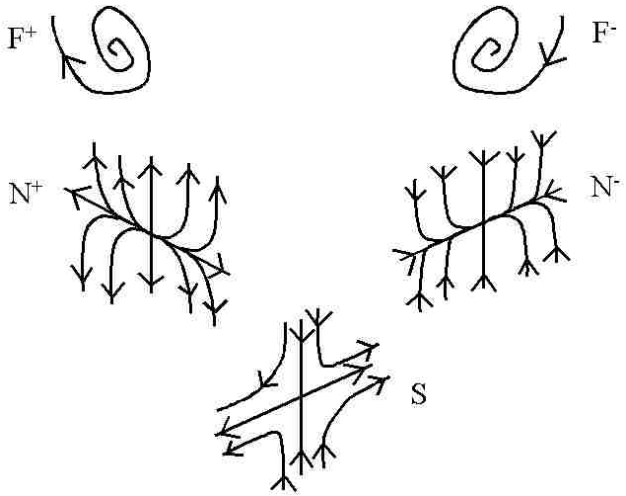

Figure 2-5: Critical points.

3. EXPERIMENTAL METHODOLOGY

This chapter details the experimental design used for this research. It begins with the physical arrangement of the experiment and apparatus. Then, the technique of particle image velocimetry (PIV) is explained and its setup is presented. The chapter concludes with an explanation of flow visualization.

3.1. EXPERIMENTAL ARRANGEMENT

The experiments presented herein were conducted in an aquarium filled with deionized water. Resting on the top of this aquarium were mechanisms to move the airfoil in a flapping motion or in a pitching motion. An aquarium, being glass walled, innately allows excellent optical access. This characteristic was exploited for flow visualization and particle image velocimetry experiments.

Figure 3-1 shows the arrangement used in these experiments. A Labview virtual instrument (VI) was written to control the system. It instructs the stamping program to begin, and fires the two PIV lasers. As the DC motor rotates the mechanism to flap or plunge the wing, an encoder attached to that shaft sends a signal to the Labview interface every degree and also an index pulse once per rotation. This was set manually to occur at the left hand extreme of the motion. The rotation signal and laser trigger can be sent at any time relative to the index pulse, allowing image acquisition at any point in the wing's motion. It also allows for various types of flip, namely advanced, symmetric, or delayed flip. A digital camera connected to a second computer then records image pairs for PIV analysis.

Computer 1 possesses Labview and a BASIC Stamp program called StampW. These programs control the timing of the experiment. Labview sends a signal to the servo, which controls pitching, and also to the delay generator, which controls the duration of, and separation between, laser pulses. StampW controls that pitching servo. Various angles of attack can be obtained by altering this program. A DC power supply drives the DC motor responsible for flapping and plunging the airfoil. Finally, a scientific grade megapixel camera, connected to computer 2 and controlled by the image

acquisition program Epix, can be used for particle image velocity and for flow visualization.

A mechanism to perform a plunging and pitching motion was designed and appears in Figure 3-2, along with the flapping mechanism that it replaces. The plunging mechanism produces a symmetric, sinusoidal harmonic motion, whereas the flapping mechanism does not. Nonsinusoidal wing trajectories can produce higher thrust than sinusoidal trajectories [69], but are not considered here. The flapping mechanism is a two bar mechanism, and the plunging mechanism is a Scotch yoke mechanism. Appendix A contains blueprints for the plunging mechanism.

Reduced frequency was adjusted by means of the selectable lengths available on the two mechanisms. The flapping mechanism has three holes about which the bar connecting the wing to the connecting rod can pivot, as is visible in Figure 3-2. This mechanism's reduced frequency range is from 0.09 to 0.19, but was found to be unreliable with the larger wings. The plunging mechanism has a much larger reduced frequency range, 0.1 to 0.47. The plunging mechanism has five holes on the wheel allowing for several horizontal lengths of travel. There is an inverse relationship between travel distance and reduced frequency, so the shorter radii correspond to higher reduced frequencies. The three equations below define these experimental parameters, where $\overline{U}$ is the average velocity, S is the distance swept by the wing in meters, f is the flapping frequency in Hz, c is chord length in meters, and ν is the coefficient of kinematic viscosity in m^2/s.

$$\overline{U} = 2S\ f \tag{11}$$

$$\mathrm{Re}_c = \frac{\overline{U}\,c}{\nu} = \frac{2S\ f\ c}{\nu} \tag{12}$$

$$k = \frac{f\ c}{\overline{U}} = \frac{c}{2S} \tag{13}$$

The working medium was water to allow a much lower Reynolds number than would be possible with air. Four thin, flat plate wings were cut out of 2mm thick Lexan and were used in this investigation. Two are rectangular in planform, and the other two

have a semi-elliptical planform. Each of the two pairs consists of one with a smaller, 50mm chord, and one with a larger, 75mm chord. All four wings have a 150mm span. Thus, the aspect ratios are three for the smaller chord and two for the larger chord wings. These wings are shown in Figure 3-3 and Figure 3-4, where the two holes at the root of each wing allow attachment to a rod that connects it to the servo motor responsible for pitching. This servo motor is mounted on a chassis, which is then connected to the flapping or plunging mechanism.

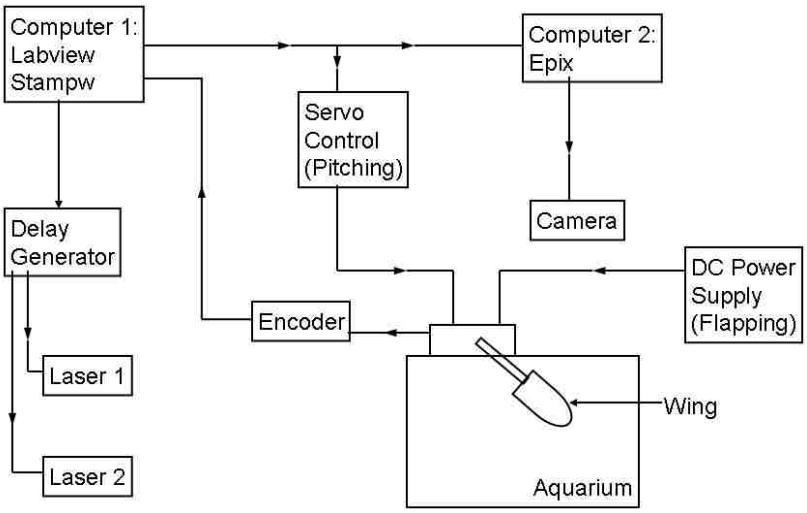

Figure 3-1: Experimental arrangement.

Figure 3-2: Flapping (left) and plunging (right) mechanisms.

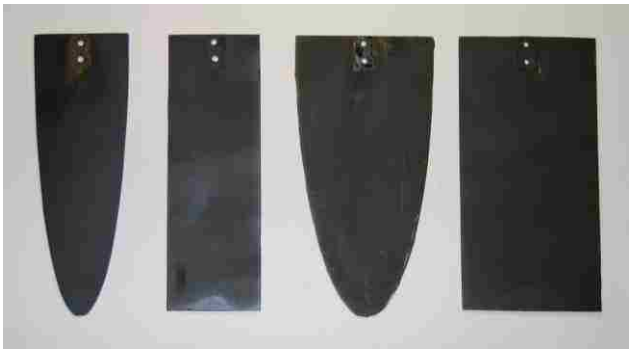

Figure 3-3: The four wings used in the experimental work.

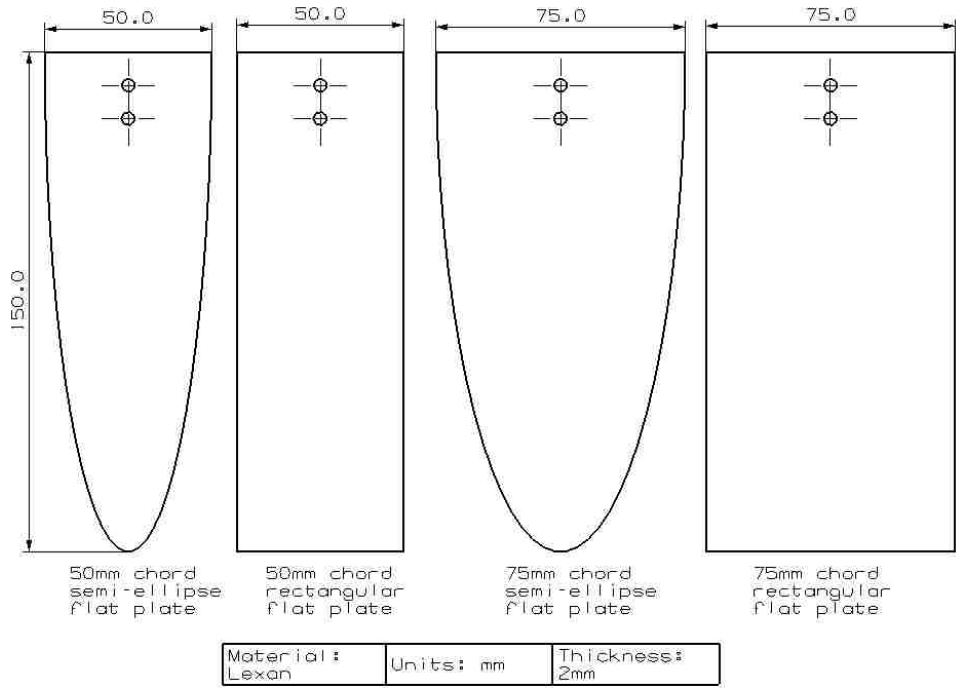

Figure 3-4: Drafts of the four wings used.

The figures below explain the terminology of a wing, the wing's motion, and its related coordinate system. A wing has a leading and trailing edge, a root and a tip. Cambered wings are curved, as shown in the figure, whereas non-cambered wings are flat plates. Chord is the dimension in freestream dimension, and span is perpendicular to it. As a wing plunges or flaps towards one extreme point of its motion, it maintains a constant angle of attack prior to flipping, which is a pitching motion. The wing then

reverses and flaps or plunges towards the other extreme point of its motion where it flips again. This flip can occur in advance of, symmetric with, or delayed until after motion reversal. The flapping images here use delayed flip, whereas the plunging images use symmetric flip.

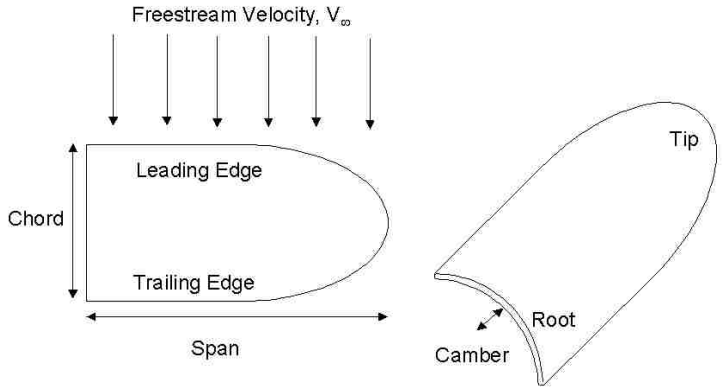

Figure 3-5: Wing terminology.

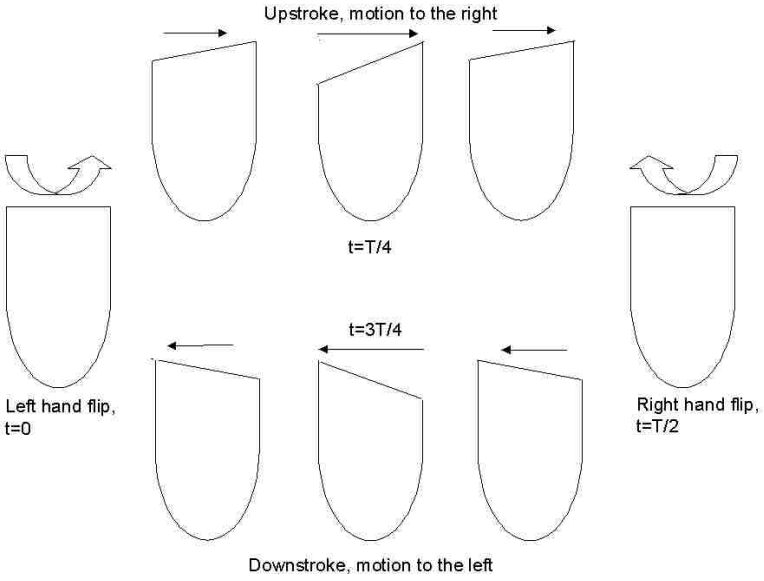

Figure 3-6: Wing motion, flapping or plunging and symmetric pitching.

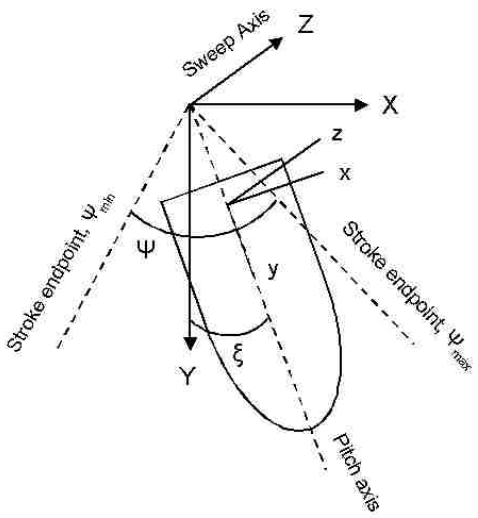

Figure 3-7: Coordinate system.

Since the Labview program is key to these experiments, a word on its operation is warranted. This program's front panel appears in Figure 3-8, and controls most of the parameters for these experiments. The absolute frequency at which the wing flaps or plunges is input into the Labview program. The most important of these timing parameters is the initial delay for the servomotor, the time between the pitching pulse and activating the servomotor. There is an identical time parameter for the PIV system, which sends a trigger pulse at a certain time after the index pulse. Adjustment of this number allows images to be acquired at any point in the airfoil's motion. Also, the Labview program produces a certain number of pulses for the servomotor responsible for pitching the wing.

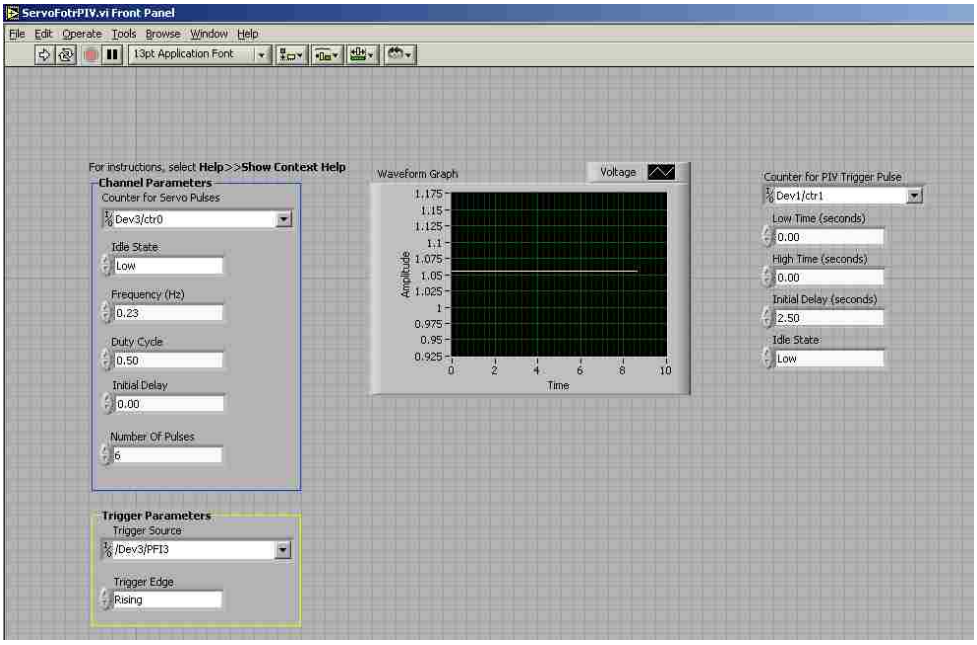

Figure 3-8: Labview experimental interface.

The remainder of this chapter details the background necessary to comprehend these experimental techniques and the methodology for the experimental methods used herein: particle image velocimetry and flow visualization.

3.2. PARTICLE IMAGE VELOCIMETRY: BACKGROUND

Particle image velocimetry (PIV) is an incredibly important technique in experimental fluid mechanics. The first use of this term was by Adrian in 1984 [1]. This technique, as well as many other experimental fluid mechanics techniques, is well described in the textbook edited by Goldstein [51]. It is also the subject of an entire book [119]. Adrian [4] has also written a recent review article on the subject. Digital particle image velocimetry, or DPIV, its operation and its advantagesover PIV are described by Willert and Gharib [175] and illustrated with the example of a vortex ring.

The technique itself is conceptually simple: finding velocity vectors from displacement vectors and the time interval between them. However, PIV in practice is not so simple, as it involves several pieces of expensive equipment and software, has

optics to be aligned, seeding density to be optimized, and some kind of correlation used to determine displacement vectors. The basics of PIV are described here in this section, and a diagram of a typical system is provided in the next section, along with a description of the setup used in this research.

Essentially, a PIV system consists of particles (markers) seeded into the flow, which are illuminated and imaged at two times. Since the marker particles are moving, a finite exposure time image of them will result in a streak corresponding to the particle's motion in that finite time. Thus, the exposure time must be short. Marker particles must be small in order to accurately follow the flow, and this results in low reflected light brightness. Both of these characteristics necessitate a light source that is intensely bright and emits in a short period of time, usually a laser. Two conflicting effects [5] determine the optimal particle size: it is easier to detect large particles, but displacement measurement accuracy improves with decreasing particle size. Two lasers whose light is converted into a plane provide this illumination. A camera is placed perpendicular to that plane, thus allowing displacement in two dimensions along the plane to be determined.

PIV image analysis begins by dividing the image into small areas called interrogation spots. These areas are analyzed with cross correlation and a displacement vector, corresponding to the correlation peak, is calculated for each area. Velocity vectors then come from the displacement of these particles divided by the time between the images.

Image density is the parameter that defines the type of PIV being used, namely autocorrelation for low image density and cross correlation for high image density. Image density is given by

$$N_I = C\Delta z_0 \frac{\pi d_I^2}{4M^2} \tag{14}$$

where N_I is image density, C is the particle concentration (number of particles divided by volume), Δz_0 is the depth of the light sheet, d_I is the interrogation spot diameter on the image plane, and M is the camera's magnification. Low image density PIV occurs when N_I is much less than one, and high image density PIV occurs when N_I is at least ten or

twenty. Since in low image density PIV the odds of finding two or more particles in the same interrogation spot are remote, the two particle images in a double exposure must be of the same particle at the two different times. If three or more images occur in the interrogation spot, it is ignored. Displacement vectors come naturally, and so does velocity. However, this ease comes at the price of few randomly located vectors in the flow: less velocity information is present. Faulty velocity vectors also occur and can be removed by post-interrogation.

High image density PIV has the opposite of the advantages and disadvantages in low image density PIV. Here, velocity vector determination is much more complicated, but it results in more information. Since many particle images occur in each interrogation spot, a statistical technique called cross correlation must be used to determine the displacement vector that will translates the first set of particle images to be coincident with the second set. This correlation is defined by

$$R(\vec{s}) = \int_{spot} I(\vec{X}) I(\vec{X} + \vec{s}) d\vec{X} \tag{15}$$

where $\vec{s}$ is the separation vector and I is interrogation spot's image intensity. Three peaks result from this analysis. The first is when $\vec{s}$ is zero, meaning that the each image correlates with itself. Then, there are two other smaller peaks at a displacement of $\pm\Delta\vec{X}$, which represents the first image correlating with the second, and the second image correlating with the first. Keane and Adrian [72] discuss the advantages of cross correlation over auto-correlation and provide parameters for optimal performance. After determining the centroid of the positive correlation peaks, the velocity is computed from

$$\vec{\mu}(\vec{x}, t) = \frac{\mu_{D+}}{M\Delta t} \tag{16}$$

where μ is a velocity estimate, μ_{D+} is the centroid of the positive correlation peaks, and M is magnification. This then yields a volume averaged velocity in the interrogation

spot. A commercially available program, PIVview [119], was used in this research to perform cross correlation.

Keane and Adrian [71] provide optimal parameters for a typical PIV system. At least 15 particles should appear in each interrogation spot. The ratio of the highest to the second highest correlation peak should be between 1.2 and 1.5. Particle displacements should not exceed one quarter of the interrogation spot width. To ameliorate three-dimensional effects, the displacement perpendicular to the light sheet should not exceed one quarter of the light sheet width.

3.3. PARTICLE IMAGE VELOCIMETRY: EXPERIMENTAL METHODOLOGY

Figure 3-9 shows the optics associated with the PIV system, and it is a standard optical arrangement. Figure 3-10 is a ray diagram of the laser's optics and also indicates the illuminated area. The lasers used here are frequency doubled Nd:YAG operating at 532 nm and 1064 nm, 170 mJ/pulse at 532nm. Partially reflective mirrors reflect the visible light (532 nm,) and infrared absorbers absorb the 1,064 nm light. The visible laser beams are converted into a light sheet 0.1mm thick by a cylindrical lens. By rotating this lens, this system can illuminate either a spanwise plane or a chordwise plane, as shown in

Figure 3-11. When the cylindrical lens is horizontal, a vertical light sheet is formed, and vice versa. All PIV and flow visualization images here used a horizontal light sheet reflecting light down to a mirror. A camera placed in front of the mirror records images as if the observer were looking from the bottom upwards to the horizontal imaging plane. Further focusing of the light sheet is accomplished by a convex spherical lens. A plane mirror mounted underneath the aquarium reflects light from the horizontal illumination plane to the camera. Figure 3-12 shows how the laser light sheet intersects the wing at different spanwise locations throughout the flap, a problem not encountered with plunging motion. Timing for the laser pulses (and attendant image acquisitions) is controlled by a delay generator according to Table 3-1. In that table, T is external trigger from LabVIEW. Adjusting these parameters allows for different separations between laser pulses and images.

Proper seeding is important for PIV, with the recommendation to have at least 20 particles in each interrogation window. Silver coated microspheres are the seed material used here. They are neutrally buoyant, small, and highly reflective. Images are acquired by a Kodak Megaplus Camera Model ES 1.0, operating in triggered double exposure. Images can be acquired with time separations as little at 5 μs, although 100 μs was used here. Images can be taken at any time relative to the encoder's index pulse, thus allowing for phase-locked measurements. Images were acquired by an EPIV XCAP Lite v2.2 program, and are exported as tiff files for processing in PIVview.

The PIVview software used in this research has many options to control the process. The first of these is selecting the interrogation spots, their size and overlap. Smaller interrogation spots yield higher resolution, but at the cost of less displacement information in the cross correlation. Larger interrogation spots have the opposite situation: lower resolution, but better correlation. Three cross correlation algorithms are available: standard single pass interrogation, multi pass interrogation, and multi grid interrogation. The standard algorithm performs the cross correlation analysis once. The multi pass algorithm performs cross correlation an adjustable number of times utilizing pixel shifting. This technique shifts the interrogation spots by the previous passes displacement vector to reduce the number of particles that exit the interrogation spot and thereby increase correlation. Multi grid interrogation, which also uses pixel shifting, first evaluates the image pairs with large interrogation spots and then reduces their size. Typically, a 32X32 grid with 50% overlap was used here.

Several options also exist for peak detection, but the standard three point Gaussian fit was used here. Peak detection is necessary for outliers, vectors that do not fit the expected pattern. A vector is determined to be an outlier if its velocity is too large or if it substantially differs from its neighbors. Such a vector can then be replaced by an interpolation of neighboring vectors or by a different correlation peak for that interrogation spot. Displacement error is estimated to be around 5%.

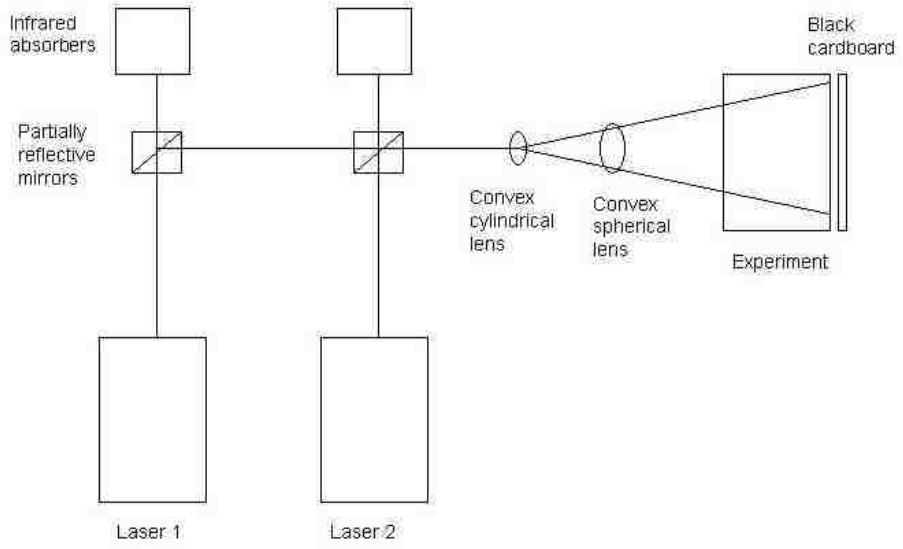

Figure 3-9: PIV optics.

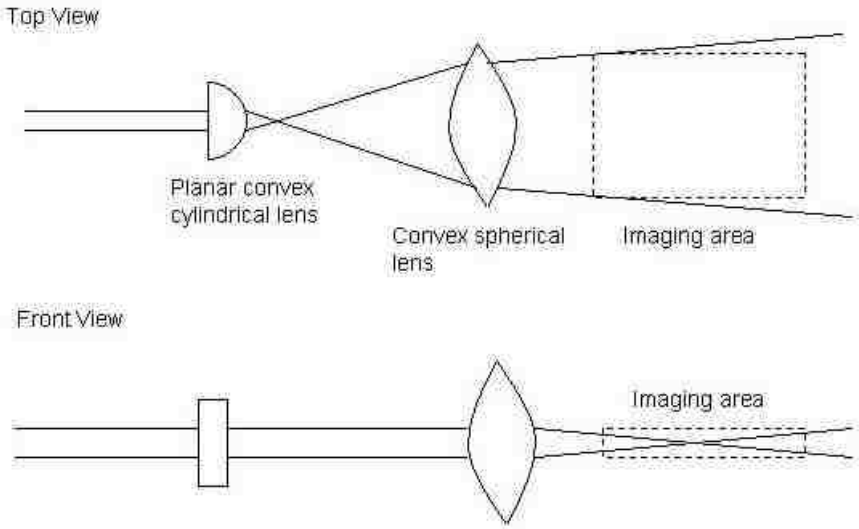

Figure 3-10: Ray diagram and imaging area.

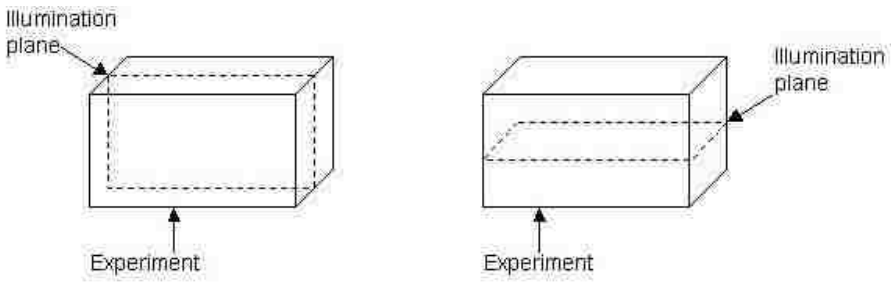

Figure 3-11: Illumination planes: spanwise on left, chordwise on right.

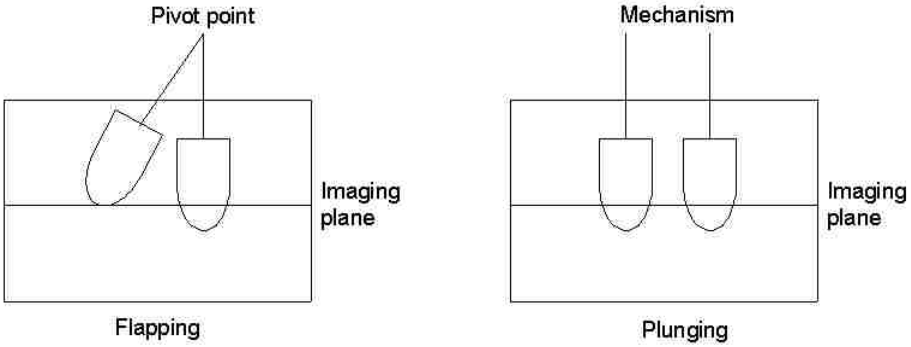

Figure 3-12: Laser light sheet intersects wing at different spanwise locations.

Table 3-1: Timing parameters.

Channel	Timing	Device
A	A = T + 20 µs	Laser 1 lamp trigger
B	B = A + 5 ms	Laser 2 lamp trigger
C	C = A + 200 µs	Laser 1 Q switch
D	D = B + 200 µs	Laser 2 Q switch

3.4. FLOW VISUALIZATION

Quantitative and qualitative flow visualization in water is mostly performed by either of two methods, hydrogen bubble formation and dye injection [51]. A wire in a DC circuit forms hydrogen bubbles, and these bubbles then follow the flow field. The wire should be small, such as a 50 µm platinum wire, and is the cathode, or negative terminal. A graphite rod inserted into the water is the anode, or positive terminal.

Hydrogen bubbles are formed at the cathode, and oxygen bubbles are formed at the anode. The addition of a small amount of an impurity promotes bubble formation. 0.15 g of Na_2SO_4 per liter of water was found to be sufficient [51]. Bubble sizes are small enough to allow buoyancy to be neglected. This technique dates to Geller published in 1955 [50], and much of the important early work was conducted at ONERA [49]. Dye can be injected into a flow by bottles of dye, which are usually pressurized by nitrogen canisters. However, the injection velocity must match the flow velocity to ensure a stable dye filament and avoid disturbing the flow. If dye is injected at an object's surface, there must be no velocity normal to that object's surface. Otherwise, the boundary layer will be disturbed.

Once dye is injected or hydrogen bubbles are formed, images are taken with a camera and a light source. Such a system is less complicated than PIV since lasers are not required, nor is post processing required to reveal qualitative flow information. Lasers can, however, be used to illuminate a plane in the flow. Using inexpensive and readily available equipment, quantitative information can be obtained from both hydrogen bubble and dye injection flow visualization [106].

4. RESULTS

The results chapter is divided into three main sections. The first of these is CFD of low Reynolds number ($Re_c = 500$) stationary wings at constant angle of attack. The second main section contains results from the experimental work, PIV for both flapping and plunging, and flow visualization for the plunging motion. The final main section in this chapter discusses dynamic mesh CFD for a flapping wing.

4.1. LOW REYNOLDS NUMBER, STATIONARY WING, CFD

This section discusses the work presented in references [144] and [145]. It is divided into four subsections. First, the simulation parameters are defined, and then force results are presented. The third subsection is streamlines, and the final subsection contains surface streamtraces investigated with critical point theory.

4.1.1. Simulation Details. In this section, the effects of angle-of-attack and camber and planform shape on the aerodynamics of thin wings of uniform thickness are investigated. Thing wings were chosen because insect wings tend to be thin and have sharp leading and trailing edges. Thus, it is hypothesized that they will perform better than conventional or elliptic cross section wings at low Reynolds numbers and high angles of attack.

Four wings were investigated here. Two of the wings have a rectangular planform, one without camber and one with camber. The other two have a semi-elliptical planform, one without and one with camber. All four wings have the same chord, span, and thickness, and the two cambered wings have circular arc sections and the same amount of camber. The geometric parameters are: 15cm length, 5cm chord, 0.05cm thickness, and 0.125cm camber, with an aspect ratio of 3 for the rectangular wings, 3.82 for the semi-ellipse wings. The wings have sharp leading and trailing edges and are unswept. The computational domain housing these wings consists of a small hemisphere, with 20cm radius and higher grid density, inside a larger hemisphere, with 80cm radius and a lower grid density. The base plane of the computational domain is a symmetry plane.

Grids were generated for all four wings to be as similar as possible. A triangular surface mesh was used on three of the four wings, but a quadrilateral surface mesh was sufficient for the non-cambered, rectangular wing. This change in mesh type was determined to not affect the results. From this surface mesh, tetrahedral volume meshes were created. Between approximately 850,000 and 900,000 cells were generated for all four wings. The grids were of high quality and results were grid independent. Forces computed with a grid with an additional 50% as many cells differed from the original grid by less than one percent. Also, single precision and first order algorithm were found to be satisfactory. Figures Figure 4-1 and Figure 4-2 show the computational domain including the inflow and outflow surfaces and symmetry plane. The surface mesh on the cambered semi-ellipse wing and the inner portion of the symmetry plane appears in Figure 4-3 and the surface mesh on the cambered rectangular wing appears in Figure 4-4. All four wings are included in Figure 4-5. Chord is in the x direction, as is the freestream flow. Span in the y direction, and camber in the z direction. The xz plane is a symmetry plane. The –x half of the hemispherical surface is set to be inflow, and the +x half is outflow (Figure 4-2).

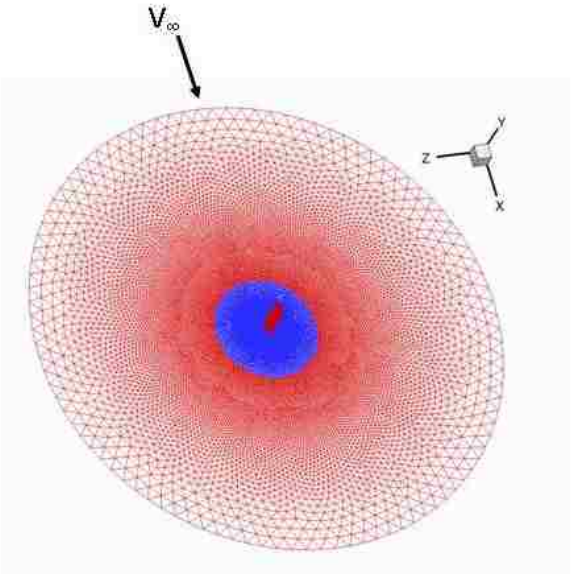

Figure 4-1: Cross section of computational domain, showing the wing and circular base surfaces.

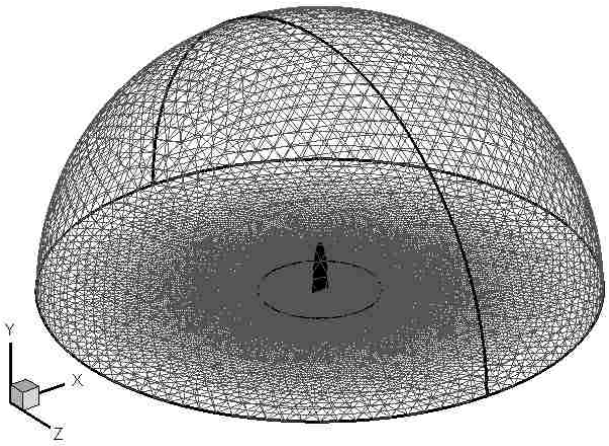

Figure 4-2: Hemispherical computational domain, showing the wing and circular base surfaces. The circular arc divides the hemispherical surface into inflow and outflow boundaries.

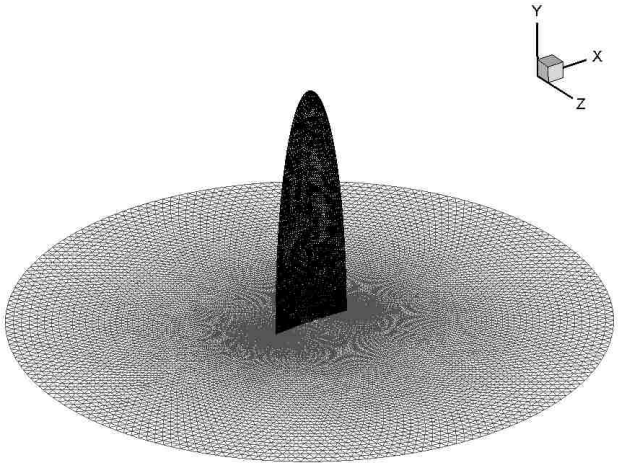

Figure 4-3: Semi-ellipse cambered wing and inner portion of meshed symmetry boundary.

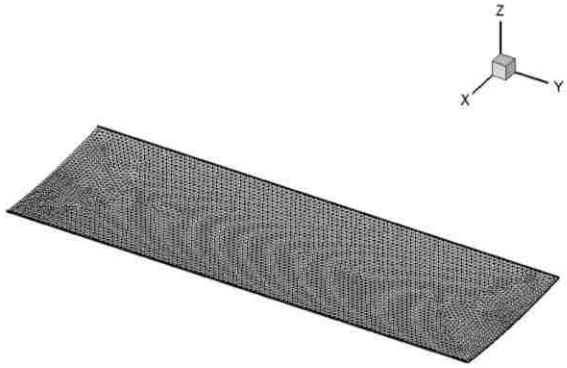

Figure 4-4: Triangular surface mesh on rectangular cambered wing.

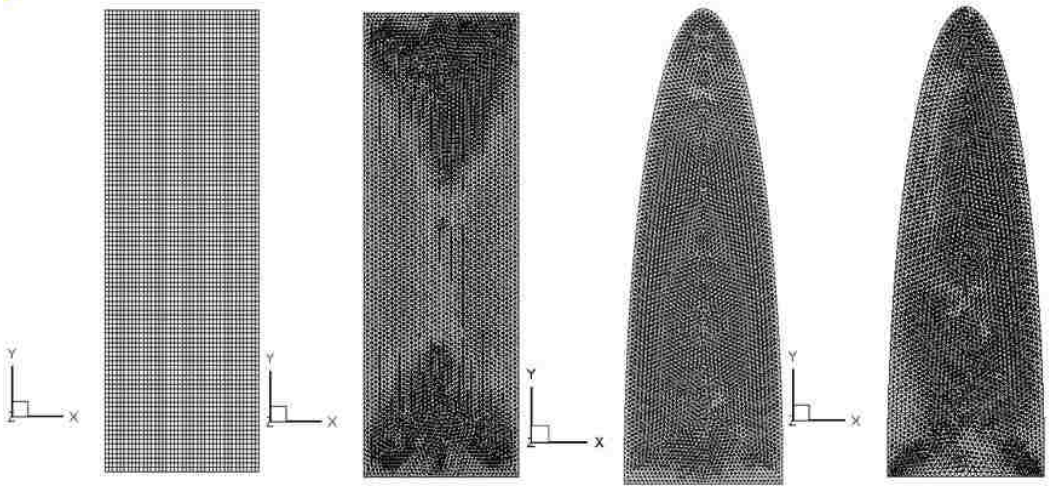

Figure 4-5: Surface meshes on all four wings: rectangular, without and with camber, semi-ellipse, without and with camber.

The simulations reported in this section used the commercially available flow solver FLUENT [44]. Reference [62] describes the pertinent features of this flow solver. That reference also established the success of a mesh like those used here to analyze laminar flow problems at this present low Reynolds number. Young et al [182], in a dynamic mesh study of a flapping wing at Reynolds numbers from 100 to 50,000, found turbulence to have no effect. Flow separation is fixed to the sharp leading edge, and is not affected by turbulence. Similarly, the two-dimensional CFD study by Kunz and Kroo [75] employed a laminar, steady solver. However, they note that unsteady trailing edge

separation degrades convergence at Re = 1,000. The residuals and force coefficients were monitored during the runs to determine the number of time steps to be used. The presented results are for flow times of approximately 50 seconds, which was found to be sufficient for the solution to reach either steady or quasisteady state. Figure 4-6 illustrates the meaning of steady state force production. All subsequent data were acquired at a peak in this cycle. The frequency of these oscillations ranges from 0.34 Hz at $\alpha = 35^o$ to 0.26 Hz at $\alpha = 45^o$, with a typical amplitude of 0.02.

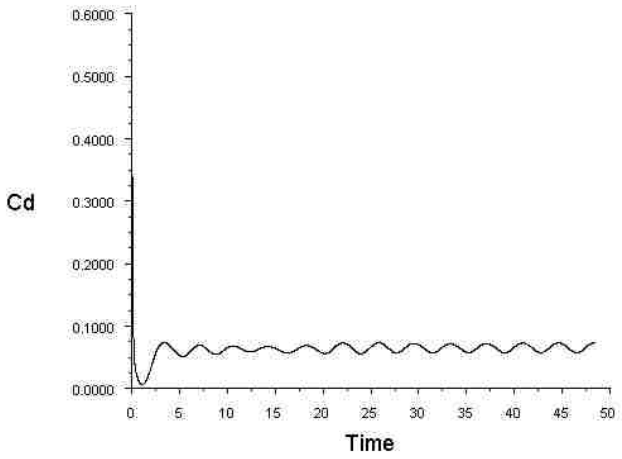

Figure 4-6: Quasi-steady state force production.

Our computational technique has been validated by comparing computed data to two dimensional cylinder flow and two data sets. For the cylinder flow, we compute C_D = 1.17, which is in excellent agreement with the correlation presented by White [173], where C_D = 1.16. The first data set is from the 3D experimental study of Sunada et al [142], where a non-cambered rectangular wing of aspect ratio of 7 was dragged through a water tank at Re = 4,000. They report experimental error of no more than 8% in C_L and C_D. The second set is from the 2D computational work of Kunz and Kroo [75], which includes the drag polar for a NACA 0002 airfoil at Re = 1,000. Computed results were generated using the procedure described above, and Table 4-1 and Table 4-2 show this comparison. Agreement is generally good, and is better for drag than for lift. Minor

differences in grid generation, and the use of the steady flow assumption in my simulations, are assumed responsible for these discrepancies. Those problems will not arise in the results presented here, since a grid study was conducted and the unsteady flow solver was used.

Table 4-1: Comparison to Sunada et al [142].

α, ^{o}	C_L			C_D		
	From Ref.	Computed	% Difference	From Ref.	Computed	% Difference
15	0.87	0.84	3.4	0.28	0.29	3.6
20	0.90	0.90	0	0.37	0.38	2.7

Table 4-2: Comparison to Kunz and Kroo [75].

α, ^{o}	C_L			C_D		
	From Ref.	Computed	% Difference	From Ref.	Computed	% Difference
0	0.00	0.00	0	0.10	0.10	0
2	0.18	0.17	5.6	0.10	0.10	0
4	0.34	0.30	12	0.11	0.11	0
8	0.55	0.53	3.6	0.13	0.13	0

4.1.2. Force Production. Figure 4-7 is a drag polar and shows lift and drag coefficients as functions of α for all four wings. However, it may be easier to see trends from Figure 4-8 and Figure 4-9, where coefficients of lift and drag are shown directly as functions of angle of attack. Moment coefficient about the quarter chord is plotted in Figure 4-10, and in Figure 4-11 for low angle of attack. Figure 4-12 plots the pressure coefficient at $\alpha = 10^o$. Lift coefficient peaks at $\alpha = 20^o$ for all wings except the non-cambered rectangular wing which peaks at $\alpha = 40^o$. A lift peak at 20^o has been

postulated in our research group's previous work ([60], [61], [62], and [63]) as the angle at which vortices preferentially shed, thus explaining the lift peak at that angle. Lift then decreases after this peak to its value at $\alpha = 30^o$. However, the behavior above this angle of attack differs for the different wings. C_L continues to decrease for both semi-ellipse wings, while C_L increases for the rectangular wings from $\alpha = 30^o$ to $\alpha = 40^o$ and then decreases beyond $\alpha = 40^o$. There is more similarity in drag polar behavior between wings of the same planform than wings of the same cambering. This indicates that planform shape is a more dominant factor than camber for the wings considered in this study. Coefficient of moment decreases with angle of attack, but at the highest angles of attack, it decreases much less for the rectangular wings than for the semi-ellipse wings. After stall, wings generally experience a decrease in moment coefficient. Moment coefficient does not show the typical trend at high Reynolds number, where the moment coefficient about the quarter chord is constant until stall. At low Reynolds numbers, the moment coefficient increases in magnitude.

Two possible explanations for the force peak and subsequent behavior are proposed. Vortex shedding occurs at 20^o angle of attack and causes additional lift, hence the peak at this angle. Vortices have shed above this maximum lift angle and no longer contribute to increase lift. The second possible explanation is similar to that of Selig [131] and involves the laminar separation bubble. Airfoils at low Reynolds numbers and high angles of attack have a large, laminar separation bubble on their suction surface. This bubble causes the resultant force vector to be nearly perpendicular to the wing at low Reynolds numbers. This vector tilts aft as α increases, thereby decreasing the vertical component (lift) and increasing the horizontal component (drag.) As α increases, the laminar separation bubble moves toward the leading edge and grows larger, which increases lift and also drag. When a certain angle of attack is reached, the bubble bursts and the wing stalls. As α increases beyond this value, the lift coefficient would decrease.

Two other predictable trends are visible. A cambered wing has more lift and more drag at the same angle of attack than a non-cambered wing, as the zero lift point is shifted for the cambered wing. Thus, the C_L peak for the cambered wing is greater than that for the non-cambered wing. Also, cambered wings develop lift even at $\alpha = 0^o$, but the non-cambered wing has no lift at $\alpha = 0^o$.

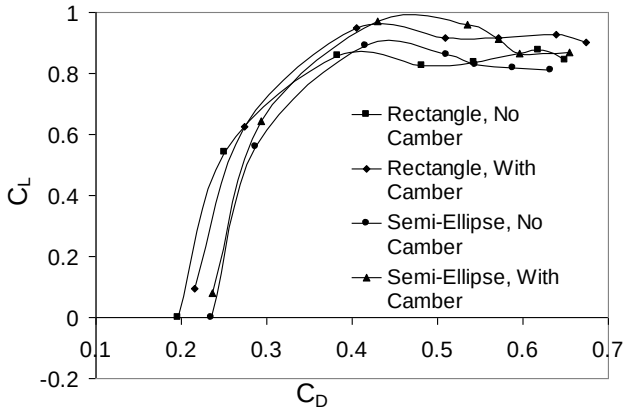

Figure 4-7: Drag polar for non-cambered and cambered rectangular wings. Rec=500.

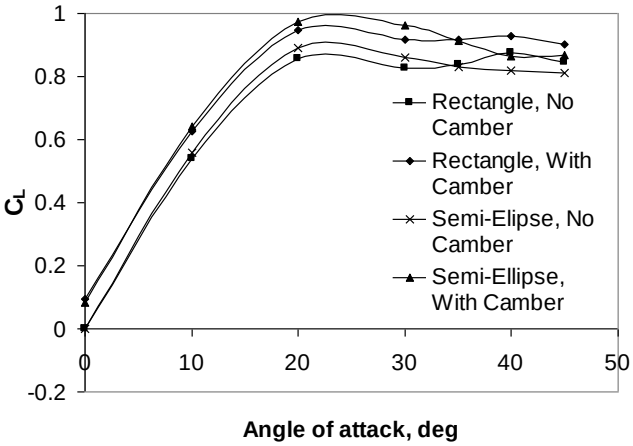

Figure 4-8: Lift coefficient curve.

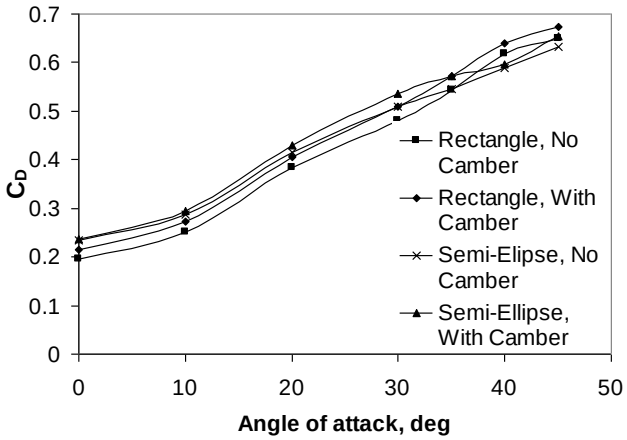

Figure 4-9: Drag coefficient curve.

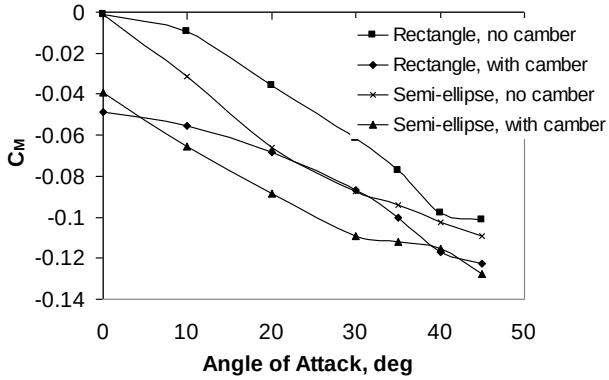

Figure 4-10: Moment coefficient about quarter-chord.

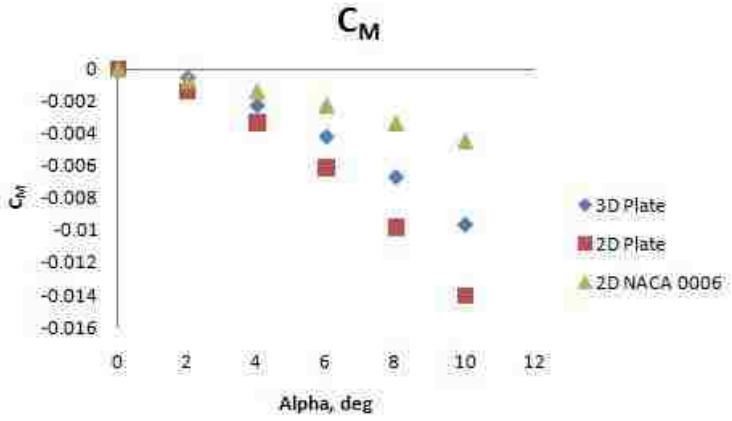

Figure 4-11: Moment coefficient for a 3D plate, 2D plate, and 2D airfoil at Re=500.

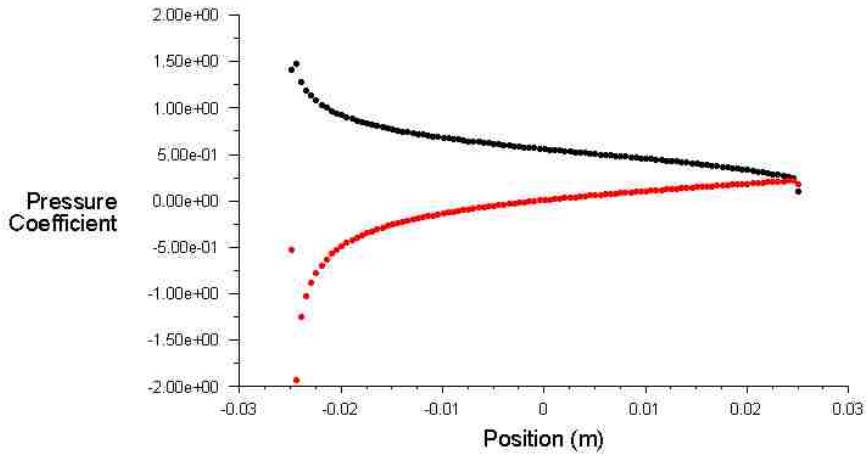

Figure 4-12: Pressure coefficient for flat plate at Re_c=500, $\alpha = 10^o$. Red is suction surface, black is pressure surface.

The lowest Reynolds number found in the literature is 1,000, in a paper by Kunz and Kroo [75], and it is to this work that comparisons are made. However, since their study was two dimensional and limited to low angles of attack, additional 2D cases were run at Re_c=500. As expected, lift coefficient is smaller and drag coefficient is larger at the lower Reynolds number than at the higher Reynolds number, as expected. For example, Kunz and Kroo report C_D=0.0998, while the value we computed for a 2D airfoil of the same chord and thickness as the wings in this study is C_D=0.162 at $\alpha=0^o$. Also, C_L at $\alpha=8^o$ is 0.553 at Re_c=1,000, but C_L=0.523 at Re_c=500. Kunz and Kroo [75] note the large drag and low lift to drag ratios, orders of magnitude different from high Reynolds number results. Two drag polars are presented at Re=1,000 in Kunz and Kroo [75]. Lift coefficient plateaus around $\alpha = 10^o$, as evident in their Figure 2, much lower than the value here. Flow visualizations shown later in this chapter reveal substantial separation for all angles of attack above 10^o. Table 4-3 shows force and moment coefficients at Re_c = 500 and Re_c = 5,000. Coefficient of lift and drag are both higher at the lower Reynolds number.

Table 4-3: Force and moment coefficients at two Reynolds numbers.

Re_c	$\alpha = 0^o$			$\alpha = 45^o$		
500	$C_L = 0.000$	$C_D = 0.196$	$C_M = -0.001$	$C_L = 0.845$	$C_D = 0.649$	$C_M = -0.101$
5,000	$C_L = 0.0016$	$C_D = 0.0627$	$C_M = -0.001$	$C_L = 0.544$	$C_D = 0.574$	$C_M = -0.115$

4.1.3. Flow Features. The figures in this subsection show streamlines for flow over the four wings studied. Some trends are present for all wings, such as the tip vortex and spiral vortex, and there are some features apparent in only one of the wings. These flow features are discussed below.

Figure 4-13 through Figure 4-16 show a top view of the flow over the four wings at seven angles of attack: 0^o, 10^o, 20^o, 30^o, 35^o, 40^o, and 45^o (labeled a – g, respectively). Figure 4-13 and Figure 4-14 are for the rectangular wings, without and with camber respectively, and Figure 4-15 and Figure 4-16 are their semi-ellipse counterparts. Corresponding streamline patterns in Figure 4-13 and Figure 4-14 for the rectangular wings, and Figure 4-15 and Figure 4-16 for the semi-ellipse wings can be used to determine the effect of camber on the flow field. Since they are substantial similar, the qualitative effect of this amount of camber on streamlines is small. At $\alpha = 0^o$ without camber (Figure 4-13a and Figure 4-15a) the streamlines are not perceptible altered in the view shown, and are only slightly disturbed with camber (Figure 4-14a and Figure 4-16a). Streamlines proceed straight aft of the wing forming a sheer without any spanwise curvature. At $\alpha = 10^o$ (Figure 4-13b - Figure 4-16b), only a minor tip vortex is present, but it becomes prominent beginning at $\alpha = 20^o$ (Figure 4-13c - Figure 4-16c). As α increases beyond this value, the tip vortex becomes steadily more prominent. The tip vortex curves the streamline sheet aft of the wing tip. Figure 4-13c and d without camber, and also Figure 4-14c and d with camber, show streamline curvature at the wing's root near the symmetry plane, indicating a spanwise variation. For the two rectangular wings, a spiral vortex forms at the tip; however, for the two semi-ellipse wings, a spiral vortex originates from the wing's root. Substantial vortices, which dominate large portions of the flow, form at angles of attack of 30^o and higher. A spiral

vortex forms on every wing except the cambered rectangular wing above 35^o, where it did not form until 40^o. Thus, camber enhances flow attachment and delays development of that vortex. Kunz and Kroo [75] also report the benefits of camber, and show camber promotes attachment.

Reversed flow, flow directed against the freestream, is present in the spiral vortex close to the wing's suction surface. The spiral vortex forms from the tip in both of the rectangular wings, and in the non-cambered semi-ellipse at 45^o. However, it forms from the root in the non-cambered semi-ellipse at $\alpha = 35^o$ and 40^o, and in the cambered semi-ellipse at $\alpha = 35^o$, 40^o and 45^o. This could indicate transverse flow from root to tip, and also indicates the importance of shape and camber. A spiral vortex is conspicuously absent on the cambered semi-ellipse wing at $\alpha = 45^o$. An explanation for this is not immediately apparent.

Flow features we referred to as dead fluid regions in previous work [144], regions with few or no streamlines, also appear at and above 35^o. At 45^o, it extends for the majority of the wing's span. However, as illustrated by Figure 4-17, these regions have been erroneously identified as dead fluid regions in the previous work [144]. While it is true that streamlines released from the points used to create these previous images do not go through those regions, streamlines originating from other areas, like those in Figure 4-17, do traverse those regions. These low streamline density regions with highly three-dimensional flow features are caused by the tip vortex lifting streamlines up above the wing and transporting them rootward. This is also responsible for sending many streamlines over to, and compressing them up against, the symmetry plane. Substantial spanwise flow is thus present toward the symmetry plane at higher angles of attack for these fixed wing cases. Also present in Figure 4-17 is an interesting flow feature near the root just aft of the leading edge. Here, the flow is reversed, and forms a spiral vortex from the root in the semi-ellipse wings. Taira and Colonius [147] also report a leading edge vortex which separates as a hairpin vortex and interacts with the tip vortex. However, the behavior of the spiral vortex is quite different from that shown above when the wing is not stationary, but undergoing complex motions such as flapping and pitching. This is discussed by Isaac et al [61], and later in this chapter.

Kunz and Kroo [75] provide a few figures of numeric streamlines. Trailing edge separation is apparent in them, and it occurs at higher angles of attack at lower Reynolds numbers. Their Figure 10 indicates a backwards S-shaped feature, where flow near the trailing edge is initially in the free-stream direction, reverses direction, and then returns to the free-stream direction. This is quite similar to some of the streamtraces along the symmetry plane in Figure 4-17. Figure 4-18 shows strealimes for the non-cambered rectangular wing at $\alpha = 45^{o}$ for both $Re_c = 500$ and 5,000. The spiral vortex is present but much smaller at the higher Reynolds number, as is the reversed flow region. Both trends are as anticipated.

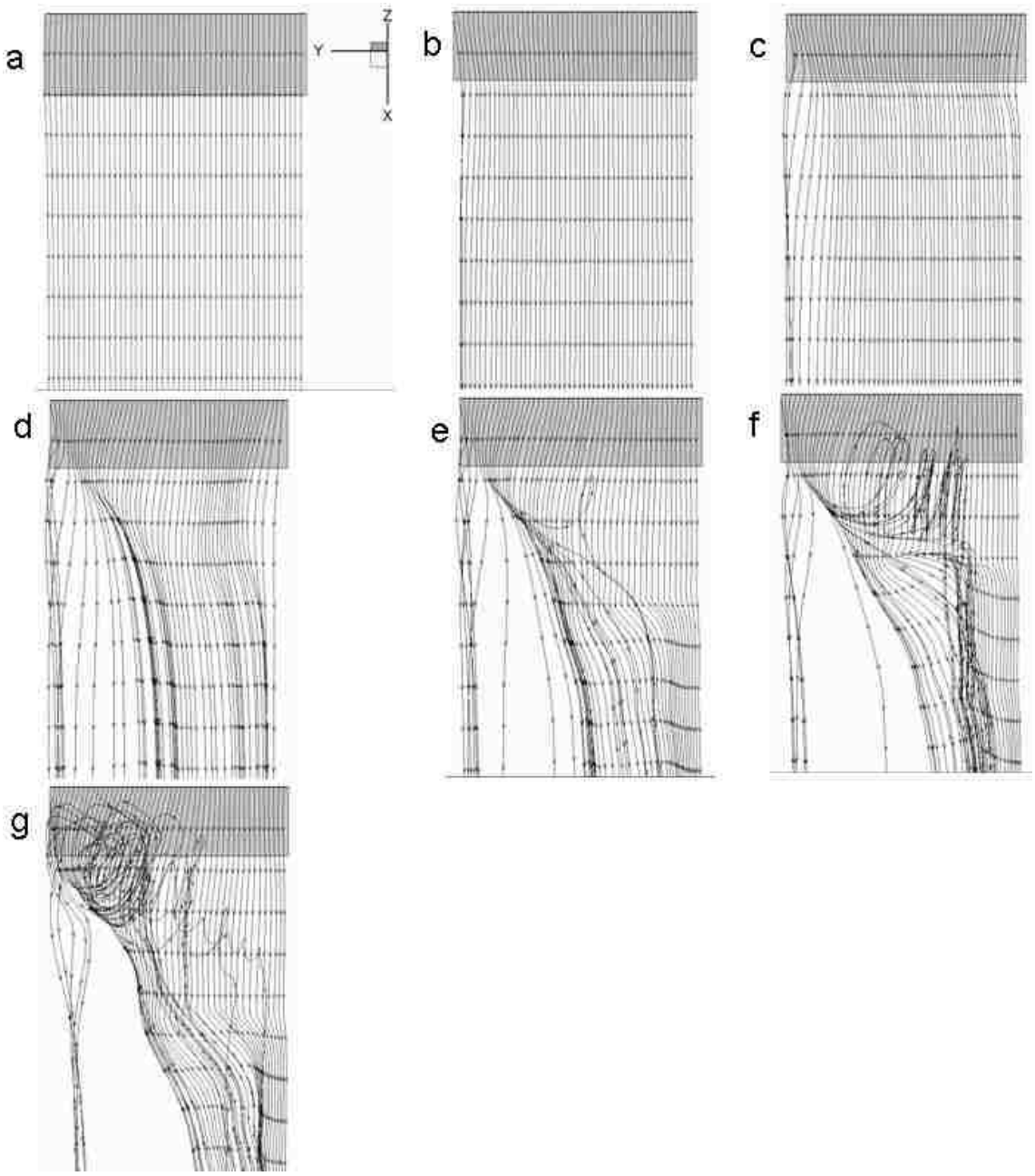

Figure 4-13: Streamlines for non-cambered rectangular wing viewed from top along a direction between the x and z axes. Axis is for orientation purposes. Flow is from top to bottom, tip is left and root is right. Beginning at top left, $\alpha = 0^o$, 10^o, 20^o, 30^o, 35^o, 40^o, and 45^o.

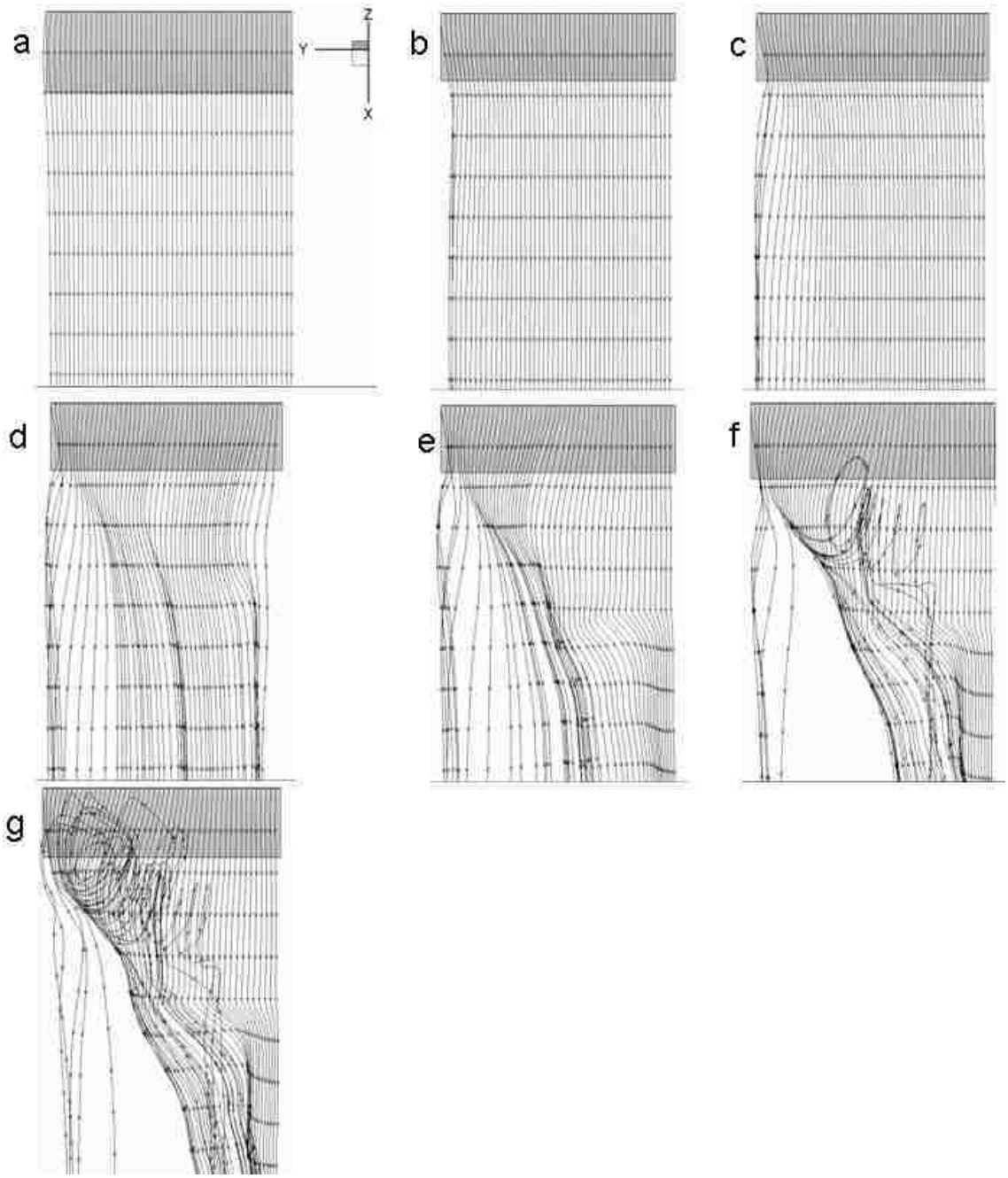

Figure 4-14: Streamlines for cambered rectangular wing. Viewing direction is same as in Figure 4-13. Axis is for orientation purposes. Flow is from top to bottom, tip is left and root is right. Beginning at top left, $\alpha = 0^o$, 10^o, 20^o, 30^o, 35^o, 40^o, and 45^o.

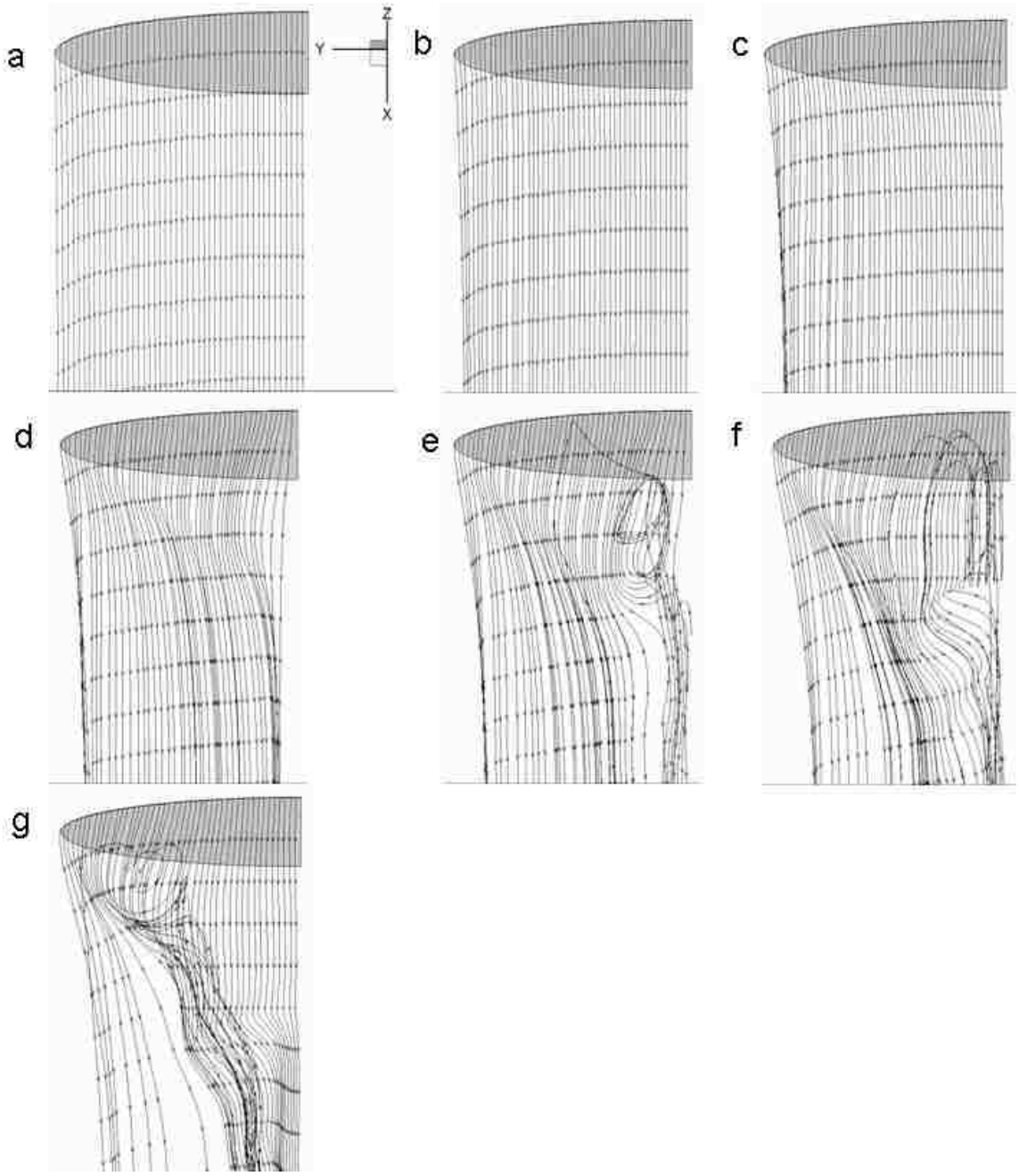

Figure 4-15: Streamlines for non-cambered semi-ellipse wing. Viewing direction is same as in Figure 4-13. Axis is for orientation purposes. Flow is from top to bottom, tip is left and root is right. Beginning at top left, $\alpha = 0^o$, 10^o, 20^o, 30^o, 35^o, 40^o, and 45^o.

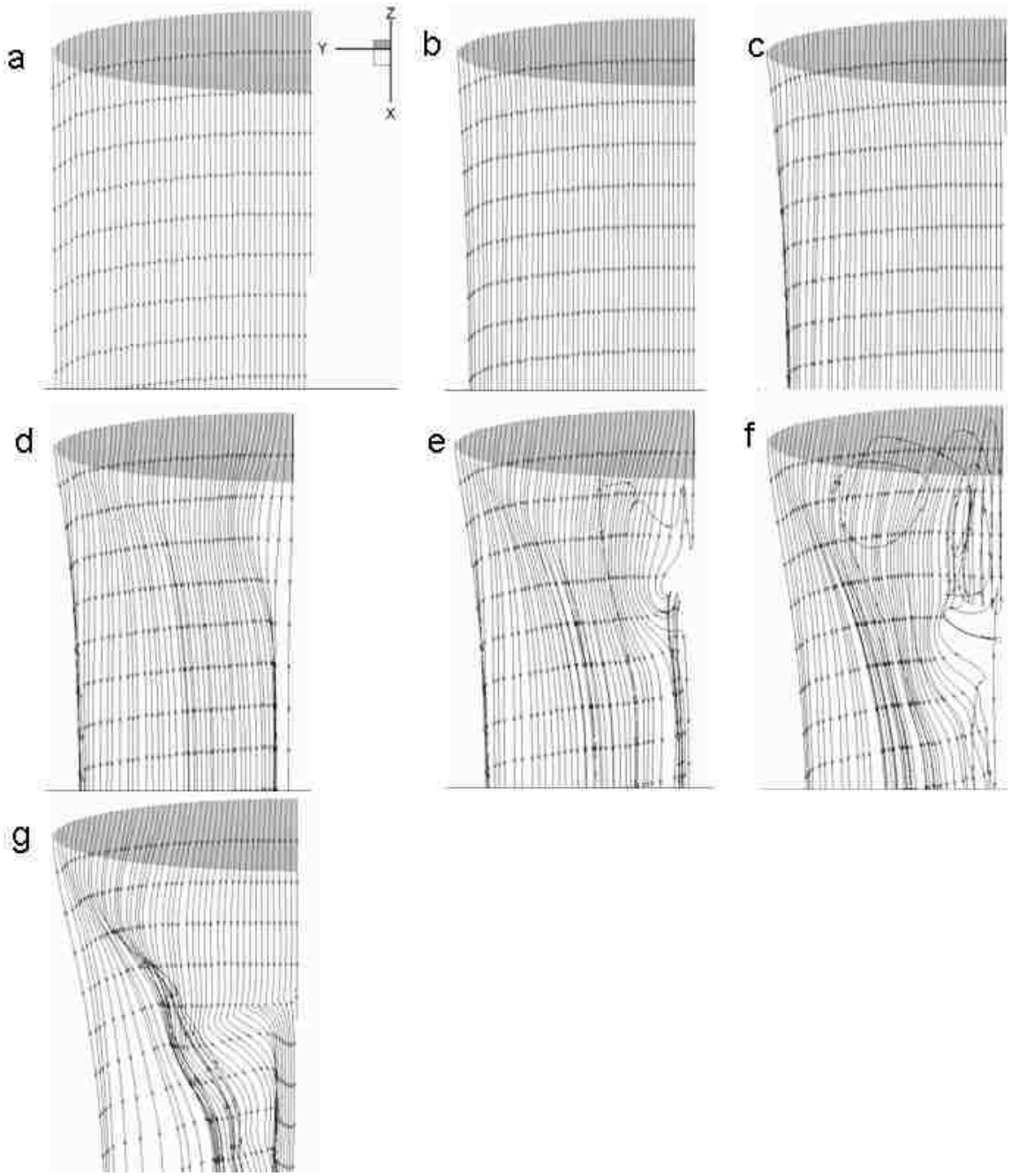

Figure 4-16: Streamlines for cambered semi-ellipse wing. Viewing is direction same as in Figure 4-13. Axis is for orientation purposes. Flow is from top to bottom, tip is left and root is right. Beginning at top left, $\alpha = 0^o$, 10^o, 20^o, 30^o, 35^o, 40^o, and 45^o.

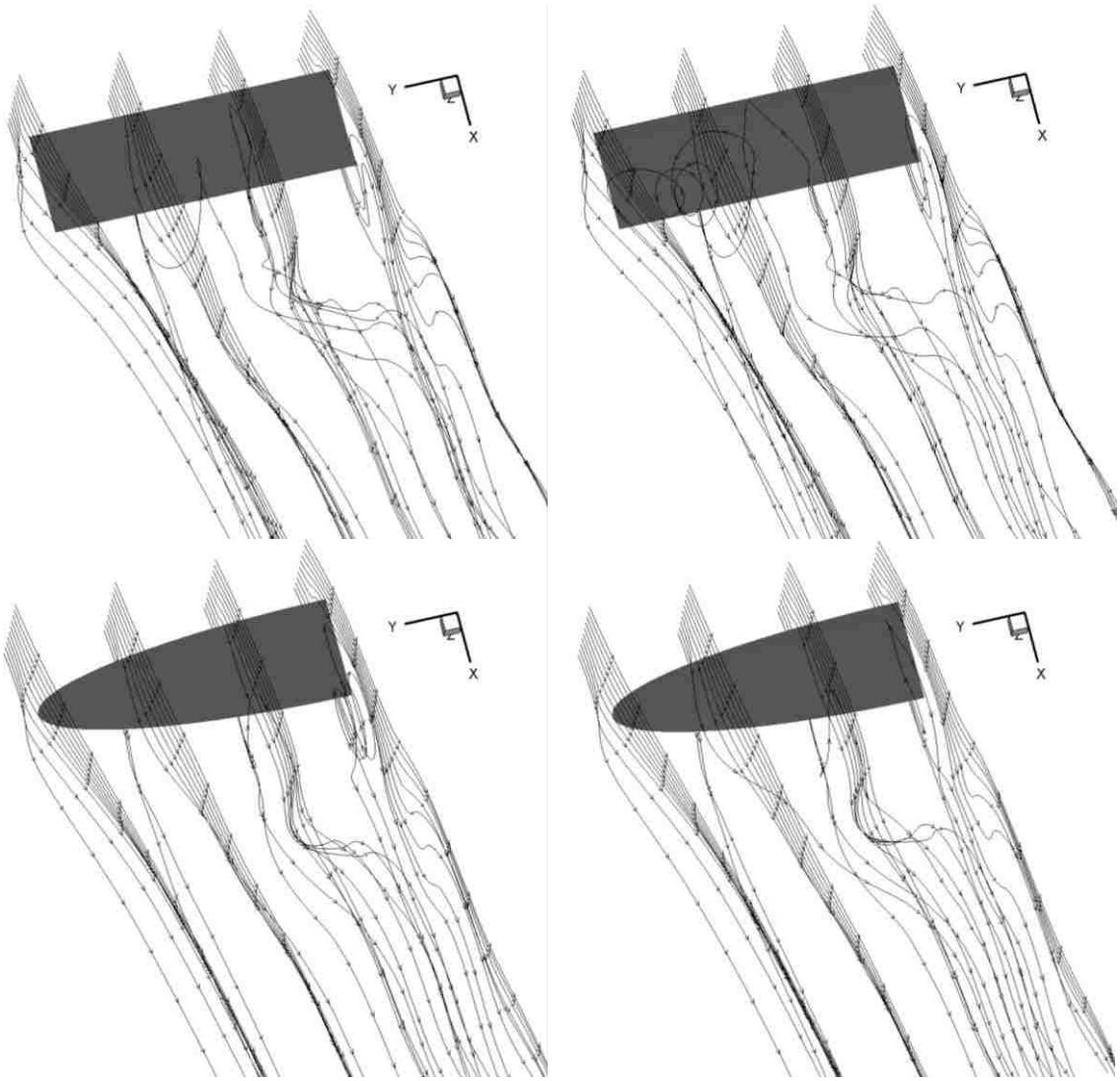

Figure 4-17: Non-cambered rectangular wing, cambered rectangle, non-cambered semi-ellipse, and cambered semi-ellipse, $\alpha = 45^{o}$.

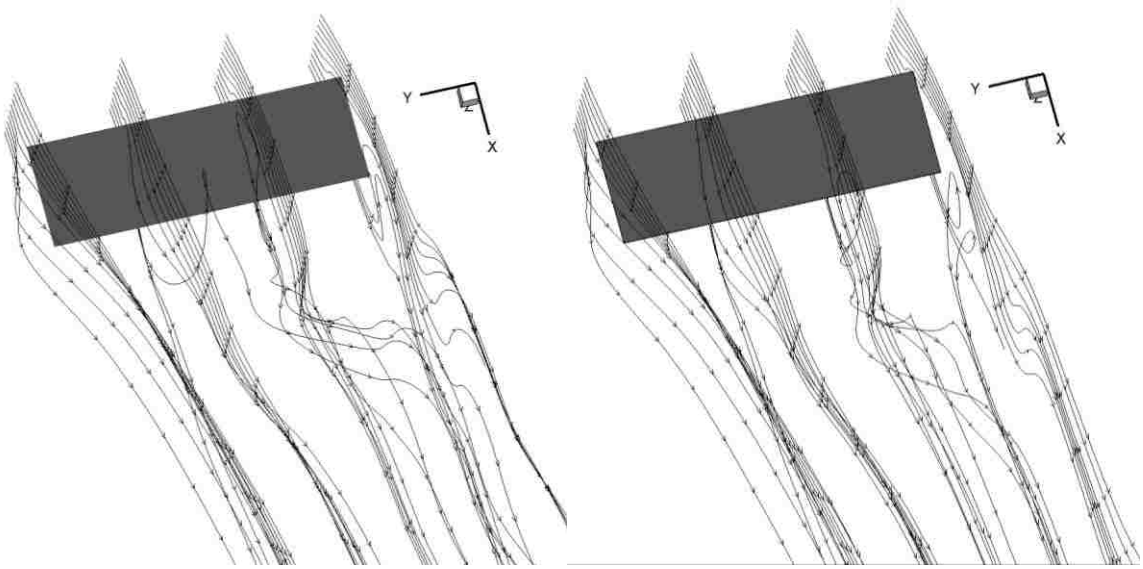

Figure 4-18: Streamlines at Rec = 500 (left) and 5,000 (right.)

4.1.4. Surface Streamtraces. Surface streamtraces were prepared for both the suction and pressure surfaces of all four wings at all seven angles of attack. However, pressure surface streamtraces are not shown here. They are quite similar for all four wings and only reveal a single flow feature. Streamtraces curve toward the tip, thus indicating that the tip vortex becomes increasingly powerful as angle of attack increases. It is possible to correlate features visible in these surface streamtraces, Figure 4-19 through Figure 4-22, to flow features visible in the previous streamline plots, Figure 4-13 through Figure 4-16. Surface streamtraces are often more complicated than near wake streamtraces, especially when separation occurs.

Figure 4-19 through Figure 4-22 show suction surface streamtraces for the noncambered rectangular wing, cambered rectangular wing, noncambered semi-ellipse wing, and cambered semi-ellipse wing, respectively. In all four figures, streamtraces are parallel at $\alpha = 0^o$, but show a curve near the tip at $\alpha = 10^o$. This streamtrace deflection near the tip is more pronounced for the rectangular wings, indicating that the tip vortices are stronger on rectangular wings. This trend is also shown in the streamline plots of Figure 4-13 through Figure 4-16. At and above $\alpha = 20^o$, the surface streamtrace patterns become more interesting. A small series of circular lines indicating a small recirculation region is apparent at 20^o near the root at the trailing edge for the semi-ellipse wings,

Figure 4-21c and Figure 4-22c. This is an earlier indication of the root vortex that develops on the semi-ellipse wings at higher angles of attack, as in Figure 4-15e and Figure 4-16e. The rectangular wings also show a similar swirling pattern possibly indicative of vortices in the rootward half of the suction surface.

A noticeable change is present in the surface stream trace topology between 20^o and 30^o. The patterns are more complex at 20^o than at 30^o, possibly because 20^o is a biurcation value separating the low angle of attack solution and the high angle of attack vortex dominated solution. Figure 4-13c, at 20^o, shows streamline curvature near the root and tip, and its corresponding surface streamtraces in Figure 4-19c show a very complex vortex structure. This trend is echoed in Figure 4-15c and Figure 4-21c for non-cambered semi-ellipse wings at $\alpha = 20^o$. However, the streamtraces have fewer features for the cambered wing at 20^o, because camber promotes attachment.

Lines of flow separation at the leading edge are apparent in all four wings at 30^o, but reattachment is different for the two planform shapes. Reattachment occurs at 35^o in the rectangular wings, as in Figure 4-19e and Figure 4-20e. However, in the semi-ellipse wings of Figure 4-21g and Figure 4-22g, reattachment does not occur until 45^o. Also apparent in all of the figures at 30^o is a circular feature near the tip. This is an unstable focus in the terminology of critical point theory, and represents a vortex near the tip. Another critical point, a saddle point, exists near the trailing edge of the rectangular wings at spanwise locations ranging between one quarter and two fifths span from the root in all four wings at and above $\alpha = 35^o$. This is particularly clear in Figure 4-19f, where surface streamtraces can be seen to converge to it. Streamtraces right of the point of convergence veer to the right and the streamtraces left of it veer to the left. Saddle points suggest spanwise variation of flow features. A saddle point also exists for the semi-ellipse wings in the same region, but the topology is different. Instead of streamtraces converging, surface streamtraces seem to originate from a point near the root at the trailing edge and spread out over a substantial portion of the wing's surface for the 30^o through 40^o cases. This is best shown in Figure 4-22e, and is most likely attributable to the vortex that grows from the root on the semi-ellipse wings. This rootward region is clearly separated from the region closer to the tip where the streamlines are more nearly parallel.

Vortex pairing is evident by comparing the wake vortices in Figure 4-13 through Figure 4-16 to the surface streamtraces in Figure 4-19 through Figure 4-22. These streamline figures do not show vortices shedding as in the two-dimensional cases where vortex shedding causes unsteady lift generation. These vortices instead remain bound to the surface. Their structure is complex and depends on the angle of attack. A wake vortex with a highly complex structure is visible, rather than the coalescence into a well defined tip vortex. The wake vortices axis is curved, and it breaks down fast.

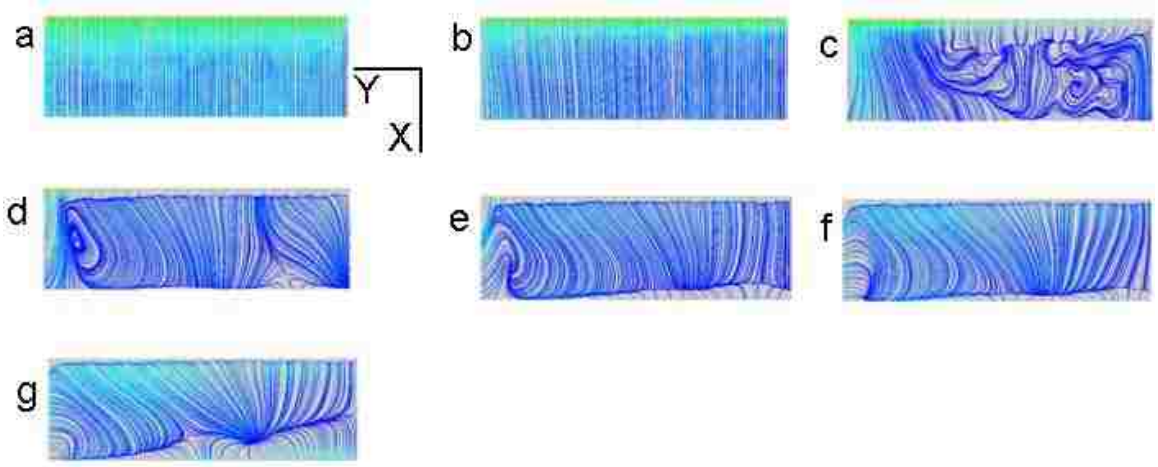

Figure 4-19: Suction surface streamtraces for non-cambered rectangular wing. Flow is from top to bottom, tip is left and root is right. Beginning at top left, $\alpha = 0^o$, 10^o, 20^o, 30^o, 35^o, 40^o, and 45^o. Colors indicate shear stress.

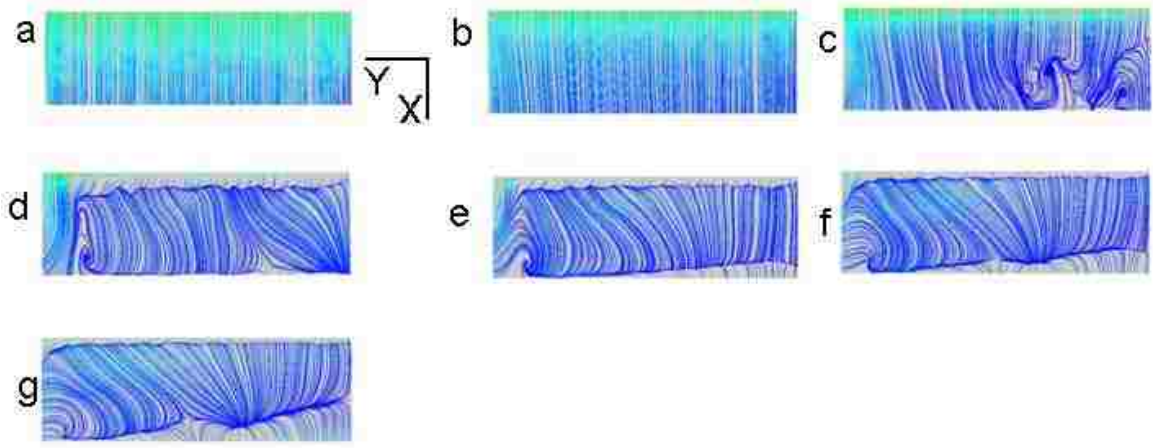

Figure 4-20: Suction surface streamtraces for cambered rectangular wing. Flow is from top to bottom, tip is left and root is right. Beginning at top left, $\alpha = 0^o$, 10^o, 20^o, 30^o, 35^o, 40^o, and 45^o. Colors indicate shear stress.

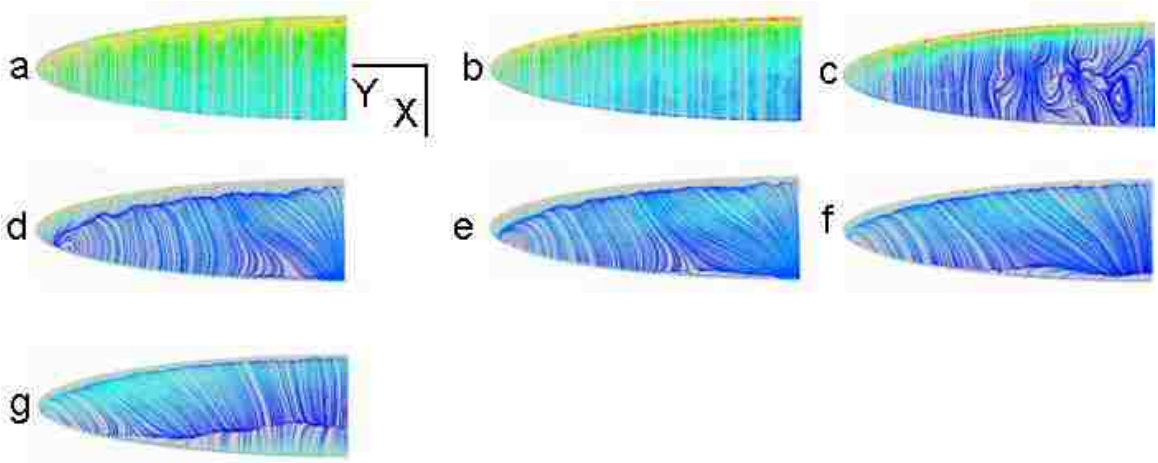

Figure 4-21: Suction surface streamtraces for non-cambered semi-ellipse wing. Flow is from top to bottom, tip is left and root is right. Beginning at top left, $\alpha = 0^o$, 10^o, 20^o, 30^o, 35^o, 40^o, and 45^o. Colors indicate shear stress.

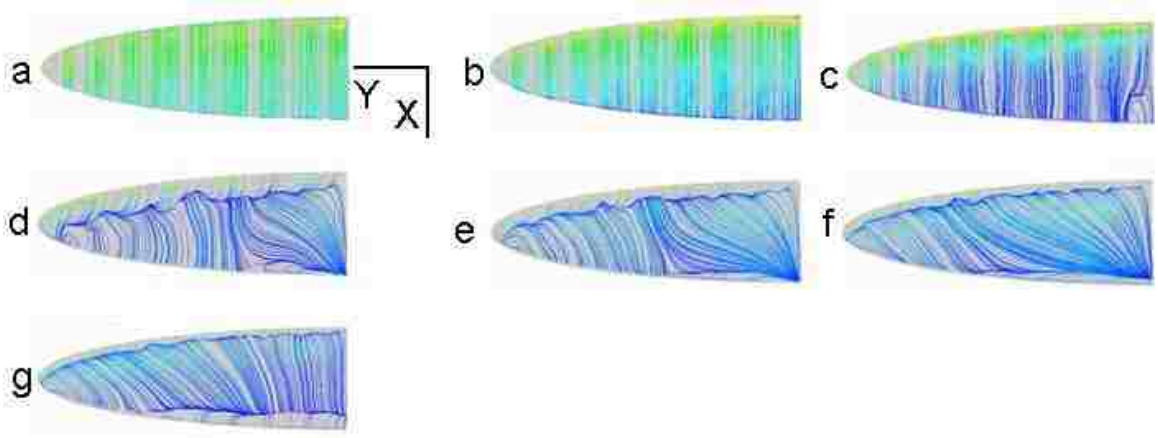

Figure 4-22: Suction surface streamtraces for cambered semi-ellipse wing. Flow is from top to bottom, tip is left and root is right. Beginning at top left, $\alpha = 0^o$, 10^o, 20^o, 30^o, 35^o, 40^o, and 45^o. Colors indicate shear stress.

Surface streamlines can be analyzed using critical point theory to extract flow features ([153], [115], [177].) One case has been selected for this analysis, the surface streamtraces for the non-cambered, rectangular wing, $\alpha = 35^o$ in Figure 4-19e. Important streamtraces are traced in Figure 4-23. Two bifurcation lines are present: one near the leading edge where flow separates, and one near the trailing edge where flow reattaches. These are labeled BL^- and BL^+, respectively. A saddle point, represented by the letter S, is present on the reattachment bifurcation line BL^+. The unstable focus point from which streamlines spiral outward, mentioned previously, can be seen near the wing tip. A similar procedure of sketching streamtraces and determining critical points can be performed for the other surface streamtraces shown in Figure 4-19 through Figure 4-22, as was done in Figure 4-23. However, many of these other cases, especially those in Figure 4-19c and Figure 4-21c, for the non-cambered wings at $\alpha = 20^o$, are quite complicated. This angle of attack is a transition of the flow after which the leading edge vortex begins to form. Surface streamtraces are not as complex for the two cambered wings because camber has already been shows to promote attachment. This can now be extended to indicate that camber causes a smoother transition to vortex-dominated flow.

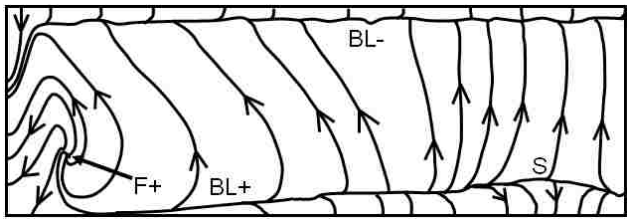

Figure 4-23: Topological features of the surface flow extracted from the streamtraces in Figure 4-19e. Axes and wing orientation are as in that figure.

Several general observations regarding the results can be made: at $\alpha = 20^o$, there is no strong vortex on the leeward surface. The surface streamline pattern shows some waviness probably due to the growing spanwise instability, which indicates a transition to vortex dominated flow. This transition is also manifested in the drag polars (Figure 4-7) which show a C_L maximum at $\alpha \approx 20^o$. At $\alpha = 35^o$ the flow pattern on the suction surface has become more complex. A wake vortex is present on this surface, and the streamlines in this vortex are tightly packed. The vortex seems to break down somewhere between the tip and the root, with the breakdown occurring closer to the tip at higher angles of attack. There is a slight spiraling of the vortex visible in the surface streamtraces toward the wing tip, and the streamlines originating from this vortex merge with the tip vortex evolving into the wake vortex present in Figure 4-13 through Figure 4-16.

4.2. FLAPPING AND PLUNGING EXPERIMENTS

This section consists of two subsections, the first on flapping wing PIV and the second on plunging wing PIV and hydrogen bubble flow visualization. Most of this material is as presented in reference [143].

4.2.1. Flapping PIV. The flapping motion's base case uses the 50mm chord semi-ellipse wing at $\alpha = 25^o$, and the higher of the two available reduced frequencies. To determine the effect of reduced frequency, a set of images was acquired at a lower reduced frequency for the same wing and same α. Then, a rectangular wing of the same size was investigated under the same conditions as the base case. Finally, an angle of attack experiment was performed. In it, several angles of attack were investigated under

the same conditions as the base case. All of the flapping results presented here are for delayed flip. Table 4-4 shows the parameters for the flapping experiment.

Table 4-4: Flapping Experimental Parameters.

	Middle Pivot		Lowest Pivot	
	50mm chord	75mm chord	50mm chord	75mm chord
$U_{average}$, m/s	0.16	0.16	0.11	0.11
Re	8,000	12,000	5,700	8,600
k	0.091	0.14	0.13	0.19
ψ, deg	61.8	61.8	46	46

As mentioned in Section 3.3, the flapping wing moves with respect to the PIV system's imaging plane. This illustrates a problem inherent in all flapping wing PIV systems. As the wing rotates, a different spanwise location is viewed at the imaging plane. Thus, images at two different times in the flapping period will be at two different spanwise locations. For non-rectangular wings, this means the chord length at that location will also be different. The wing can even rotate completely out of the imaging plane. Plunging solves these problems by keeping the same spanwise location of the wing exposed to the imaging plane at all times. The wing will never rotate out of the imaging plane.

Figure 4-24 shows instantaneous velocity vectors for the base flapping case, namely the 50mm chord semi-ellipse wing, at $\alpha = 25^o$, and reduced frequency k = 0.13. These four images, parts A through D, were taken at one quarter period, one half period, three quarters period, and the full period, respectively. Thus, this figure shows a complete flapping cycle. In the top left image in the figure, part A, the wing's motion is rightward; at the top right, part B, the wing is momentarily stationary as it begins its counterclockwise flip and return to the left. In the bottom left, part C, the wing has flipped and is moving left, and in the bottom right, part D, the wing is momentarily stationary as it begins its flip and return to the right. The wing appears as a small

rectangle in part D because it has rotated almost out of the imaging plane. This basic sequence holds for the images in Figure 4-25 and Figure 4-26. Part A shows a clockwise vortex on the suction surface, just aft of the leading edge, and a counterclockwise vortex shed into the wake from the trailing edge. A wake is created by the wing dragging fluid in its direction of motion. The clockwise vortex has shed from the leading edge by part B, and the counterclockwise vortex aft of the trailing edge has dissipated. The entrained fluid continues its rightward motion, where the reversing wing will impact it. Part C shows a development similar to that in part A, with vortices on the leading and trailing edges in senses corresponding to those of part A. The counterclockwise leading edge vortex is the same sense as the counterclockwise flip experienced at the right extreme of the motion, and would be reinforced by it. Also apparent in part C is fluid being pushed in front of the wing, an effect hidden in part A by the shadow region. In part D, two vortices are visible and are nearly touching. The upper of the two vortices is the counterclockwise vortex shed from the leading edge, and the lower is the clockwise vortex shed from the trailing edge. These vortices form between them a jet of fluid in the wing's direction. The clockwise vortex would be reinforced by the clockwise flip experienced at the left extreme of the motion.

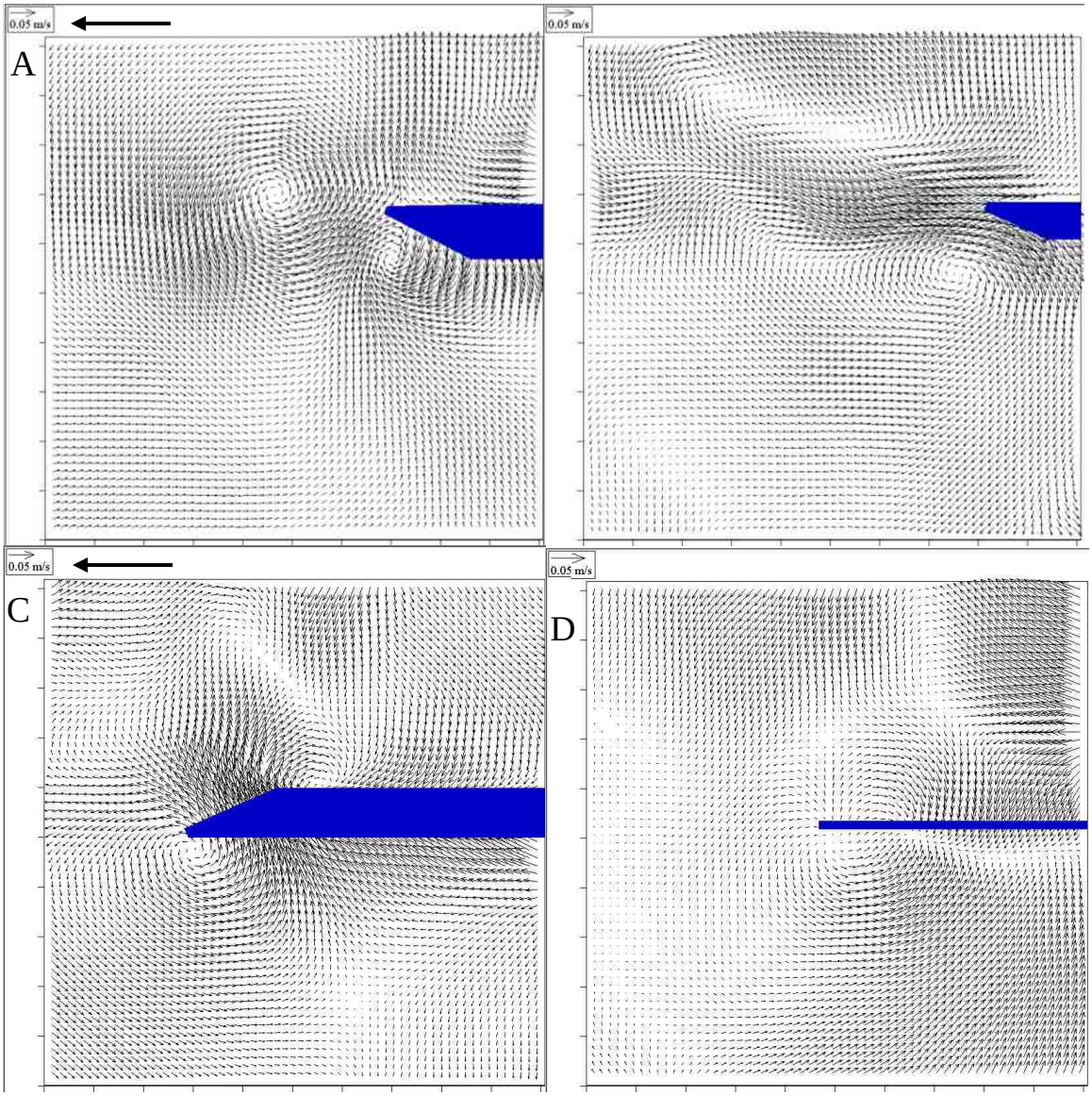

Figure 4-24: Flapping, base case. t=0.25T, 0.5T, 0.75T, and T.

The next set of images, Figure 4-25, is for the same wing at the same angle of attack, but at the lower reduced frequency of 0.091. The reduced frequency was lowered by selecting the middle pivot in the flapping mechanism. The timing and motion are the same as in Figure 4-24, and many of the trends are the same. Fluid circulating around the leading edge forms a clockwise vortex. However, this figure lacks the counterclockwise vortex visible in the previous figure. In part B of Figure 4-25, the leading edge vortex shed sooner at the lower reduced frequency and is farther from the wing than it is in

Figure 4-24. The wake is also larger at the lower reduced frequency. Part C reveals the formation of a leading edge vortex but not a trailing edge vortex as in Figure 4-24. In part D, the leading edge vortex has shed, and the trailing edge vortex has formed by this time.

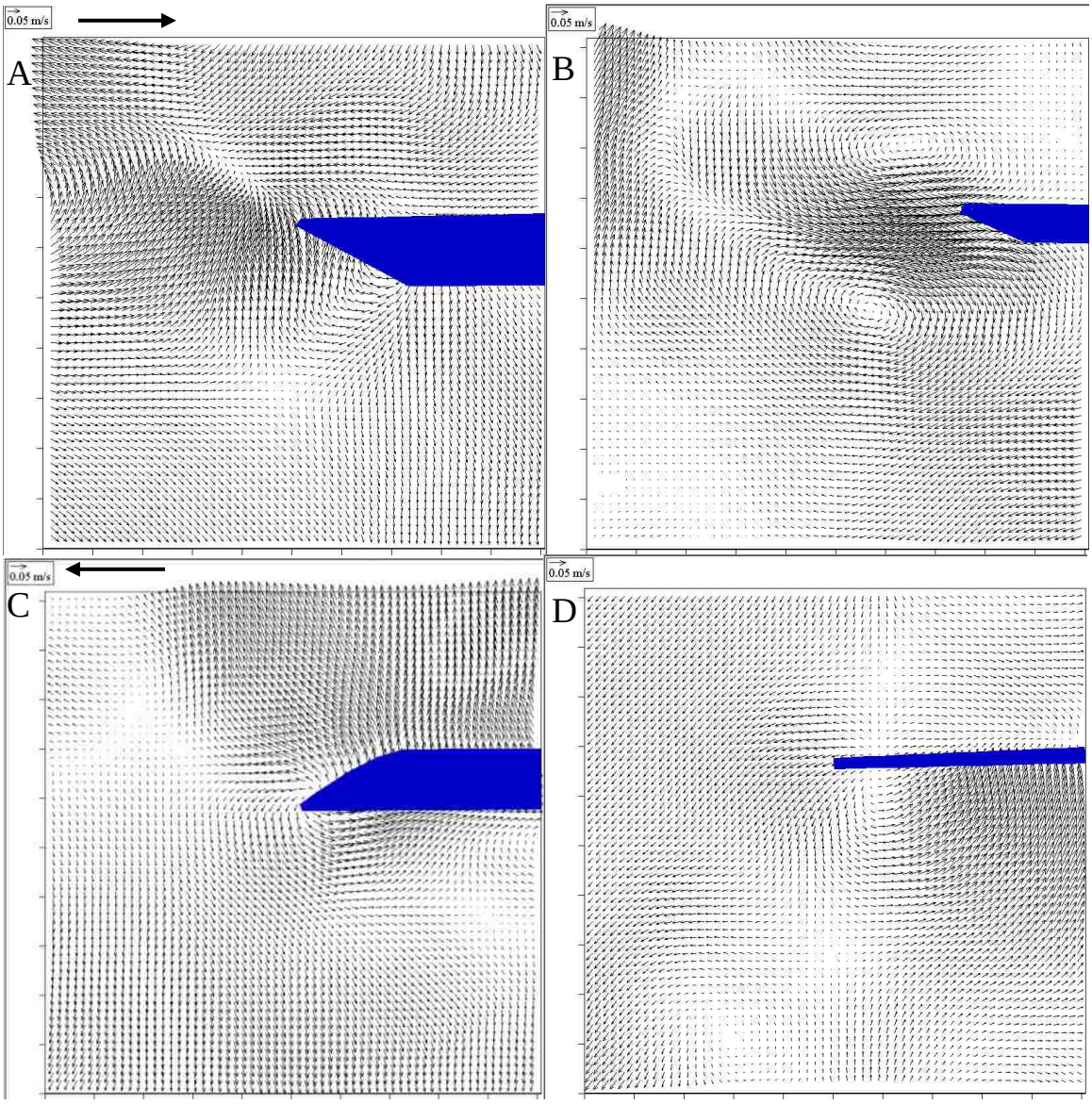

Figure 4-25: Flapping, lower reduced frequency. t=0.25T, 0.5T, 0.75T, and T.

Determination of the effect of wing shape is possible by comparing the next set of images, Figure 4-26, to the base case, Figure 4-24. This set of images uses a rectangular wing with 50mm chord at a reduced frequency of 0.13 and the same angle of attack $\alpha = 25^{o}$. The same clockwise leading edge vortex and counterclockwise vortex shed from the trailing edge apparent in the previous images is visible on the rectangular wing as well, but both vortices appear farther aft of the wing than in Figure 4-24. This indicates earlier vortex detachment on the rectangular wing. Part B, at the right extreme of the motion and at the beginning of the counterclockwise flip, reveals a wake flow directed up and right and which will be impacted by the wing. Wake capture increases the wing's effective angle of attack, and is a beneficial effect. However, there appear to be no qualitative differences between this image and the corresponding image from Figure 4-24. Part C also shows no qualitative differences from its semi-ellipse wing counterpart, with their flow deflected by the pressure surface and their leading edge vortices. Part D was taken just after the clockwise flip at the left extreme of the motion. The clockwise flip experienced at that extreme of the motion reinforces the clockwise vortex shed from what is now the leading edge. Behind the wing is a substantial wake of velocity vectors directed towards the top of the image. Again, this is qualitatively similar to the semi-ellipse wing.

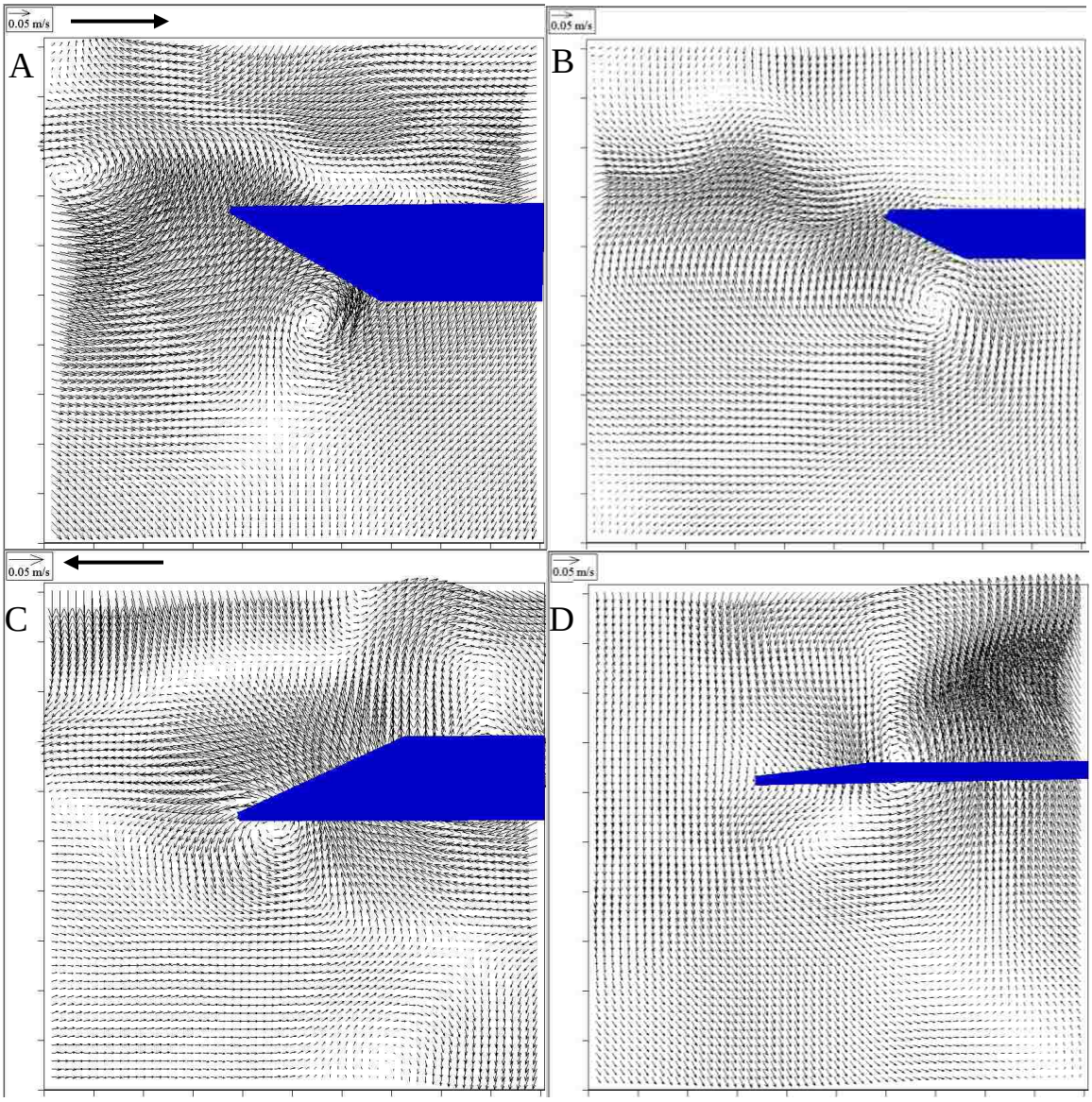

Figure 4-26: Flapping, 50mm chord rectangular wing. t=0.25T, 0.5T, 0.75T, and T.

Angle of attack has a profound effect, as revealed in Figure 4-27, which is for the 50mm chord semi-ellipse wing at a reduced frequency of 0.13, and three angles of attack. The left column shows images at one quarter period, and the right column shows images just after one half period. This allows for the flip to have begun and the wing to have reversed direction. The three rows in the figure are for the angle of attack values, α = 20^o, 30^o, and 40^o, from top to bottom.

Wake size increases with angle of attack, and vortex shedding occurs earlier, as is evident in Figure 4-27. At 20^o, in part A, the trailing edge vortex has been shed while the leading edge vortex remains attached at one quarter period. The same is true at 30^o in part C, but the trailing edge vortex shed earlier and has traveled farther aft. Part E, at 40^o, shows shed leading and trailing edge vortices. The flipping process can be analyzed from parts B, D, and F. Wake captured will occur at all three angles of attack. Also present for all angles of attack is the shed leading edge vortex below the wing in the images, and it will not be captured. Evidence is shown of counterclockwise circulation caused by the counterclockwise flip, especially in part B.

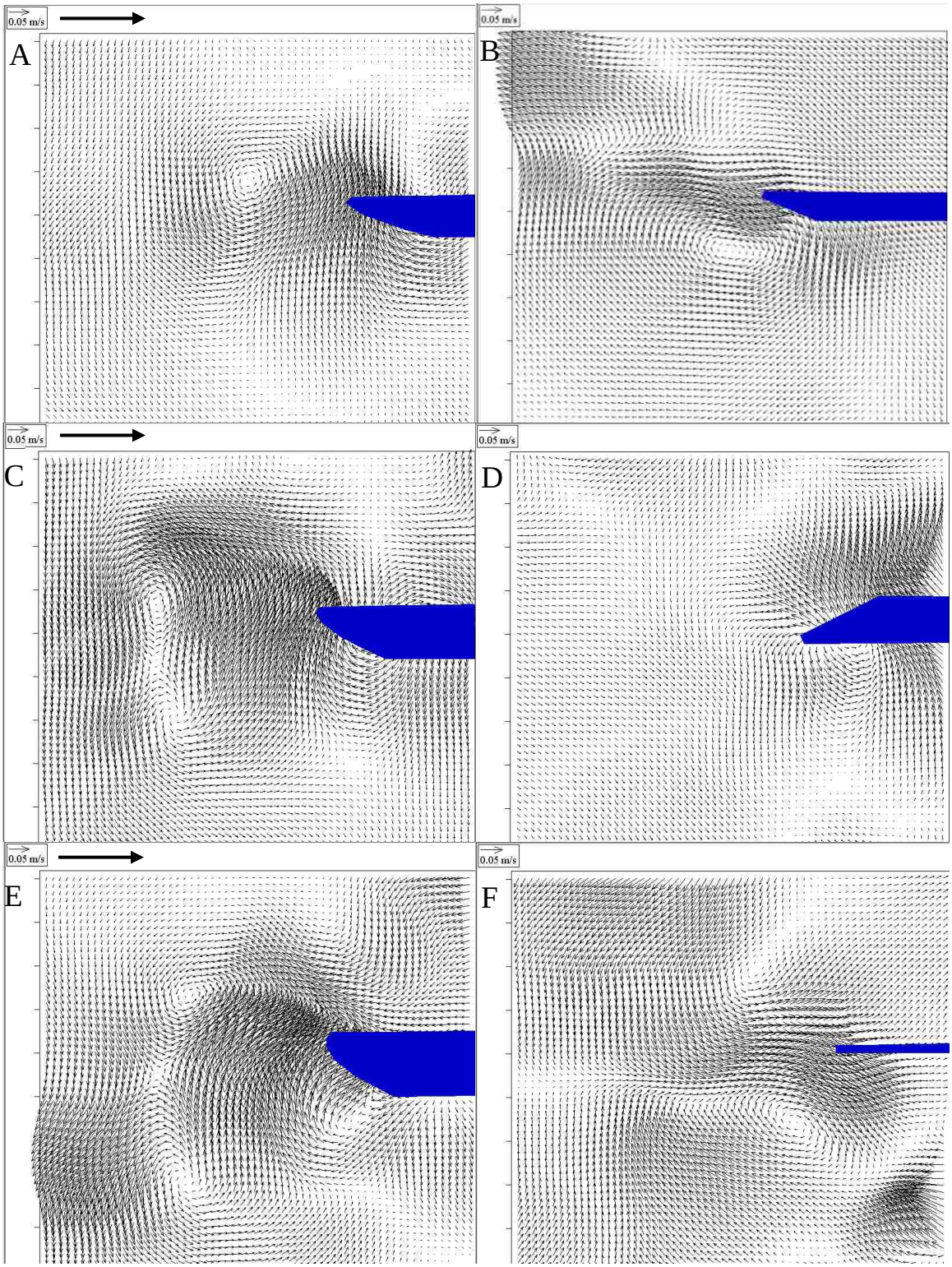

Figure 4-27: Semi-ellipse wing at three angles of attack, 20^o, 30^o, and 40^o, and two locations in its flapping motion: one quarter period, and slightly after one half period.

4.2.2. Plunging Flow Visualization. Hydrogen bubble flow visualization and PIV experiments were performed and are presented in this section. Figure 4-28 shows flow visualization images for the semi-ellipse wing and Figure 4-29 shows flow visualization images for the rectangular wing, both with 50mm chord, 20^o angle of attack, and a reduced frequency of k = 0.31. The four images in each figure were acquired approximately 0.16s before the flip, mid-flip, 0.16s after the flip, and near the midpoint along the downstroke. This flip is at the left extreme of the flapping motion, and is clockwise. Thus, the wing is moving leftward slowly in A, is reversing in B, and is moving rightward in C and D. Leading edge and trailing edge switching also occurs, where the leading edge on the upstroke becomes the trailing edge on the downstroke.

A leading edge vortex is visible in part A of Figure 4-28 and Figure 4-29, as is a series of weak vortices shed from the trailing edge. Both are visible in part B, and the leading edge vortex is being stretched by the flip. Parts B and C also show the formation of a new vortex at the right edge. Part C shows an interesting structure to the former leading edge vortex, which is now at the trailing edge since motion is now rightward. The vortex, which is counterclockwise, has been shed, and is directing a jet of fluid between it and the wing. This is less clear in Figure 4-29 than in Figure 4-28. A new vortex has formed on the new leading edge. Above this vortex is the vortex previously shed from this edge. Part D particularly clearly shows two vortices shedding from the leading edge and two from the trailing edge. Both figures are show similar flow features, indicating no more than a minor effect of planform shape. In previous hydrogen bubble flow visualization images for a flapping wing [61], the development of vortices has been tracked and compares well to the current images. The deformation and shedding of the leading edge vortex and development of a new vortex at the original trailing edge during the flip were reported [61], and are similar to the process here. Tarascio et al [150] also found, in their flow visualization, multiple shed eddies, starting vortices at the extremes of the motion, and a wake. Ramasamy and Leishman [126] also report multiple eddies which shed into the wake.

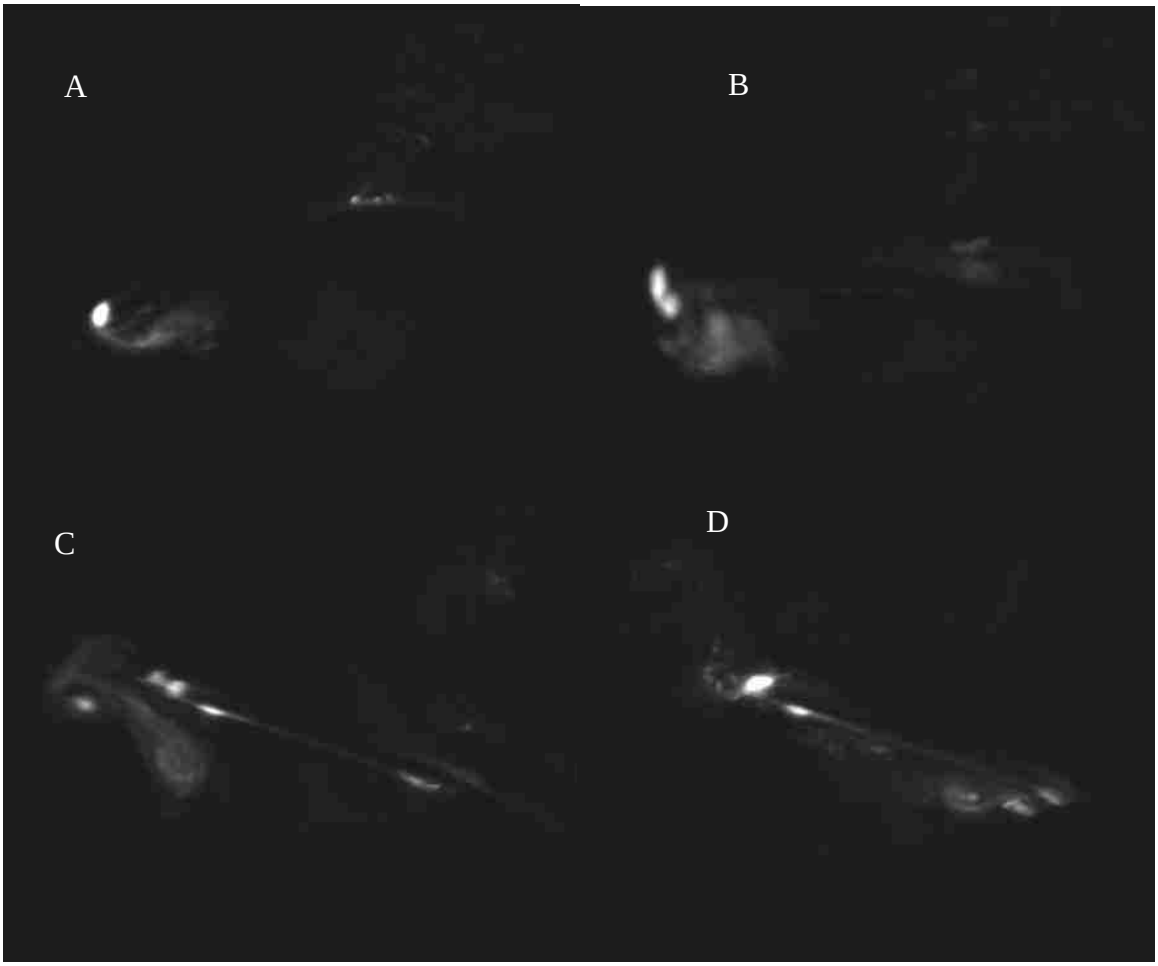

Figure 4-28: Hydrogen bubble flow visualization, semi-ellipse wing.

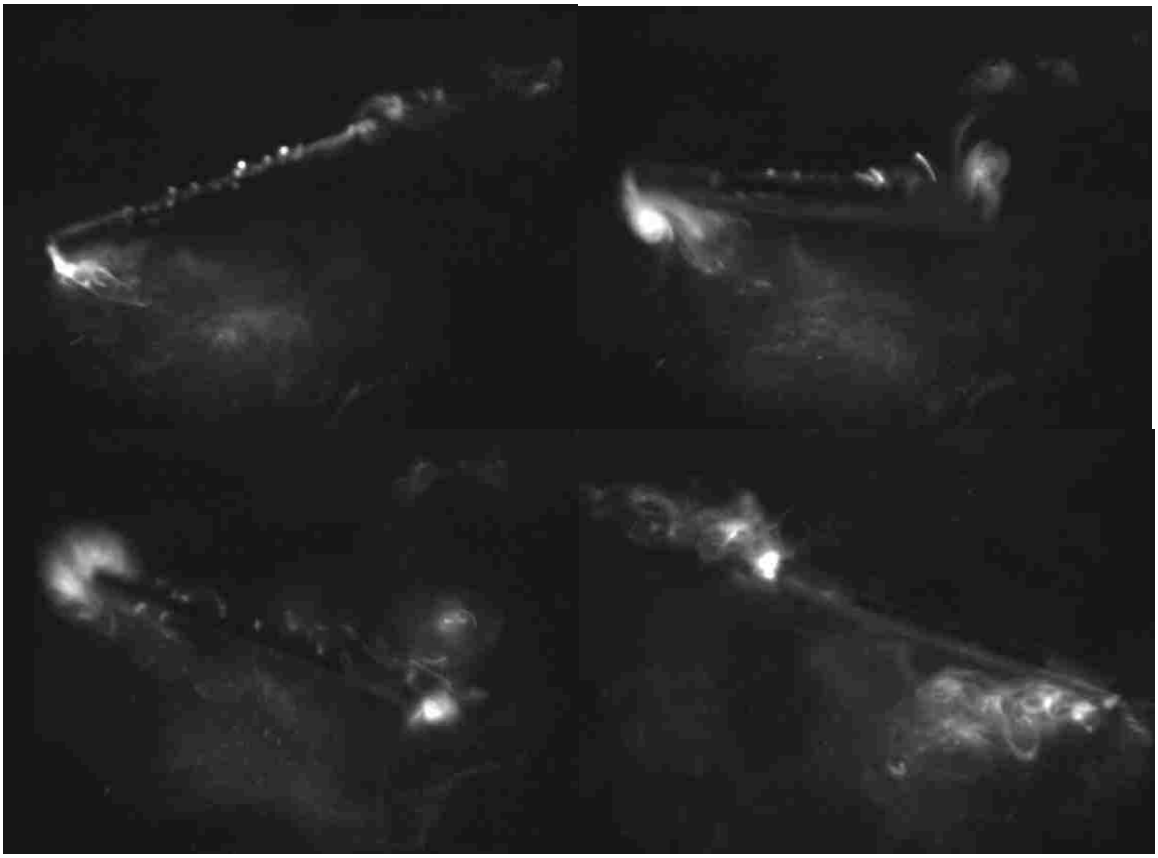

Figure 4-29: Hydrogen bubble flow visualization, rectangular wing.

4.2.3. Plunging PIV. Results from the plunging experiments are presented next. The base plunging case uses the 50mm chord semi-ellipse wing and the highest of the four available reduced frequencies. This was tested at $\alpha = 30^{o}$. The other three lower reduced frequencies were tested for the same wing and same α. Next, the remaining three wings were tested under the same parameters as the base case. Finally, an angle of attack experiment showing two other angles of attack, $\alpha = 20$ and 30^{o}, but with all other parameters the same as the base case, will be presented. All of the plunging results presented here used a symmetric flip. Table 4-5 presents the parameters for the plunging experiments.

Table 4-5: Plunging Experimental Parameters.

	40mm radius		50mm radius		75mm radius		100mm radius	
	50mm chord	75mm chord	50mm chord	75mm chord	50mm chord	75mm chord	50mm chord	75mm chord
$U_{average}$, m/s	0.046	0.046	0.058	0.058	0.087	0.087	0.12	0.12
Re	2,300	3,500	2,900	4,400	4,400	6,500	5,800	8,700
K	0.31	0.47	0.25	0.38	0.17	0.25	0.13	0.19

Figure 4-30 shows the plunging motion base case, which is the 50mm chord semi-ellipse wing at $\alpha = 30^o$ and the highest available reduced frequency for this wing, k = 0.31. Part A shows two vortices, a clockwise vortex attached to the leading edge and a counterclockwise vortex shed from the trailing edge. A wake of velocity vectors directed upward and rightward is also visible in the image. By part B, the shed trailing edge vortex has traveled even farther aft. There is also a substantial wake directed towards the wing will be captured, thus increasing the effective angle of attack. The leading edge vortex has now shed and is below the wing in the image. It is close enough to be captured, but this is not shown in part C. Part C contains the trailing edge vortex shed in Part A, but this vortex will not be captured. A trailing edge vortex is developing, but the development of a leading edge vortex is not apparent. This could be attributable to the shadow region obscuring part of that vortex. Fluid is pushed by the pressure surface, an effect which must exist in part A but is obscured there by the shadow region. During the flip at the left extreme of the motion, part D, a counterclockwise vortex is visible on the trailing edge and which will soon be shed. The clockwise flip at the left extreme of the motion drags fluid along with it, as in Part B, but in the opposite sense. A wake of upward directed velocity vectors is visible in most parts of the figure, and indicates thrust generation in the opposite direction. The flapping case also has this thrust generation.

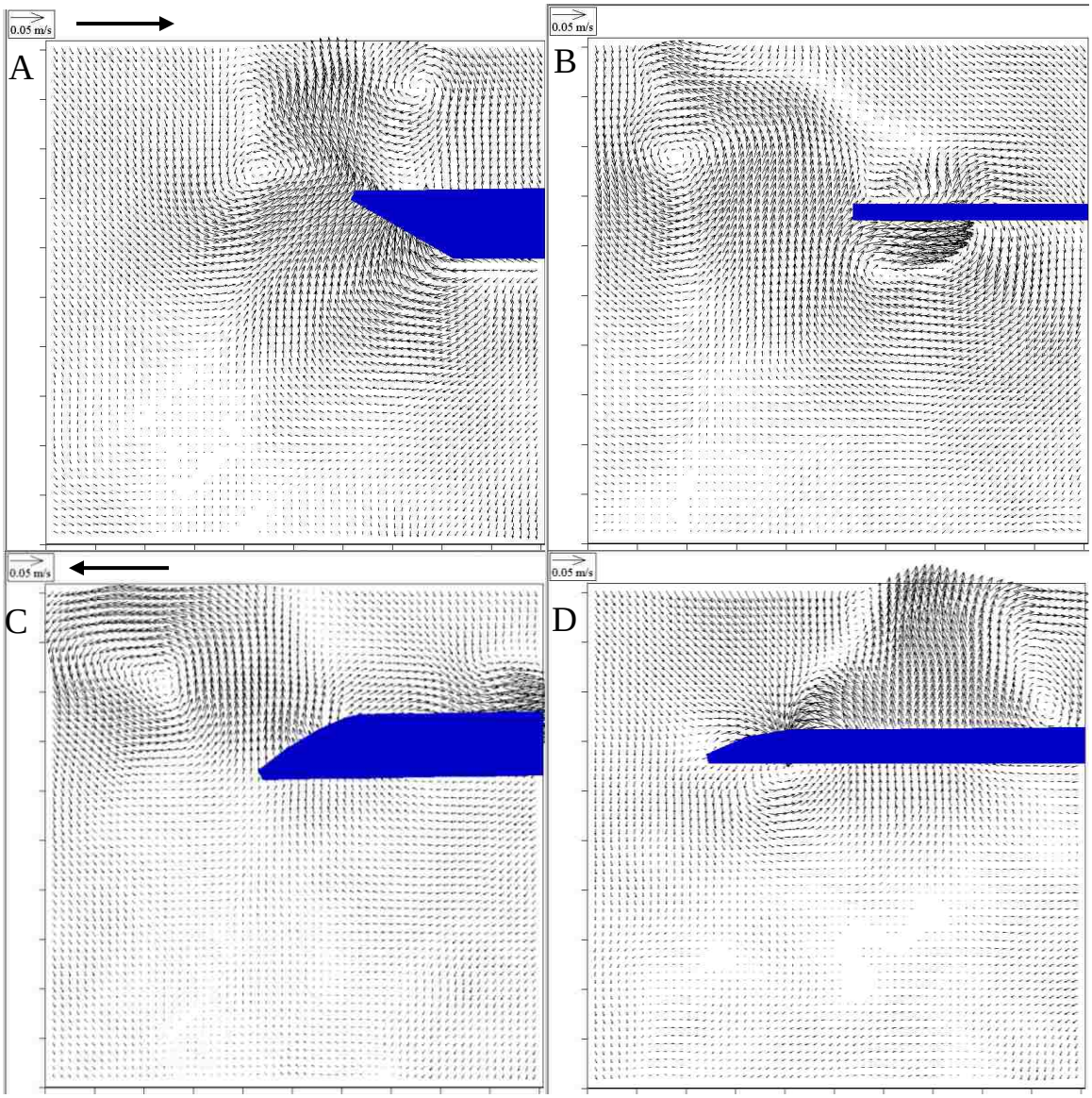

Figure 4-30: Plunging base case. t=0.25T, 0.5T, 0.75T, and T.

The effect of reduced frequency is illustrated in Figure 4-31. This figure shows the 50mm chord semi-ellipse wing at $\alpha = 30^{o}$ and the other three available reduced frequencies for this wing, k = 0.25, 0.17, and 0.13. The images in the left column were taken at one quarter period, and those in the right column were taken at one half period. As reduced frequency decreases, wake size and vortex size increase. Vortex shedding occurs earlier at lower reduced frequencies, as evidenced by the trailing edge vortex

being farther from the wing. Two features occur at all reduced frequencies, wake capture and trailing edge vortex capture. However, the leading edge vortex is shed upon flipping and reversing direction.

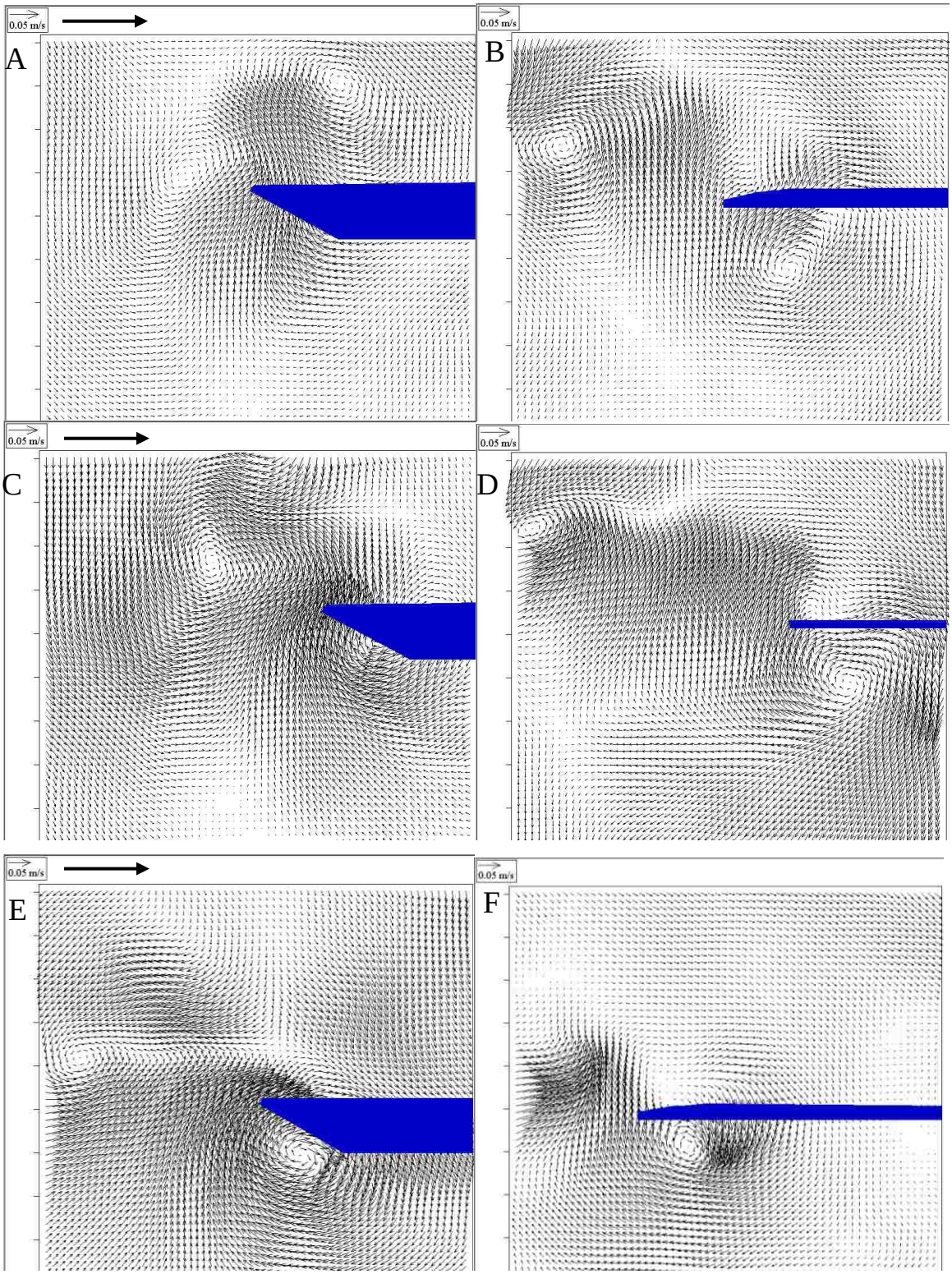

Figure 4-31: Effect of reduced frequency. Left and right columns are at one quarter and one half period, respectively. The three rows are at k = 0.25, 0.17, 0.13.

PIV images for the other three wings are shown in Figure 4-32. These wings are, from top to bottom, the 50mm chord rectangular wing, 75mm chord semi-ellipse wing, and 75mm chord rectangular wing. The angle of attack is $\alpha = 30^{o}$, and the reduced frequency is $k = 0.31$ for the smaller wing and $k = 0.47$ for the larger wings. The rectangular wings are larger near the tip than the semi-ellipse wings. This accounts for the increased flip circulation and larger trailing edge vortex apparent on the rectangular wings. Otherwise, wing shape has no qualitatively substantial affect the flow field.

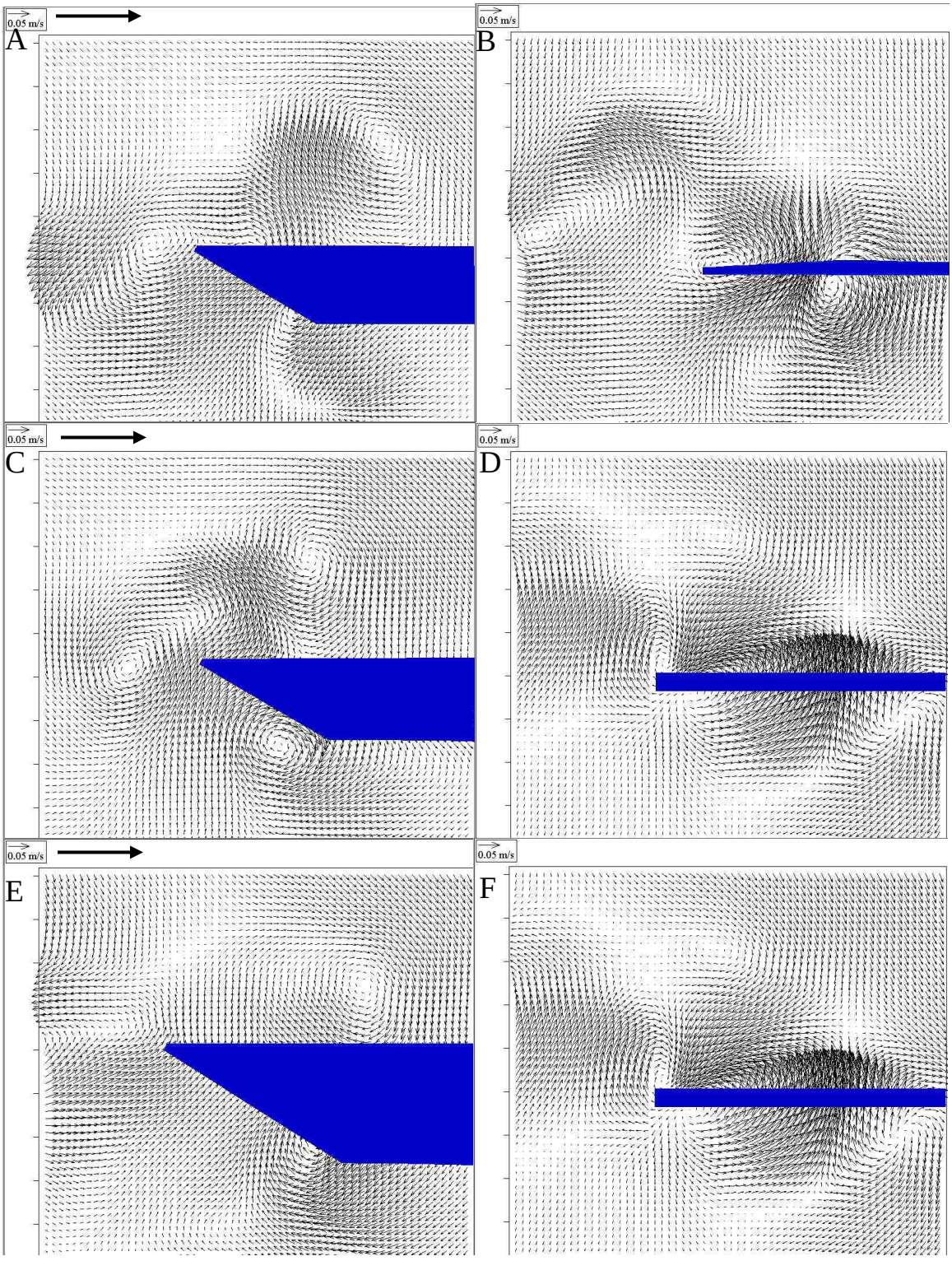

Figure 4-32: Effect of wing shape. Left and right columns are at one quarter and one half period, respectively. The three rows are 50mm chord rectangle, 75mm chord semi-ellipse, and 75mm chord rectangle.

An angle of attack experiment was performed in which two additional angles of attack, $\alpha = 20^o$ and 40^o, were investigated for the base case for the plunging motion. The wing used is the 50mm chord semi-ellipse wing at the highest available reduced frequency for it, k = 0.31. The results of this experiment are shown in Figure 4-33. The wing presents a larger frontal area to the flow at higher angles of attack. This explains the three visible trends. Larger angles of attack produce larger wakes and larger vortices. Also, shedding occurs earlier at higher angles of attack, as evidenced by comparing Parts C and D to Parts A and B.

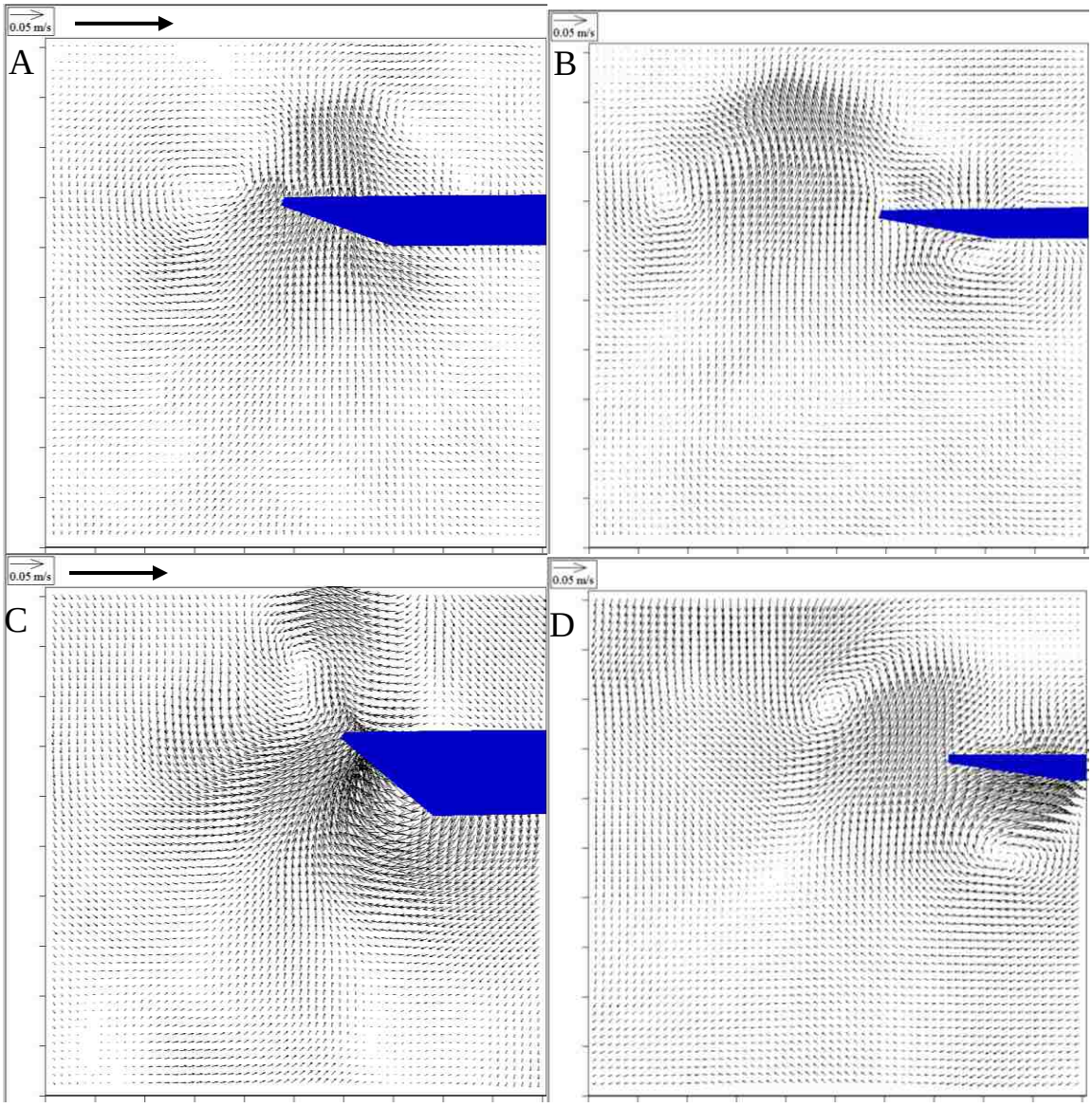

Figure 4-33: Effect of angle of attack. Left and right columns are at one quarter and one half period. The two columns are at angle of $\alpha = 20^{o}$ and 40^{o}.

4.3. PLUNGING WING DYNAMIC MESH CFD

Presented in this section is the investigation of the leading edge trailing edge switching mode, and for comparison other modes, using dynamic mesh CFD. The material for this portion has been published in Reference [146]. Since the primary benefit of the leading edge trailing edge switching mode is that wings can be cambered,

the current study aims to quantify the benefit of camber over a low Reynolds number parameter space.

4.3.1. Computational Procedure And Validation. Four airfoils were investigated, all with chord length of 1cm and 1% thickness. Airfoil 1 is not cambered, and airfoils 2-4 are cambered 1%, 2.5%, and 5%, respectively. Triangular meshes were generated around these airfoils to be as similar to each other as possible. A sample mesh appears in Figure 4-34 for the 0% camber case. Figure 4-35 shows the mesh near the airfoil's edge, again for the 0% camber case. Approximately 40,000 triangular cells were created in all four meshes, and the meshes passed all quality checks with skew less than approximately 0.5. Each mesh consists of two parts, an outer annulus with lower grid density, and an inner circle with higher grid density. The outer boundary is at a radius equal to ten times the chord length, and the radius of the inner circle is twice the chord length. The outer edge is set to outflow boundary condition, and the airfoil is set to wall boundary condition. A grid dependence study was conducted using a mesh with approximately 60,000 cells, and maximum force coefficients were altered by no more than one percent, from which it is concluded that the meshes are sufficient.

The motion of the airfoil was defined by a user defined function. This motion is the leading edge/trailing edge switching hovering mode. The airfoil translates and pitches simultaneously according to equations 17 and 18, respectively, where the period is calculated from equation 21. The Reynolds number determines the maximum velocity the airfoil reaches through equation 19. Plunging frequency f is then calculated from equation 20 for each desired reduced frequency. Period is simply the reciprocal of the frequency, and is given in equation 21. Table 4-6 lists parameters for the cases investigated here. The maximum angle of attack was selected to be 10^o for convenience. Cases 1-12 utilize the leading edge trailing edge switching mode, but Cases 13 and 14 are for different dynamics, and are included for comparison. In Case 13 the airfoil heaves vertically, but with no rotation, in a horizontal freestream. Case 14 is a normal hovering mode, mode 2, where the leading edge and trailing edge do not switch, and the angle of attack varies 10^o from the vertical.

$$\dot{x} = U_{max} \sin(2\pi t/Pd) \tag{17}$$

$$\omega_z = \frac{2\pi\alpha}{Pd}\cos(2\pi t/Pd) \tag{18}$$

$$Re_c = \frac{U_{max}\, c}{\nu} \tag{19}$$

$$k = \frac{f\, c}{U_{max}} \tag{20}$$

$$Pd = \frac{1}{f} = \frac{c}{k\, U_{max}} \tag{21}$$

Table 4-6: Computational Cases and Parameters.

Case #	Parameters	Case #	Parameters
1	Re_c=500, k=1, LE/TE, 0% camber	8	Re_c=500, k=2, LE/TE, 1% camber
2	Re_c=500, k=1, LE/TE, 1% camber	9	Re_c=100, k=1, LE/TE, 0% camber
3	Re_c=500, k=1, LE/TE, 2.5% camber	10	Re_c=100, k=1, LE/TE, 1% camber
4	Re_c=500, k=1, LE/TE, 5% camber	11	Re_c=2,500, k=1, LE/TE, 0% camber
5	Re_c=500, k=0.5, LE/TE, 0% camber	12	Re_c=2,500, k=1, LE/TE, 1% camber
6	Re_c=500, k=0.5, LE/TE, 1% camber	13	Re_c=500, k=1, standard plunging, 0% camber
7	Re_c=500, k=2, LE/TE, 0% camber	14	Re_c=500, k=1, normal hovering, 0% camber

The motion of the airfoil is diagrammed in Figure 4-36. The airfoil begins at the left end of the motion and is oriented horizontally. It then translates rightward at increasing speeds and pitches up, until it reaches both maximum angle of attack and maximum translational velocity at one quarter period. The airfoil then continues to the right, but at decreasing speeds, and pitches down until it is horizontal at the right extreme of the motion, at one half period. The same motion then occurs in reverse, with what was the trailing edge on the upstroke now serving as the leading edge on the return stroke.

The dynamic mesh strategy of spring analogy smoothing built into Fluent v.6.3.26 and described in Reference [44] was employed in this research. It was determined that

1,000 steps per period was sufficient for the dynamic mesh routine to remesh without exceeding a skew of 0.7, an acceptable value for two dimensional meshes. PISO, pressure implicit with splitting of operators, was selected as the solver since it is recommended for unsteady dynamic mesh calculations in the FLUENT user's guide [44]. PISO is a predictor corrector method with one predictor and two corrector steps, in which the discretized equations are solved sequentially and uncoupled. The solutions presented here are laminar. Young et al [182], in a three dimensional dynamic mesh study of a flapping wing with a Reynolds number range of 100 to 50,000, and also Elimelech et al [37], in a two dimensional fixed mesh airfoil study, proved the validity of laminar flow. Shedding occurs at a fixed location on the sharp leading edge, and this is unaffected by turbulence. By monitoring the x and y force coefficients, it was also determined that five periods was found to be sufficient for the flow to reach a periodic state, and that starting effects had dissipated before reaching the fifth period. Examining the velocity vectors away from the airfoil reveals that the velocity was near zero well inside the outer circular boundary with outflow boundary condition.

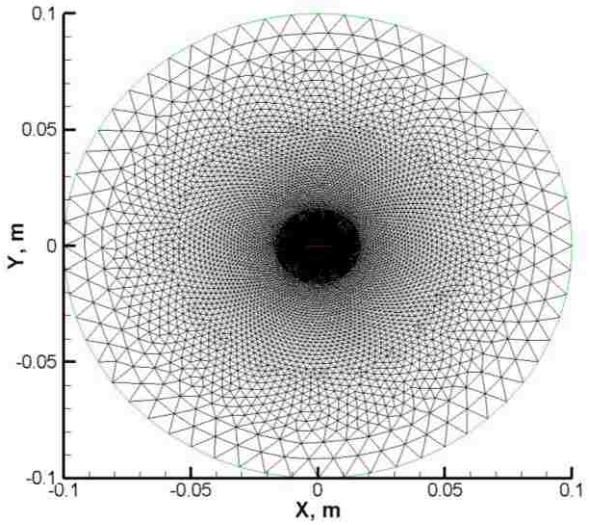

Figure 4-34: Triangular mesh on non-cambered airfoil.

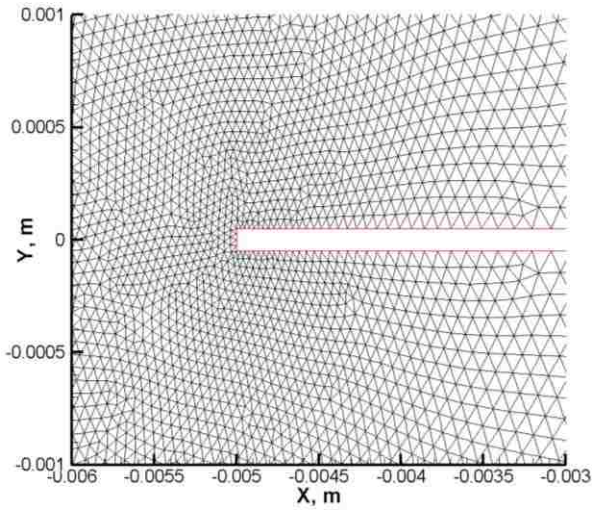

Figure 4-35: Near airfoil mesh.

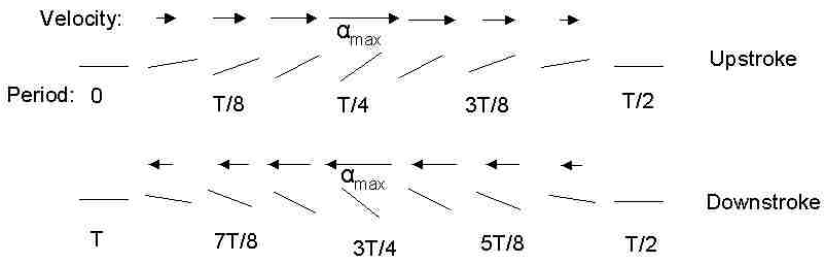

Figure 4-36: Airfoil motion.

Validation has been performed over the entire Reynolds number range, and for both fixed and dynamic mesh. Drag coefficient on a circular cylinder has been computed and compared with the correlation presented in Reference [173] and repeated in equation 22 below. The first of two dynamic mesh validations is for the oscillating circular cylinder at Re_D = 185, with an amplitude of 0.2D, and an excitation frequency f_e=0.154 Hz, presented in Reference [52]. The second dynamic mesh validation is a NACA 0012 airfoil pitching about its quarter chord point at Re_c = 12,000, presented in References [125], [180], and [74]. Two cases were computed here: the first with angle of attack amplitude $\alpha=2^o$ and k=4.275, and the second with $\alpha=4^o$ and k=2.159. It should be noted that those authors define reduced frequency with an additional factor of pi. Comparisons are provided in Table 4-7, and are within the established bounds. For example, Ramamurti and Sandberg [125] have C_T=0.0543 at k=2.159 and $\alpha=4^o$, while Young and Lai [180]

have C_T=0.061 at k=1.91 and α=4°. Also, Ramamurti and Sandberg [125] have C_T=0.0339 at k=4.27 and α=2°, while Young and Lai [180] have C_T=0.070 at k=3.83 and α=2°. Figure 4-37 shows z-vorticity filled contours for this pitching airfoil, where the shed vortices match the flow visualization images in Koochesfahani [74] well.

$$C_D = 1 + 10.0*Re_D^{-2/3} \quad (22)$$

Table 4-7: Validation.

Fixed Mesh				Dynamic Mesh		
Re_D	100	500	2,500	Oscillating Cylinder	Pitching Airfoil	
					k=4.275, α=2°	k=2.159, α=4°
C_D from Reference	1.46	1.16	1.05	1.20	-0.0339	-0.0543
C_D Computed	1.32	1.17	1.00	1.25	-0.0481	-0.0657
% Difference	9.6	0.9	4.8	4.2	42	21

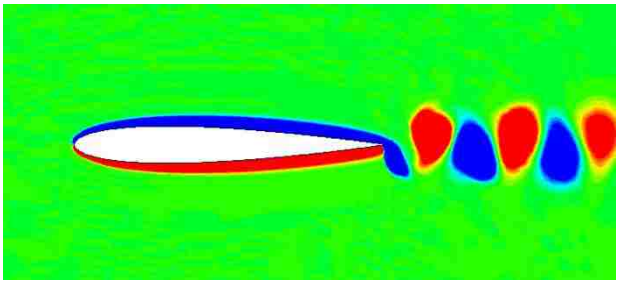

Figure 4-37: Z-vorticity for NACA 0012 airfoil pitching about quarter chord, Re_c=12,000, k=1.91, α=4°.

4.3.2. Results. X and Y force coefficients over one period, and averaged values, are the first set of results presented here. Figure 4-38 presents the force coefficients for Case 1, and Table 4-8 presents force coefficients averaged over one period for every case. The maximum translation velocity, U_{max}, was used as the velocity scale in computing these

coefficients. Lift is in the y direction, and the value of C_Y averaged over this period for Case 1 is 0.152. Thus, net lift is being generated even for a non-cambered airfoil. C_Y forms a near perfect sine curve, while C_X does not show such behavior. Sunada et al [140] also report a roughly sinusoidal force curve. Also, C_Y goes through two cycles in each plunging cycle, while C_X appears to go through one cycle. However, further analysis of the dot product of force and displacement reveals that C_X undergoes two cycles in each period. During the first half of the period, the airfoil travels in the positive x direction. It is notable that the x direction force component is both positive and negative during this portion of the period. Thus, there is both drag, when the force opposes the motion and the dot product is negative, and thrust, when the force is in the direction of motion and the dot product is positive. When the sign of C_X is adjusted to negative for drag and positive for thrust, as in Figure 4-39, a pattern forms for the upstroke and downstroke. Drag is present initially, and increases until approximately 0.16 of a period, and then decreases. Around 0.32 into the period, the force is in the direction of motion and therefore changes from drag to thrust for the remainder of the upstroke. At the point of stroke reversal, one half period, the airfoil begins to travel in the opposite direction. The force magnitude and direction remains constant, but switches from thrust to drag. Net drag is generated in the x direction for all cases but Case 13 where this is not applicable. Camber provides additional lift for every leading edge trailing edge switching case investigated here. Cases 1-4 indicate increasing lift for increasing camber up to 5%.

Lift coefficient reaches its peak before the points of highest velocity and angle of attack, which occur at one quarter and three quarters period. This behavior is attributed to the separation region on the suction surface of the airfoil as the airfoil pitches up, and thus the force vector pitches aft. Tang et al [149] report maximum lift occurring after the point of maximum velocity and angle of attack, beyond which lift decreases due to the recirculation bubble. However, in the present study, negative lift occurs during part of the period. This is explainable by the differences in reduced frequency, Reynolds number, and airfoil section between the two studies. Separation is promoted by the sharp edged plates investigated here, whereas the smooth, elliptical airfoil section of Tang et al [149] would delay separation. Lift coefficient initially increases until 0.15 period, after

which it decreases to zero around 0.30 period, and then reaches a negative value. This negative value peaks around 0.40 period, past which lift coefficient increases back to zero shortly after half a period. This pattern repeats for the return stroke.

Figure 4-41 shows the flow features which govern this force generation pattern. The vorticity distribution above the suction surface changes at the same point in the cycle where the lift coefficient reaches its peak. At this point, the region of CW vorticity moves aft and the suction surface is covered by CCW vorticity. Maximum lift occurs when the airfoil breaks through the tongue of CW vorticity to the right of the airfoil. The CCW vorticity which is now present on the suction surface reduces lift until the lift reaches its most negative value. After reaching this lift minimum, CW vorticity returns to the suction surface and increases lift. For the return stroke, the situation is similar. By the Kutta-Joukowski theorem [70], when the motion of the airfoil is to the right, CW vorticity causes lift; however, when the motion of the airfoil is to the left, CCW vorticity causes lift. It is also noted that stagnation regions on the surface of the airfoil, visible in Figure 4-40, have high pressure and create a force normal to the airfoil.

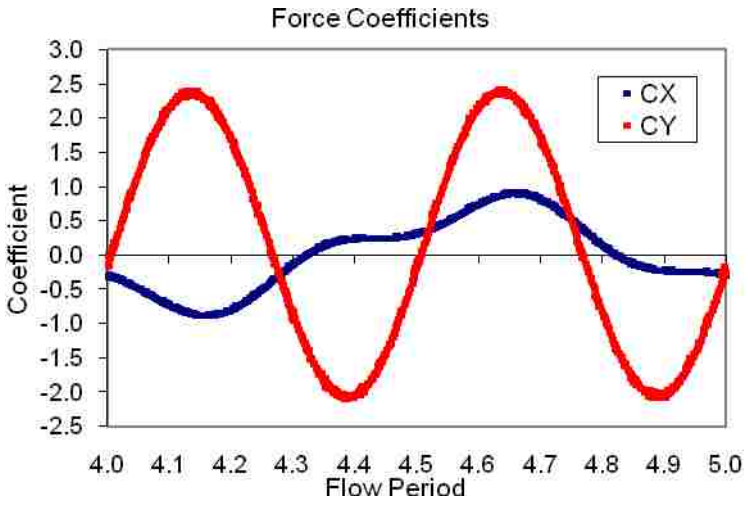

Figure 4-38: Force coefficients for one period, Case 1, 0% camber airfoil.

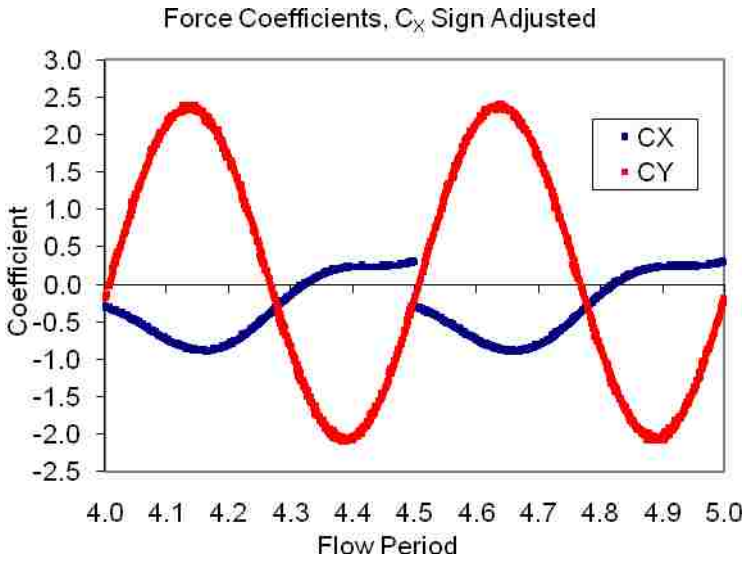

Figure 4-39: Force coefficients for Case 1, with adjusted sign.

Table 4-8: Force coefficient values averaged over one period.

Case #	C_X	C_Y	Case #	C_X	C_Y
1	-0.298	0.152	8	-0.350	0.363
2	-0.279	0.160	9	-0.608	0.146
3	-0.260	0.171	10	-0.589	0.151
4	-0.235	0.191	11	-0.169	0.189
5	-0.211	0.075	12	-0.152	0.198
6	-0.209	0.081	13	-0.258	na
7	-0.425	0.354	14	-5.76	0.742

The next figure shows velocity vectors for the 0% camber airfoil in Case 1. Flow features during the first half of the period mirrored flow features during the second half of the period, so only images from the first half of the period are presented in this figure. Part A of the figure is at the beginning of period four, and the subsequent parts of the figure are evenly spaced at 10% period. The flow features in part F, at 50% period, look symmetric with the flow features in part A. They both exhibit a vortex at both edges; at

the inward facing edge, which is the right edge in part A and the left edge in part F, and at the outer edge. Between the leading and trailing edges on the upper (suction) surface, circulation in the sense of the airfoil's rotation is visible, which is counterclockwise in part A and clockwise in part F. The inward edge vortex, clockwise in sense in part A, is shed from the right edge, which is now the leading edge in part B. The leading edge vortex slips to the pressure surface below the leading edge in part C, and a counterclockwise vortex forms at the leading edge suction surface in part D. This vortex sheds in part F, and is the outer vortex. A region of high velocity at the left edge, which is now the trailing edge, splits into two regions in parts B and C. It forms a counterclockwise vortex in part E, and becomes the inward facing edge vortex at part F, mentioned above. It is also apparent from all parts of this figure that there is a downward directed wake, which causes lift in the upward direction by the momentum theorem. Thus, there are four important flow features: two vortices, one from each of the inner and outer edges, one region of circulation caused by the rotation of the airfoil, and a downward wake. Those two vortices are named as inner and outer to avoid confusion that would be caused by calling them leading or trailing edge vortices, since the leading and trailing edges switch. The region of circulation caused by the rotation of the airfoil causes lift and is also known at the Magnus effect. Freymuth [46] provides flow visualization images showing similarities to the vector plot in Figure 4-40. In those images, a pair of opposite sense vortices is created in each cycle and they are convected away from the airfoil by the jet.

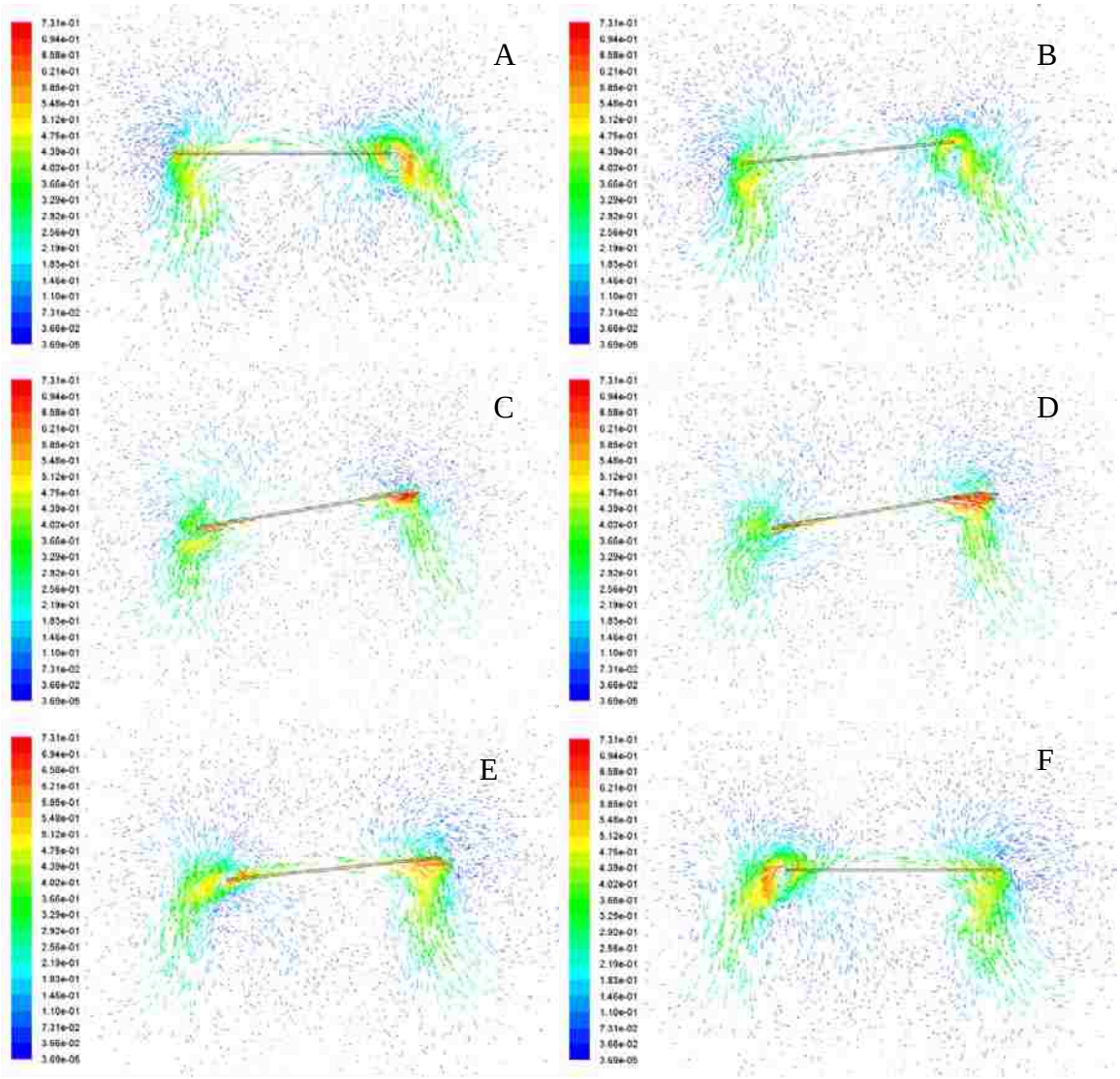

Figure 4-40: Velocity vectors, m/s, Case 1, 0% camber airfoil.

Figure 4-41 shows filled contours of Z vorticity, ζ_Z, for Case 1. In this figure, red regions have counterclockwise rotation where $\zeta_Z>0$, and blue regions have clockwise rotation where $\zeta_Z<0$. In part A, a thick layer of CW vorticity is apparent above a thin layer of CCW vorticity above the airfoil and wrapping around it on both the left and right. A similar arrangement occurs on the lower surface, where a large CCW region is below the airfoil in the center, with small regions of CW vorticity below the airfoil near the edges. The situation is reversed by part F. The region of CW vorticity on top of the

airfoil in part A, and including vortex 1', feeds and merges with the outboard vortex 1. Rightward motion of the airfoil causes vortex 1' to shed. Vortex 1 is then fed by the CW vorticity below the airfoil until it is shed in part F. Vortex 1 is connected to vortex 3 through the regions of CW vorticity above and below the airfoil from part B until shedding in part F. A tongue of CW vorticity is severed by rightward motion of the airfoil, thus separating this region of CW vorticity into two distinct regions, one above and the other below the airfoil, as in part C. Freymuth [46] also reports this vortex severing. Vortex 3 merges with the tongue of CW vorticity from above the airfoil in part B, but the rightward motion severs that connection and vortex 3 becomes connected to the region of CW vorticity below the airfoil and in vortex 1 in part C. By part E, the CW vorticity from above the airfoil is now entirely past the airfoil, and CCW vorticity covers the area above the airfoil, symmetric with the situation in part A. It now forms a tongue which will be severed on the return stroke. Vortex 2 is connected to the region of CCW vorticity below the airfoil in part A, but this connection is broken and vortex 2 is shed by part C. However, CCW vorticity from above the airfoil will connect with this vortex again shortly after the return stroke begins, in a manner symmetric with vortex 3 in parts A and B. Vortex 4, which was shed during the previous stroke, becomes reconnected with the airfoil in part E. In part F, a small vortex 4' on the right edge develops and joins vortex 4, just like vortex 1' joins vortex 1 in part A. It is apparent that parts A and F are symmetric with each other, and that vortices 1, 2, 3, and 4 in part A correspond with vortices 4, 3, 2, and 1, respectively, in part F. Sunada et al [140] also report four vortices. A primary vortex forms at the leading edge during the upstroke, and four vortices are present near stroke reversal. Two vortices are shed, one from each surface of the airfoil, immediately after stroke reversal. The primary vortex at the leading edge then redevelops. The present work is consistent with Sunada et al [140]. Vorticity contour plots reveal flow features for cases 2-4, with 1-5% camber, to be qualitatively similar to those in Figure 4-41. The similarity is so close that an additional figure is not presented. Case 4, with 5% camber, had 26% more lift than case 1.

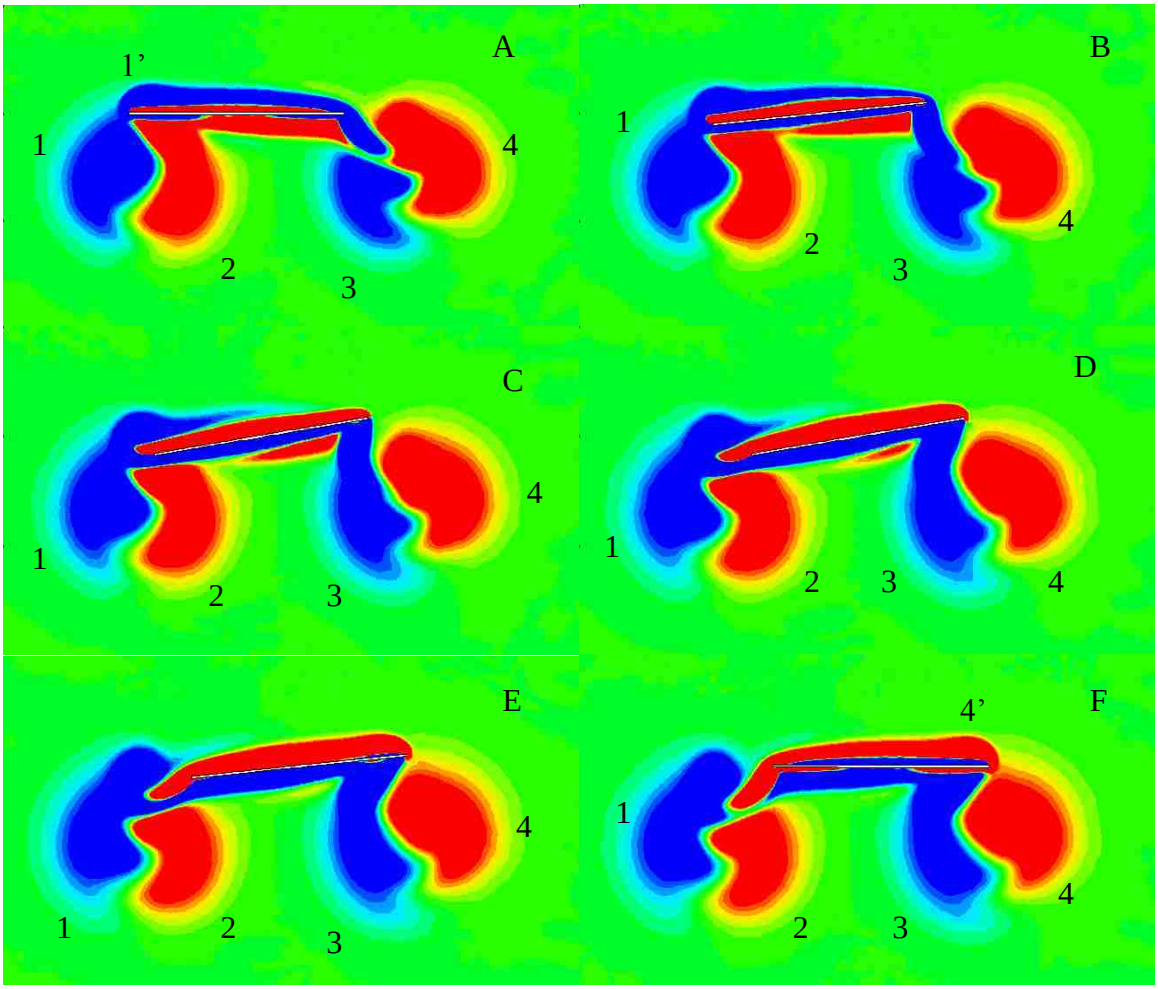

Figure 4-41: Z vorticity contours for Case 1.

Figure 4-42 illustrates the effect of reduced frequency with cases 5 and 7. The higher reduced frequency case produces much more intense vorticity than the lower reduced frequency case. However, the lower reduced frequency, since it has a larger amplitude of motion, has a correspondingly larger spread of weaker flow disturbances. The higher reduced frequency cases had dramatically larger lift coefficients than the lower reduced frequency cases. This is attributed to the stronger vortices and the stronger downward directed wake. Camber is more beneficial at lower reduced frequencies, where 1% camber increased lift by 8% at k=0.5, but by 2.5% at k=2.

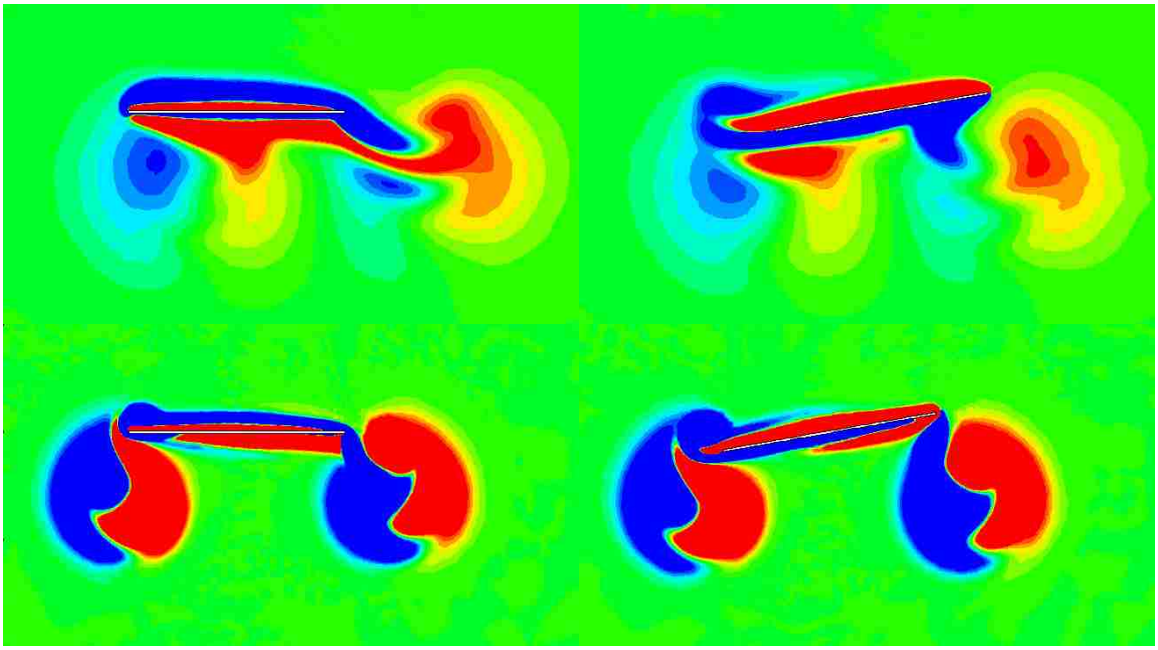

Figure 4-42: Effect of reduced frequency. Beginning of period in left column, one quarter period in right column. k=0.5 in top row, k=2 in bottom row.

Figure 4-43 illustrates the effect of Reynolds number with cases 9 and 11. Quite like the effect of reduced frequency, higher Reynolds numbers produce more intense vorticity. However, in contrast with reduced frequency, lift coefficient is only slightly increased with increasing Reynolds number. This effect is explained by the deflected wake being only slightly stronger at the higher Reynolds number. Thus, force generation for the leading edge/trailing edge switching mode is more sensitive to reduced frequency than Reynolds number. Also in contrast with the reduced frequency results, camber is more effective at higher Reynolds numbers. One percent increased lift by 3.4% at Re_c=500, but the increase was 4.8% at Re_c=2,500.

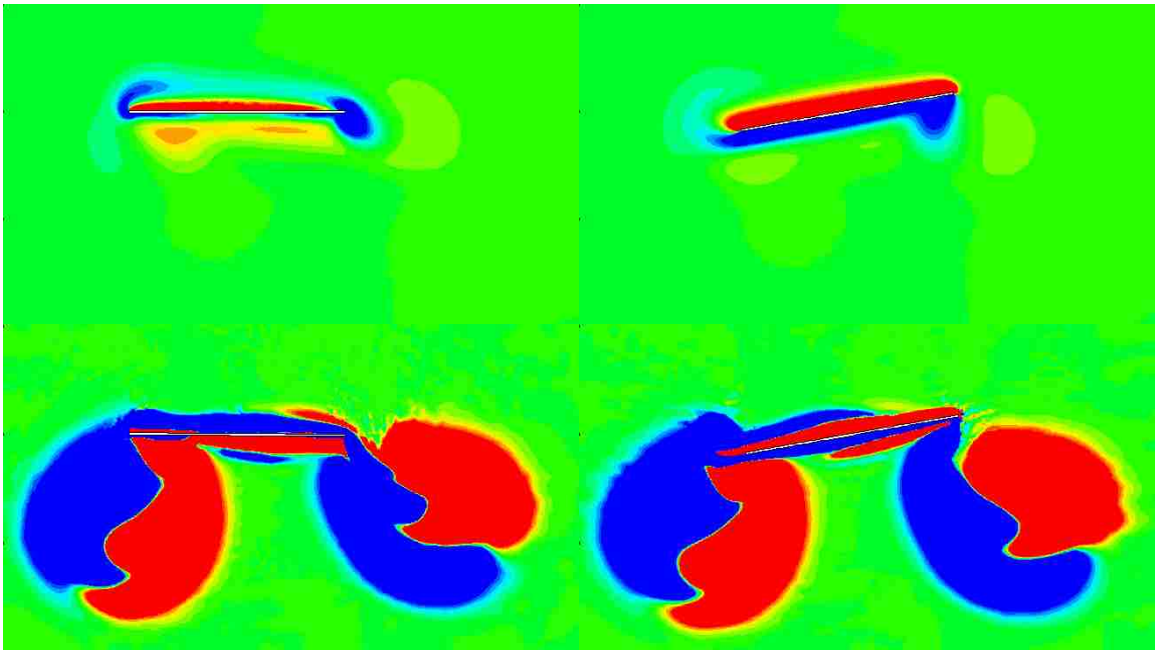

Figure 4-43: Effect of Rec. Beginning of period in left column, one quarter period in right column. Rec=100 in top row, Rec=2,500 in bottom row.

Figure 4-44 shows two other modes of flapping flight for comparison. In the top row is case 13, pure plunging with no rotation. The freestream is from the left, and the airfoil moves harmonically in the vertical direction. It is not a hovering mode. The bottom row of the figure is the normal hovering mode, case 14, in which the leading and trailing edges do not switch. Angle of attack amplitude, Reynolds number, and reduced frequency are the same as for case 1, for consistency. The pure plunging mode generates thrust through the reverse von Karman vortex street, a well established phenomena which is indicated by the row of alternating vortices aft of the airfoil. The normal hovering mode produces a net upward force, but large horizontal forces are present. Since the angle of attack only varies 10^{o} about the vertical, the airfoil is mostly vertical and produces forces mostly in the horizontal direction. Better performance could be obtained with a larger angle of attack variation; however, it is noted that the leading edge trailing edge switching mode appears advantageous, as also noted by Tang et al [149]. This mode has vortex shedding from both the leading and trailing edges. Vortices of opposite sense occur on the two edges and the situation reverses for the return stroke. For

example, a CCW vortex occurs on the leading edge and a CW vortex occurs on the trailing edge during the upstroke, but a CW vortex occurs on the leading edge and a CCW vortex occurs on the trailing edge during the downstroke.

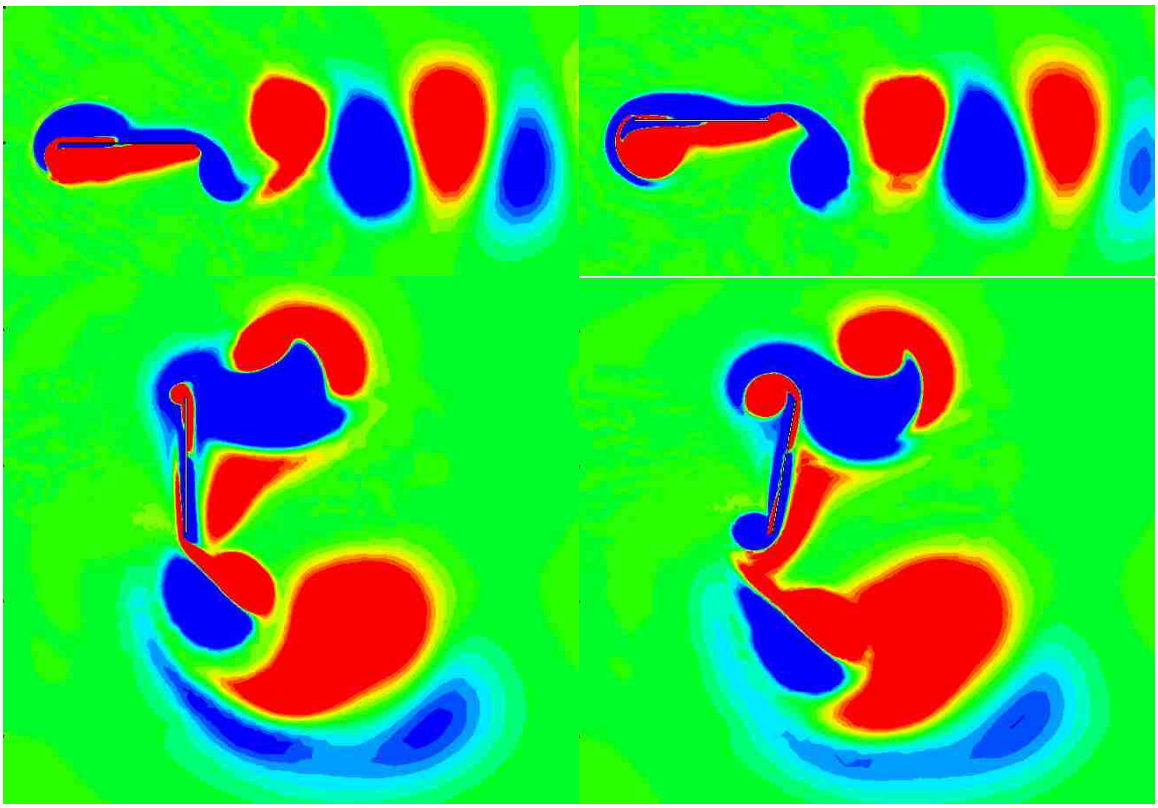

Figure 4-44: Two additional flapping flight modes. Rec=500, k=1. Beginning of period in left column, one quarter period in right column. Case 13 in top row, case 14 in bottom row.

5. CONCLUSIONS

The fixed-wing cases show that a tip vortex that strengthens with angle of attack is present over low Reynolds number (Re_c=500) wings in the 0^o – 45^o angle of attack range. This tip vortex is the dominant flow feature and explains many aspects of the flow behavior. Lift peaks at an angle of attack slightly greater than 20^o for all the wings, and is attributable to a vortex-dominated flow at that angle of attack. Behavior above this angle of attack varies differently for the rectangular wings and for the semi-ellipse wings, thus indicating the importance of planform shape. This behavior, generally a C_L decrease followed by a subsequent recovery, could be caused by tip vortices or the laminar separation bubble. Flow features include a tip vortex forcing streamlines rootward and creating highly three-dimensional, low velocity regions indicated by lower streamline density in the post-processed results. This tip vortex forces the adjacent streamlines to curl into a spiral vortex on the rectangular wings at high angles of attack; the spiral vortex then breaks down leading to the highly three-dimensional low velocity region. However, the semi-ellipse wings do not show such a clear tip vortex. Instead, a less coherent vortex is present toward the root. Among the semi-ellipse wing cases, only the non-cambered semi-ellipse at 45^o has a clear tip vortex similar to those in the rectangular wing cases. Surface streamtraces indicate separation, recirculation, and reattachment at higher angles of attack. Also, the 20^o case shows the most complicated topological pattern, reinforcing the significance of that angle of attack value. The flow patterns and C_L-α curves reveal significant differences from flow over wings at high Reynolds numbers which have well-defined tip vortex and clear stall angle of attack.

Of the three parameters experimentally investigated for flapping, angle of attack was found to have the largest effect. Wake size increases with angle of attack, and the leading edge vortex sheds earlier at higher angles of attack. The leading edge vortex shed sooner at the lower reduced frequency, and a larger area of entrained fluid is also apparent at the lower reduced frequency. Vortices are also larger at lower reduced frequencies. Shedding occurs earlier for rectangular wings than for semi-ellipse wings for flapping, but the same trend was not apparent for plunging. Thrust is generated for

both flapping and plunging. The mechanism for thrust generation is wake momentum, the formation of a jet.

Several important flow features have been identified. These include vortices shed from the two edges, circulation caused by the rotation of the airfoil, and the downward directed wake. This circulation and downward directed wake both create lift. Cambered airfoils create more lift than non-cambered airfoils at every Reynolds number and reduced frequency studied here, but camber is most beneficial at low reduced frequencies and large Reynolds numbers in this range. Reduced frequency has a much more profound effect than Reynolds number.

APPENDIX

PLUNGING MECHANISM BLUEPRINTS

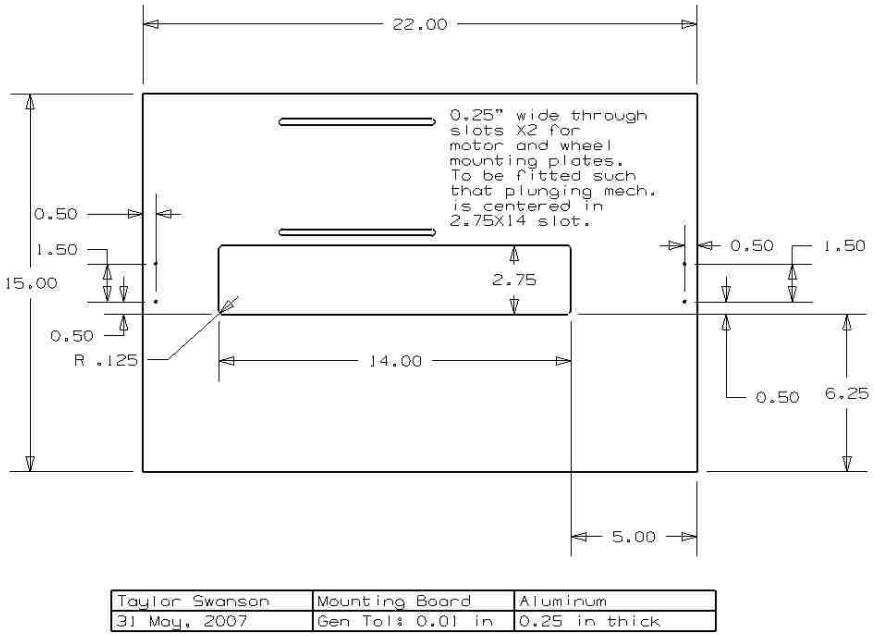

Figure A-1: Plunging mechanism mounting board.

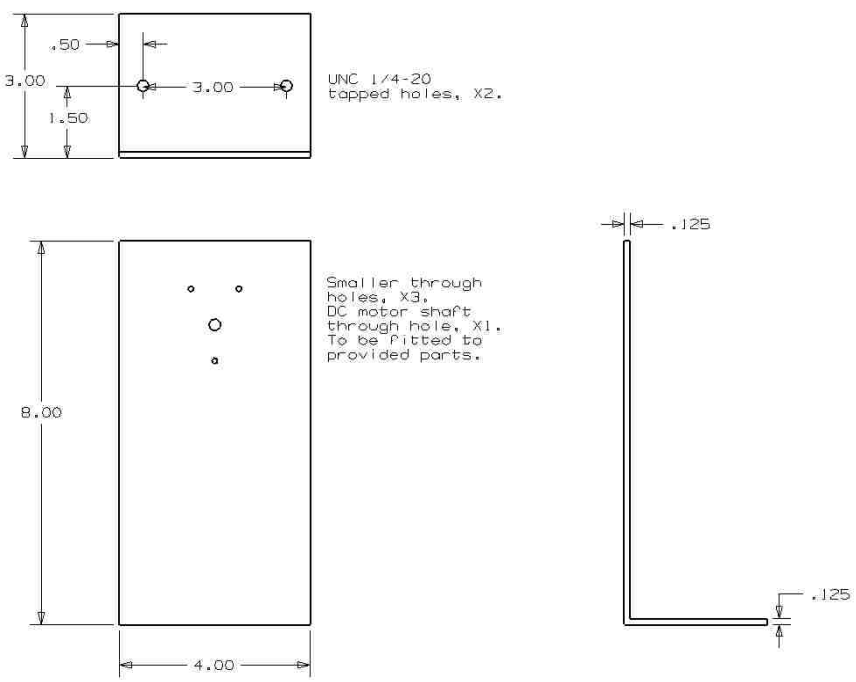

Figure A-2: Motor mounting bracket.

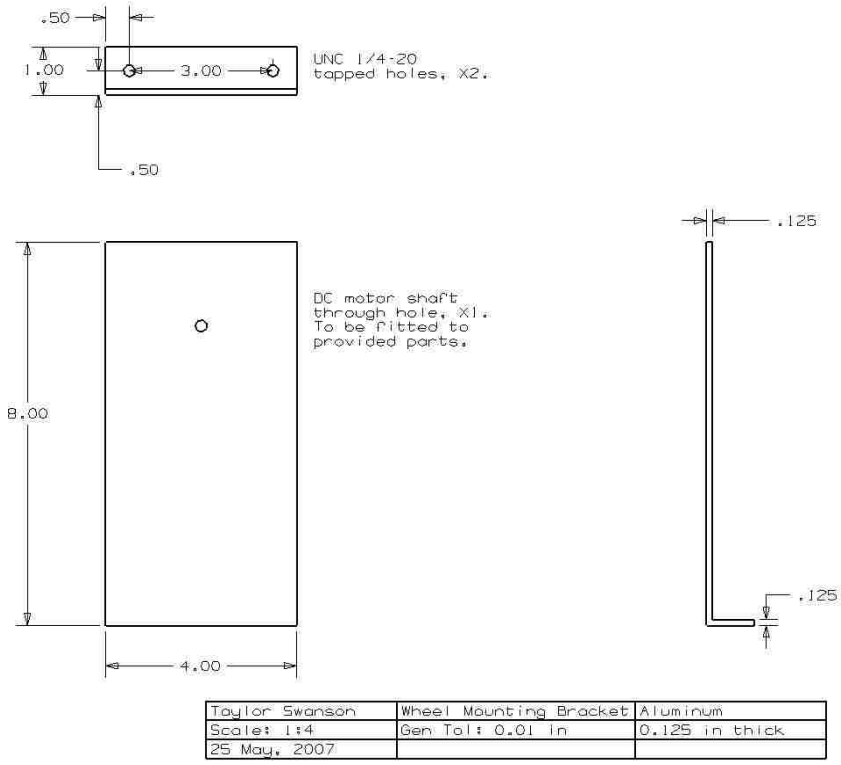

Figure A-3: Wheel mounting bracket.

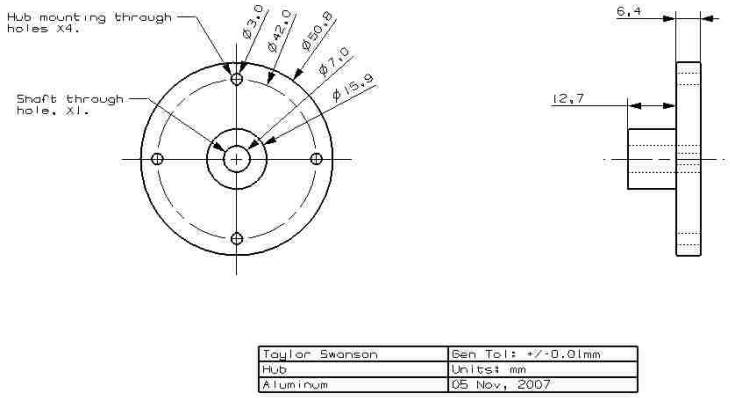

Figure A-4: Wheel hub.

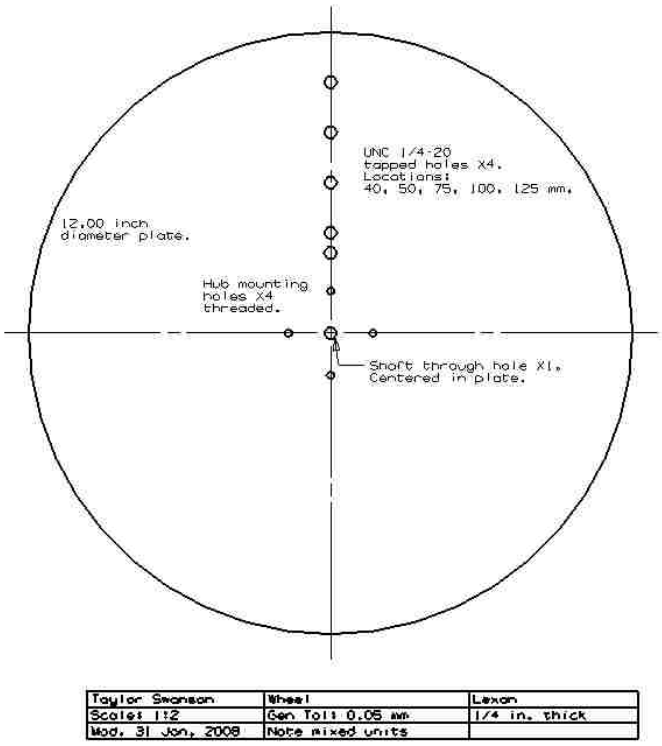

Figure A-5: Wheel.

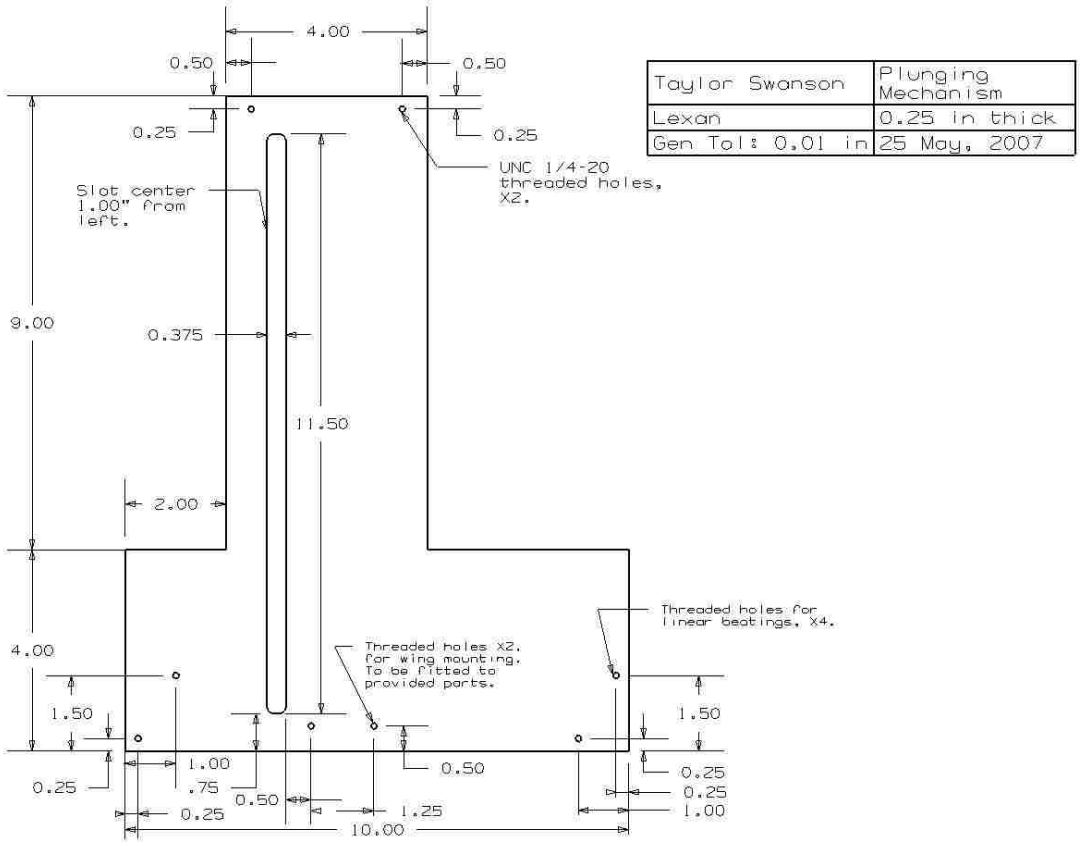

Figure A-6: Plunging slotted board.

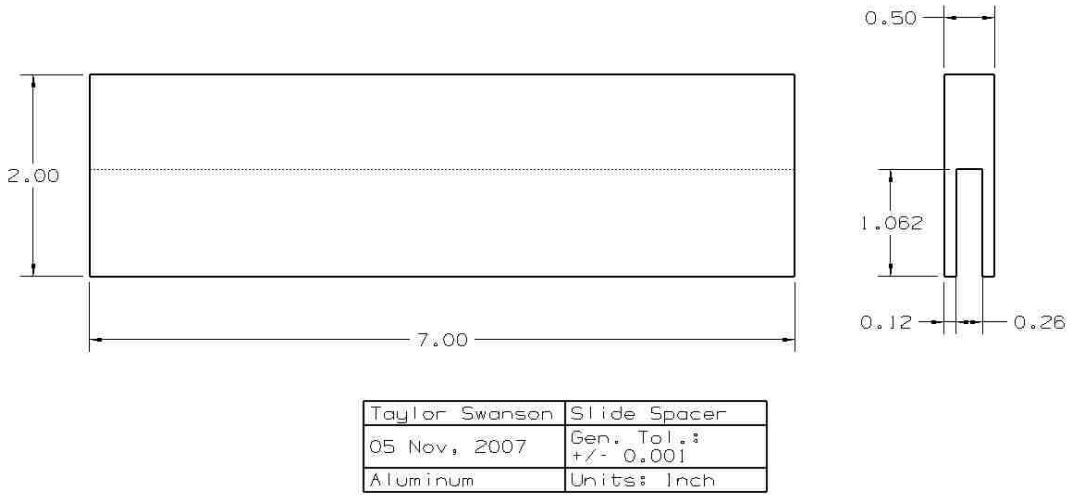

Figure A-7: Slide spacer bar.

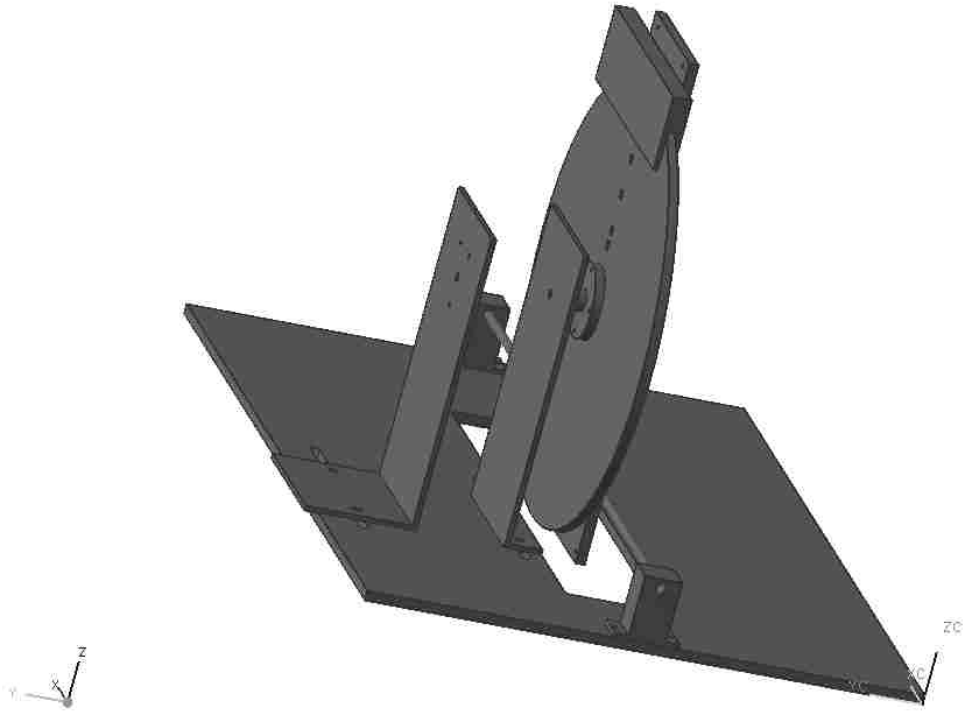

Figure A-8: Assembled view, from rear.

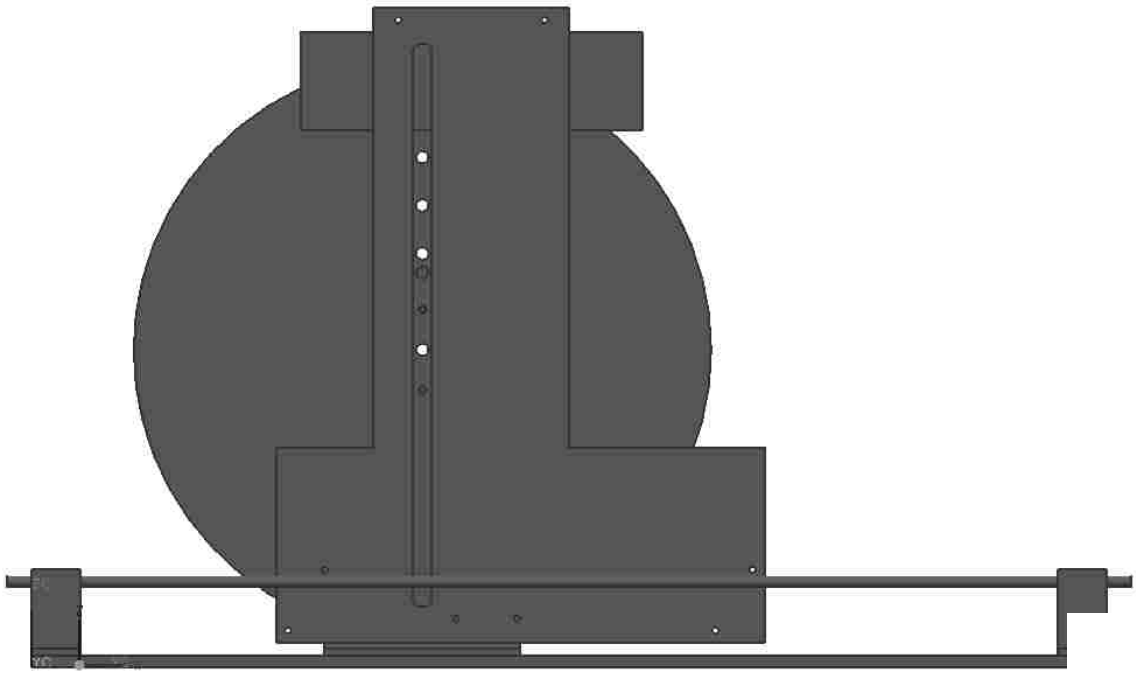

Figure A-9: Assembled view, from front.

BIBLIOGRAPHY

[1] Abtahi, A. A., and Marchman, J. F., "Aerodynamics of an Aspect Ratio 8 Wing at Low Reynolds Numbers," Journal of Aircraft, v. 22, pp. 628-634, July 1985.

[2] Adrian, R. J., "Particle Imaging Techniques for Experimental Fluid Mechanics," Annual Review of Fluid Mechanics, vol. 23, pp. 261-304, 1991.

[3] Adrian, R. J., "Scattering Particle Characteristics and Their Effect on Pulsed Laser Measurements of Fluid Flow: Speckle Velocimetry vs. Particle Image Velocimetry," Applied Optics, vol. 23, pp. 1690-1691, 1984.

[4] Adrian, R. J., "Twenty Years of Particle Image Velocimetry," Experiments in Fluids, vol. 39, pp. 159-169, 2005.

[5] Adrian, R. J., and Yao, C.-S., "Pulsed Laser Technique Application to Liquid and Gas Flows and the Scattering Power of Seed Materials," Applied Optics, v. 224, n. 1, pp. 44-52, Jan. 1985.

[6] Alford Jr., L. D., and Altman, A., "Foundation of a New Investigation of Natural Flight Characteristics and Theory," AIAA 2005-1357.

[7] Altshuler, D. L., Dickson, W. B., Vance, J. T., Roberts, S. P., and Dickinson, M. H., "Short-Amplitude High-Frequency Wing Strokes Determine the Aerodynamics of Honeybee Flight," Proceedings of the National Academy of Sciences, vol. 102, no. 50, pp. 18213-18218, 2005.

[8] Altshuler, D. L., Dudley, R., and Ellington, C. P., "Aerodynamic Forces of Revolving Hummingbird Wings and Wing Models," Journal of Zoology, vol. 264, pp. 327-332, 2004.

[9] Anderson, J. M., Streitlien, K., Barrett, D. S., and Triantafyllou, M. S., "Oscillating Foils of High Propulsive Efficiency," Journal of Fluid Mechanics, vol. 360, pp. 41-72, 1998.

[10] Ansari, Salman A., Knowles, Kevin, and Zbikowski, Rafai, "Insectlike Flapping Wings in Hover Part 1: Effect of Wing Kinematics," Journal of Aircraft, v. 45, n. 6, Nov-Dec 2008, pp. 1945-1975.

[11] Ansari, Salman A., Knowles, Kevin, and Zbikowski, Rafai, "Insectlike Flapping Wings in Hover Part 1: Effect of Wing Geometry," Journal of Aircraft, v. 45, n. 6, Nov-Dec 2008, pp. 1976-1990.

[12] "Autonomous Rotorcraft Sniper System," http://www.sdl.usu.edu/programs/arss, accessed 23 Apr, 2009.

[13] Biber, K., Ol, M. V., and Tilman, C. P., "Some Examples of Airfoil Design For Future Unmanned Air Vehicle Concepts," AIAA 2004-1050.

[14] Birch, J. M., and Dickinson, M. H., "The Influence of Wing-Wake Interactions on the Production of Aerodynamic Forces in Flapping Flight," Journal of Experimental Biology, vol. 206, pp. 2257-2272, 2003.

[15] Birch, J. M., and Dickinson, M. H., "Spanwise Flow and the Attachment of the Leading-Edge Vortex on Insect Wings," Nature, vol. 412, pp. 729-733, 2001.

[16] Birch, J. M., Dickson, W. B., and Dickinson, M. H., "Force Production and Flow Structure of the Leading Edge Vortex on Flapping Wings at High and low Reynolds Numbers," Journal of Experimental Biology, vol. 207, pp. 1063-1072, 2004.

[17] Blondeaux, Paolo, Guglielmini, Laura, and Triantafyllou, Michael S., "Chaotic Flow Generated by an Oscillating Foil," AIAA Journal, v. 43, n. 4, Apr 2005, pp. 918-921.

[18] Carmichael, B. H., "Low Reynolds Number Airfoil Survey, Vol. I," NASA-CR-165803, 1982.

[19] Chandar, D. D. J., and Damodaran, M., "Computational Study of Unsteady Low-Reynolds-Number Airfoil Aerodynamics Using Moving Overlapping Meshes," AIAA Journal, v. 46, n. 2, Feb 2008, pp. 429-438.

[20] Chasman, D., and Chakravarthy, S., "Computational and Experimental Studies of Asymmetric Pitch/Plunge Flapping- The Secret of Biological Flyers," AIAA 2001-0859.

[21] Choi, D. H., and Landweber, L., "Inviscid Analysis of Two-Dimensional Airfoils in Unsteady Motion Using Conformal Mapping," AIAA Journal, v. 28, n. 12, Dec. 1990, pp. 2025-2033.

[22] Choi, D. H., and Lee, E. H., "Prediction of Separation Bubbles Using Improved Transition Criterion with Two-Equation Turbulence Model," AIAA Journal, vol. 33, no. 8, pp. 1512-1514, 1995.

[23] Chong, M. S., Perry, A. E., and Cantwell, B. J., "A General Classification of Three-Dimensional Flow Fields," Physics of Fluids A, v. 2, n. 5, pp. 765-777, May 1990.

[24] Cosyn, P., and Vierendeels, J., "Numerical Investigation of Low Aspect Ratio Wings at Low Reynolds Numbers," Journal of Aircraft, v. 43, n. 3, pp. 713-722, May 2006.

[25] Davis, R. L., and Carter, J. E., "Counterrotating Streamline Pattern in a Transitional Separation Bubble," AIAA Journal, vol. 24, pp. 850-851, 1986.

[26] Defense Advanced Research Projects Agency, "Fiscal Year 2001 Budget Estimates," Technical Report, U. S. Department of Defense, http://www.darpa.mil/body/pdf/DARPAFY2001BudgetEstimates.pdf, February 2000.

[27] DeLaurier, J. D., "An Aerodynamic Model for Flapping-Wing Flight," Aeronautical Journal, vol. 97, pp. 153-162, 1993.

[28] DeLaurier, J. D., and Harris, J. M., "Experimental Study of Oscillating-Wing Propulsion," Journal of Aircraft, v. 19, n. 3, pp. 368-373, 1982.

[29] Dickson, W. B., and Dickinson, M. H., "The Effect of Advance Ratio on the Aerodynamics of Revolving Wings," Journal of Experimental Biology, vol. 207, pp. 4269-4281, 2004.

[30] Dickinson, M. H., "The Effects of Wing Rotation on Unsteady Aerodynamic Performance at Low Reynolds Numbers," Journal of Experimental Biology, vol. 192, pp. 179-206, 1994.

[31] Dickinson, M. H., "Unsteady Mechanisms of Force Generation in Aquatic and Aerial Locomotion," American Zoology, vol. 36, pp. 537-554, 1996.

[32] Dickinson, M. H., and Götz, K. G., "Unsteady Aerodynamic Performance of Model Wings at Low Reynolds Numbers," Journal of Experimental Biology, vol. 174, pp. 45-64, 1993.

[33] Dickinson, M. H., and Götz, K. G., "The Wake Dynamics and Flight of the Fruit Fly Drosophila Melanogaster," Journal of Experimental Biology, vol. 199, pp. 2085-2104, 1996

[34] Dickinson, M. H., Lehman, F.-O., and Sane, S. P., "Wing Rotation and the Aerodynamic Basis of Insect Flight," Science, vol. 284, pp. 1954-1960, 1999.

[35] Dong, H., Mittal, R., and Najjar, F. M., "Wake Topology and Hydrodynamic Performance of Low-Aspect-Ratio Flapping Foils," Journal of Fluid Mechanics, v. 566, 2006, pp. 309-343.

[36] Dornheim, Michael A., "Tiny Drones May be Soldier's New Tool," Aviation Week and Space Technology, vol. 148, no. 23, pp. 42, 43, 47, 48, June 1998.

[37] Elimelech, Y., Arieli, R., and Iosilevskii, G., "Flow over NACA-0009 and Eppler-61 Airfoils at Reynolds Numbers 5,000 to 60,000," AIAA Journal, vol. 45, no. 10, Oct. 2007, pp. 2414-2421.

[38] Ellington, C. P., "Insects Versus Birds: The Great Divide," AIAA 2006-35.

[39] Ellington, C. P., "The Novel Aerodynamics of Insect Flight: Applications to Micro-Air Vehicles," Journal of Experimental Biology, vol. 202, pp. 3439-3448, 1999.

[40] Ellington, C. P., van den Berg, C., Willmott, A. P., and Thomas, A. L. R., "Leading-Edge Vortices in Insect Flight," Nature, vol. 384, pp. 626-630, 1996.

[41] Emblemsvag, J-E., and Candler, G., "Simulation of the Unsteady Aerodynamics of the Fruit Fly (Drosophila,)" AIAA 2004-2672.

[42] Fitzgerald, E. J., and Mueller, T. J., "Measurements in a Separation Bubble on an Airfoil Using Laser Velocimetry," AIAA Journal, vol. 28, pp. 584-592, 1990.

[43] "Flag and Footprints Mission to Mars: Preliminary Design Review Two," NASA no. 19990025832, 1998.

[44] FLUENT, v6.3.26, Fluent, Inc., Lebanon, NH, 2006.

[45] Freymuth, P., "Propulsive Vortical Signature of Plunging and Pitching Airfoils," AIAA Journal, v. 26, n. 7, pp. 881-883, Jul 1988.

[46] Freymuth, P., "Thrust Generation by an Airfoil in Hover Modes," Experiments in Fluids, v. 9, pp. 17-24, 1990.

[47] Freymuth, Peter, "Concepts and Applications of Dynamic Separation for Agility and Super-Maneuverability of Aircraft: An Assessment," NASA Ames Research Center, Physics of Forced Unsteady Separation, pp. 309-316, N94-34966 10-34, 1992.

[48] Fry, S. N., Sayaman, R., and Dickinson, M. H., "The Aerodynamics of Hovering Flight in Drosophila," Journal of Experimental Biology, vol. 208, pp. 2303-2318, 2005.

[49] Gallon, M., "Application of the Hydrogen Bubble Visualization Method to the Water Tunnels of ONERA," ONERA TP no. 1989-107, 1989.

[50] Geller, E. W., "An Electrochemical Method of Visualizing the Boundary Layer," Journal of Aeronautical Sciences, vol. 22, no. 12, pp. 376-380, 1955.

[51] Goldstein, R. J., ed., "Fluid Mechanics Measurements," 2nd ed., Taylor & Francis Publishing, Philadelphia, 1996.

[52] Guilmineau, E., and Queutey, P., "A Numerical Simulation of Vortex Shedding from an Oscillating Circular Cylinder," Journal of Fluids and Structures, v. 16, n. 6, pp. 773-794, 2002.

[53] Hall, Kenneth C., Pigott, Steven A., and Hall, Steven R., "Power Requirements for Large-Amplitude Flapping Flight," Journal fo Aircraft, v. 35, n. 3, May-Jun 1998, pp. 352-361.

[54] Hedenström, A., Van Griethuijsen, L., Rosen, M., and Spedding, G. R., "Vortex Wakes of Birds: Recent Developments Using Digital Particle Image Velocimetry in a Wind Tunnel," Journal of Animal Biology, vol. 56, no. 4, pp. 535-549, 2006.

[55] Ho, Steven, Nassef, Hany, Pornsinsirirak, Nick, Tai, Yu-Chong, and Ho, Chih-Ming, "Unsteady Aerodynamics and Flow Control for Flapping Wing Flyers," Progress in Aerospace Sciences, v. 39, 2003, pp. 635-681.

[56] Hong, YoungSun, and Altman, Aaron, "Lift From Spanwise Flow in Simple Flapping Wings," Journal of Aircraft, v. 45, n. 4, Jul-Aug 2008, pp. 1206-1216.

[57] Hong, YoungSun, and Altman, Aaron, "Streamwise Vorticity in Simple Mechanical Flapping Wings," Journal of Aircraft, v. 44, n. 5, Sep-Oct 2007, pp. 1588-1597.

[58] Horton, H. P., "Laminar Separation Bubbles in Two and Three-Dimensional Incompressible Flow," PhD Dissertation, Univ. London, U.K.

[59] Hsiao, F.-B., Lin, C.-Y., Liu, Y.-C., Wand, D.-B., Wei, C.-Y., Chiang, C.-H., and Hsu, C.-C., "Investigation of Aerodynamic Performance on Low-Aspect Ratio Wings at Low Reynolds Numbers," AIAA 2006-1266.

[60] Isaac, K. M., Colozza, A., and Rolwes, J., "Force Measurements on a Flapping and Pitching Wing at Low Reynolds Numbers," AIAA-2006-0450.

[61] Isaac, K. M., Rolwes, J. and Colozza, A., "Aerodynamics of a Flapping and Pitching Wing using Simulations and Experiments," AIAA Journal, v. 46, n. 6, pp. 1505-1515, Jun, 2008.

[62] Isaac, K. M., Rolwes, J., and Colozza, A., "Unsteady Flow Features of a Flapping and Pitching Wing at Low Reynolds Number," AIAA-2006-3145.

[63] Isaac, K. M., Shivaram, P. and DalBello, T., "Low Re, High α Aerodynamics with Controlled Wing Kinematics," AIAA 2003-4019.

[64] Isogai, K., Shinmoto, Y., and Watanabe, Y., "Effects of Dynamic Stall on Propulsive Efficiency and Thrust of Flapping Airfoil," AIAA Journal, v. 37, n. 10, Oct 1999, pp. 1145-1151.

[65] James, E. C., "Lifting-Line Theory for an Unsteady Wing as a Singular Perturbation Problem," Journal of Fluid Mechanics, v. 70, n. 4, 1975, pp. 753-771.

[66] Jian, T., and Ke-Qin, Z., "Numerical and Experimental Study of Flow Structure of Low-Aspect-Ratio Wing," Journal of Aircraft, vol. 41, no. 5, Sep-Oct 2004, pp. 1196-1201.

[67] Jones, K. D., Dohring, C. M., and Platzer, M. F., "Experimental and Computational Investigation of the Knoller-Betz Effect," AIAA Journal, v. 36, n. 7, Jul 1998, pp. 1240-1246.

[68] Kaplan, S. M., Altman, A., and Ol, M., "Wake Vorticity Measurements for Low Aspect Ratio Wings at Low Reynolds Number," Journal of Aircraft, v. 44, n. 1, pp. 241-251, Jan. 2007.

[69] Kaya, M., and Tuncer, I., "Nonsinusoidal Path Optimization of a Flapping Airfoil," AIAA Journal, v. 45, n. 8, pp. 2075-2082, 2007.

[70] Katz, J., and Plotkin, A., "Low-Speed Aerodynamics," 2nd ed., Cambridge University Press, 2001.

[71] Keane, R. D., and Adrian, R. J., "Optimization of Particle Image Velocimeters. Part I: Double Pulsed Systems," Measurement Science and Technology, v. 1, pp. 1202-1215, 1990.

[72] Keane, R. D., and Adrian, R. J., "Theory of Cross-Correlation Analysis of PIV Images," Applied Scientific Research, v. 49, pp. 191-215, 1992.

[73] Kemp, Nelson H., and Homicz, Gregory, "Approximate Unsteady Thin-Sirfoil Theory for Subsonic Flow," AIAA Journal, v. 14, n. 8, Aug 1976, pp. 1083-1089.

[74] Koochesfahani, M., "Vortical Patterns in the Wake of an Oscillating Airfoil," AIAA Journal, v. 27, n. 9, 1989, pp. 1200-1205.

[75] Kunz, P. J., and Kroo, I. M., "Analysis, Design, and Testing of Airfoils for use at Ultra-Low Reynolds Numbers," in Fixed, Flapping, and Rotary Wing Aerodynamics for Micro Air Vehicle Applications, T. Mueller, ed., AIAA Prog. Astro. Aero. v. 195, 2001.

[76] Kwon, K., and Park, S. O., "Aerodynamic Characteristics of an Elliptic Airfoil at Low Reynolds Number," Journal of Aircraft, v. 42, n. 6, pp. 1642-1644, Nov. 2005.

[77] Lai, J. C. S., and Platzer, M. F., "Jet Characteristics of a Plunging Airfoil," AIAA Journal, v. 37, n. 12, pp. 1529-1537, 1999.

[78] Lai, Joseph C. S., and Platzer, Max F., "Characteristics of a Plunging Airfoil at Zero Freestream Velocity," AIAA Journal, v. 39, n. 3, Mar 2001, pp. 531-534.

[79] Laitone, E. V., "Aerodynamic Lift at Reynolds Numbers Below $7X10^4$," AIAA Journal, v. 34, n. 9, Sep. 1996, pp. 1941-1942.

[80] Laitone, E. V., "Wind Tunnel Tests of Wings and Rings at Low Reynolds Numbers," in Fixed, Flapping, and Rotary Wing Aerodynamics for Micro Air Vehicle Applications, T. Mueller, ed., AIAA Prog. Astro. Aero. v. 195, 2001.

[81] Laitone, E. V., "Wind Tunnel Tests of Wings at Reynolds Numbers Below 70,000," Experiments in Fluids, v. 23, n. 5, Nov. 1997, pp. 405-409.

[82] Lauder, George V., "Flight of the Robofly," Nature, vol. 412, pp. 688-689, 16 Aug, 2001.

[83] Lee, J.-S., Kim, C., and Kim, K. H., "Design of Flapping Airfoil for Optimal Aerodynamic Performance in Low-Reynolds Number Flows," AIAA Journal, v. 44. n. 9, pp. 1960-1972, 2006.

[84] Lee, J.-S., Kim, J.-H., and Kim, C., "Numerical Study on the Unsteady Force Generation Mechanism of Insect Flapping Motion," AIAA Journal, v. 46, n. 7, pp. 1835-1848, Jul 2008.

[85] Lentink, D., and Gerritsma, M., "Influence of Airfoil Shape on Performance in Insect Flight," AIAA 2003-3447.

[86] Lewin, G. C., and Haj-Hariri, H., "Modelling Thrust Generation of a Two-Dimensional Heaving Airfoil in Viscous Flow," Journal of Fluid Mechanics, v. 492, pp. 339-362, Oct 2003.

[87] Lian, Y., and Shyy, W., "Laminar-Turbulent Transition of a Low Reynolds Number Rigid or Flexible Airfoil," AIAA Journal, vol. 45, no. 7, Jul. 2007, pp. 1501-1513.

[88] Lighthill, M. J., "Attachment and Separation in Three-Dimensional Flow," in "Laminar Boundary Layers," ed. by L. Rosenhead, New York, 1963, pp. 48-88.

[89] Lighthill, M. J., "On the Weis-Fogh Mechanism of Lift Generation," Journal of Fluid Mechanism, vol. 60, part 1, pp. 1-17, 1973.

[90] Lissaman, P. B. S., "Low-Reynolds-Number Airfoils," Annual Review of Fluid Mechanics, v. 15, 1983, pp. 223-239.

[91] Liu, H., and Kawachi, K., "A Numerical Study of Insect Flight," Journal of Computational Physics, v. 146, pp. 124-156, 1998.

[92] Liu, Hao, "Computational Biological Fluid Dynamics: Digitizing and Visualizing Animal Swimming and Flying," Journal of Integrated Comparative Biology, vol. 42, pp. 1050-1059, 2002.

[93] Liu, T., Kuykendoll, K., Rhew, R., and Jones, S., "Avian Wing Geometry and Kinematics," AIAA Journal, vol. 44, no. 5, pp. 954-963, May 2006.

[94] Liu, Tianshu, "Comparative Scaling of Flapping- and Fixed- Wing Flyers," AIAA Journal, v. 44, n. 1, Jan 2006, pp. 24-33.

[95] Liu, Tianshu, "Time-Area-Averaged Momentum Stream Tube Model for Flapping Flight," Journal of Aircraft, v. 44, n. 2, Mar-Apr 2007, pp. 459-466.

[96] Lua, K. B., Lim, T. T., Yeo, K. S., and Oo, G. Y., "Wake-Structure Formation of a Heaving Two-Dimensional Elliptic Airfoil," AIAA Journal, v. 45, n. 7, pp. 1571-1583, Jul 2007.

[97] Marden, James H., "Maximum Lift Production During Takeoff in Flying Animals," Journal of Experimental Biology, vol. 130, pp. 235-258, 1987.

[98] Marxen, O., and Henningson, D. S., "Numerical Simulation of the Bursting of a Laminar Separation Bubble," AIAA 2007-538.

[99] Maxworthy, T., "Experiments on the Weis-Fogh Mechanism of Lift Generation by Insects in Hovering Flight. Part 1. Dynamics of the 'Fling,'" Journal of Fluid Mechanics, vol. 93, part 1, pp. 47-63, 1979.

[100] Maxworthy, T., "The Fluid Dynamics of Insect Flight," Annual Review of Fluid Mechanics, vol. 13, pp. 329-350, 1981.

[101] Maxworthy, T., "The Formation and Maintenance of a Leading-Edge Vortex During the Forward Motion of an Animal Wing," Journal of Fluid Mechanics, v. 587, 2007, pp. 471-475.

[102] McMasters, J. H., and Henderson, M. L., "Low-Speed Single-Element Airfoil Synthesis," NASA SP-2085, pp. 1-33, 1979.

[103] Milano, M., and Gharib, M., "Uncovering the Physics of Flapping Flat Plates with Artificial Evolution," Journal of Fluid Mechanics, vol. 534, pp. 403-409, 2005.

[104] Mueller, T. J., and DeLaurier, J. D., "Aerodynamics of Small Vehicles," Annual Review of Fluid Mechanics, vol. 35, pp. 89-111, 2003.

[105] Mueller, T. J., and DeLaurier, J. D., "An Overview of Micro Air Vehicle Aerodynamics," in Fixed, Flapping, and Rotary Wing Aerodynamics for Micro Air Vehicle Applications, T. Mueller, ed., AIAA Prog. Astro. Aero. v. 195, 2001.

[106] Murdin, M., and Foster, S., "Inexpensive Quantitative Flow Visualization," AIAA Paper 2000-0016.

[107] Nagai, Hiroto, Isogai, Koji, Fujimoto, Tatsumi, and Hayase, Toshiyuki, "Experimental and Numerical Study of Forward Flight Aerodynamics of Insect Flapping Wing." AIAA Journal, v. 47, n. 3, March 2009, pp. 730-742.

[108] Null, W., and Shkarayev, S., "Effect of Camber on the Aerodynamics of Adaptive-Wing Micro Air Vehicles," Journal of Aircraft, vol. 42, no. 6, Nov-Dec 2005, pp. 1537-1542.

[109] Okamoto, M., and Azuma, A., "Experimental Study on Aerodynamic Characteristics of Unsteady Wings at Low Reynolds Number," AIAA Journal, v. 43, n. 12, Dec 2005, pp. 2526-2536.

[110] Oswatitsch, K., "The Conditions for the Separation of Boundary Layers," in "Contributions to the Development of Gas Dynamics" ed. by W. Schneider and M. Platzer, Braunschweig/Vieweg, pp. 6-18, 1980.

[111] Parker, K., Soria, J., and von Ellenreider, K. D., "Thrust Measurements From a Finite-Span Wing," AIAA Journal, v. 45, n. 1, pp. 58-70, 2007.

[112] Parker, K., von Ellenrieder, K. D., and Soria, J., "Morphology of the Oscillatory Flow Past a Finite-Span Wing at Low Reynolds Number," Journal of Fluid Mechanics, v. 571, 2007, pp. 327-357.

[113] Parmalee, Patricia J., "Good Scouts – The Buzz About Tiny UAVS," Aviation Week and Space Technology, vol. 161, no. 10, pp. 78, Sept. 2004.

[114] Pelletier, A., and Mueller, T. J., "Low Reynolds Number Aerodynamics of Low-Aspect Ratio, Thin/Flat/Cambered-Plate Wings," Journal of Aircraft, v. 37, n. 5, pp. 825-832, Sep. 2000.

[115] Perry, A. E. and Chong, M. S., "A Description of Eddying Motions and Flow Patterns using Critical Point Concepts," Ann. Rev. Fluid Mech., v. 19, pp. 125-155, Jan. 1987.

[116] Perry, A. E., and Steiner, T. R., "Large-Scale Vortex Structures in Turbulent Wakes Behind Bluff Bodies, Parts 1 and 2," Journal of Fluid Mechanics, v. 174, pp. 233-298, 1987.

[117] Philips, P., East, R., and Pratt, N., "An Unsteady Lifting Line Theory of Flapping Wings with Application to the Forward Flight of Birds," Journal of Fluid Mechanics, vol. 112, pp. 97-125, Nov. 1981.

[118] Pines, D. J., and Bohorquez, F., "Challenges Facing Future Micro-Air-Vehicle Development," Journal of Aircraft, v. 43, n. 2, pp. 290-305, Mar-Apr 2006.

[119] PIVview Version 2.1, by PivTec, Gottingen, Germany, 2003.

[120] "Planetary Exploration Using Biomimetics: An Entomopter for Flight on Mars," NASA Institute for Advanced Concepts, Project Final Report, Ohio Aerospace Institute, October 2002.

[121] Platzer, Max F., Jones, Kevin D., Young, John, and Lai, Joseph C. S., "Flapping-Wing Aerodynamics: Progress and Challenges," AIAA Journal, v. 46, n. 9, Sep. 2008, pp. 2136-2148.

[122] Raffel, M., Willert, C., and Kompenhans, J., "Particle Image Velocimetry, a Practical Guide," Springer, New York, 1998.

[123] Ramamurti, R., and Sandberg, W. C., "A Three-Dimensional Computational Study of the Aerodynamic Mechanisms of Insect Flight," Journal of Experimental Biology, vol. 205, pp. 1507-1518, 2002.

[124] Ramamurti, Ravi, and Sandberg, William, "Computations of Insect and Fish Locomotion with Applications to Unconventional Unmanned Vehicles," AIAA Journal, v. 46, n. 9, Sep 2008, pp. 2178-2190.

[125] Ramamurti, Ravi, and Sandberg, William, "Simulation of Flow About Flapping Airfoils Using Finite Elelemt Incompressible Flow Solver," AIAA Journal, v. 39, n. 2, Feb 2001, pp. 253-260.

[126] Ramasamy, M., and Leishman, G., "Phase-Locked Particle Image Velocimetry Measurements of a Flapping Wing," Journal of Aircraft, v. 43, n. 6, pp. 1867-1875, 2006.

[127] Rayner, J. M. V., "Flight Mechanics and Constraints on Flight Performance," Israel Journal of Zoology, v. 41, n. 3, pp. 321-342, 1995.

[128] Ricci, R., and Montelpare, S., "A Quantitative IR Thermographic Method to Study the Laminar Separation Bubble Phenomenon," International Journal of Thermal Sciences, v. 44, pp. 709-719, 2005.

[129] Sane, S. P., and Dickinson, M. H., "The Aerodynamic Effects of Wing Rotation and a Revised Quasi-Steady Model of Flapping Flight," Journal of Experimental Biology, vol. 205, pp. 1087-1096, 2002.

[130] Sane, S. P., and Dickinson, M. H., "The Control of Flight Force by a Flapping Wing: Lift and Drag Production," Journal of Experimental Biology, vol. 204, pp. 2607-2626, 2001.

[131] Selig, M. S., Guglielmo, J. J., Broern, A. P., and Giguere, P., "Experiments on Airfoils at Low Reynolds Numbers," AIAA 1996-0062.

[132] Selig, M. S., "The Design of Airfoils at Low Reynolds Numbers," AIAA 85-0074.

[133] Shyy, W., and Liu, H., "Flapping Wings and Aerodynamic Lift: The Role of Leading-Edge Vortices," AIAA Journal, v. 45, n. 12, pp. 2817-2819, Dec 2007.

[134] Shyy, Wei, Trizila, Pat, Kang, Chang-kwon, and Aono, Hikaru, "Can Tip Vortices Enhance Lift of a Flapping Wing?" AIAA Journal, v. 47, n. 2, Feb 2009, pp. 289-293.

[135] Soviero, Paulo A. O., "Generalized Vortex Lattice Method for Oscillating Thin Airfoil in Subsonic Flow," AIAA Journal, v. 31, n. 12, Dec 1992, pp. 2380-2382.

[136] Spedding, G. R., Hedenström, A., and Rosén, M., "Quantitative Studies of the Wakes of Freely Flying Birds in a Low-Turbulence Wind Tunnel," Experiments in Fluids, vol. 34, pp. 291-303, 2003.

[137] Spedding, G. R., and Lissaman, P. B. S., "Technical Aspects of Microscale Flight Systems," Journal of Avian Biology, vol. 29, no. 4, Dec. 1998, pp. 458-468.

[138] Sun, M., and Tang, J., "Unsteady Aerodynamic Force Generation by a Model Fruit Fly Wing in Flapping Motion," Journal of Experimental Biology, vol. 205, pp. 55-70, 2002.

[139] Sun, M. and Yu, X., "Aerodynamic Force Generation in Hovering Flight in a Tiny Insect," AIAA Journal, vol. 44, no. 7, pp. 1532-1541, July 2006.

[140] Sunada, S., Kawachi, K., Matsumoto, A., and Sakaguchi, A., "Unsteady Forces on a Two-Dimensional Wing in Plunging and Pitching Motions," AIAA Journal, v. 39, n. 7, July 2001, pp. 1230-1239.

[141] Sunada, S., Ozaki, K., Tanaka, M., Yasuda, T., Yasuda, K., and Kawachi, K., "Airfoil Characteristics at a Low Reynolds Number," Journal of Flow Visualization and Image Processing, vol. 7, no. 3, pp. 207-215, 2000.

[142] Sunada, S., Yasuda, T., Yasuda, K., and Kawachi, K., "Comparison of Wing Characteristics at an Ultralow Reynolds Number," Journal of Aircraft, vol. 39, no. 2, pp. 331-338, 2002.

[143] Swanson, T. A., and Isaac, K. M., "Aerodynamics of Flapping and Plunging Wings Using Particle Image Velocimetry Techniques," AIAA 2009-1271.

[144] Swanson, T. A., and Isaac, K. M., "Low Re, High Alpha Wing Aerodynamics for Micro Air Vehicle Applications," AIAA 2008-0421.

[145] Swanson, T. A., and Isaac, K. M., "Planform and Camber Effects on the Aerodynamics of Low Reynolds Number High Angle of Attack Thin Plate Wings for Micro Air Vehicles," submitted to the Journal of Aircraft.

[146] Swanson, Taylor A., and Isaac, K. M., "The Effect of Camber on Force Generation in Leading Edge/Trailing Edge Switching Hovering Mode," AIAA 2009-4103.

[147] Taira, Kunihiko, and Colonius, Tim, "Three-Dimensional Flows Around Low-Aspect-Ratio Flat-Plate Wings at low Reynolds Numbers," Journal of Fluid Mechanics, v. 623, 2009, pp. 187-207.

[148] Tamai, M., Wang, Z., Rajagopalan, G., Hu, H., and He. G., "Aerodynamic Performance of a Corrugated Dragonfly Airfoil Compared with Smooth Airfoils at Low Reynolds Numbers," AIAA 2007-0483, Jan. 2007.

[149] Tang, Jian, Viieru, Dragos, and Shyy, Wei, "Effects of Reynolds Number and Flapping Kinematics on Hovering Aerodynamics," AIAA Journal, v. 46, n. 4, pp. 967-976, Apr. 2008.

[150] Tarascio, M. J., Ramasamy, M., Chopra, I., and Leishman, J. G., "Flow Visualization of Micro Air Vehicle Scaled Insect Based Flapping Wings," Journal of Aircraft, v. 42, n. 2, pp. 385-391, 2005.

[151] Taylor, G. K., Nudds, R. L., and Thomas, A. L. R., "Flying and Swimming Animals Cruise at a Strouhal Number Tuned for High Power Efficiency," Nature, vol. 425, pp. 707-711, 2003.

[152] Templin, R., "The Spectrum of Animal Flight - Insects to Pterosaurs," Progress in Aerospace Sciences, vol. 36, no. 5-6, pp. 393-436, 2000.

[153] Tobak, M. and Peake, D. J., "Topology of Three-Dimensional Separated Flows," Ann. Rev. Fluid Mech., v. 14, pp. 61-85, Jan. 1982.

[154] Tobalske, B. W., Hedrick, T. L., and Biewener, A. A., "Wing Kinematics of Avian Flight Across Speeds," Journal of Avian Biology, vol. 34, no. 2, pp. 177-184, 2003.

[155] Torres, G. E., and Mueller, T. J., "Aerodynamic Characteristics of Low Aspect Ratio Wings at Low Reynolds Numbers," in Fixed, Flapping, and Rotary Wing Aerodynamics for Micro Air Vehicle Applications, T. Mueller, ed., AIAA Prog. Astro. Aero. v. 195, 2001.

[156] Tuncer, Ismail H., and Platzer, Max F., "Computational Study of Flapping Airfoil Aerodynamics," Journal of Aircraft, v. 37, n. 3, May-Jun 2000, pp. 514-520.

[157] Tuncer, Ismail H., and Platzer, Max F., "Thrust Generation due to Airfoil Flapping," AIAA Journal, v. 34, n. 2, Feb 1996, pp. 324-331.

[158] Triantafyllou, M. S., Triantafyllou, G. S., and Gopalkrishnan, R., "Wake Mechanics for Thrust Generation in Oscillating Foils," Physics of Fluids A, vol. 3, no. 2, pp. 2835-2837, Dec. 1991.

[159] Usherwood, J. R., and Ellington, C. P., "The Aerodynamics of Revolving Wings I: Model Hawkmoth Wings," Journal of Experimental Biology, vol. 205, pp. 1547-1564, 2002.

[160] Usherwood, J. R., and Ellington, C. P., "The Aerodynamics of Revolving Wings II: Propeller Force Coefficients From Mayfly to Quail," Journal of Experimental Biology, vol. 205, pp. 1565-1576, 2002.

[161] Van Den Berg, Coen, and Ellington, Charles P., "The Three-Dimensional Leading-Edge Vortex of a 'Hovering' Model Hawkmoth," Philosophical Transactions of the Royal Society London Series B, v. 352, pp. 329-340, 1997.

[162] Vest, Michael S., and Katz, Joseph, "Unsteady Aerodynamic Model of Flapping Wings," AIAA Journal, v. 34, n. 7, Jul 1996, pp. 1435-1440.

[163] Viieru, D., Albertani, R., Shyy, W., and Ifju, P. G., "Effect of Tip Vortex on Wing Aerodynamics of Micro Air Vehicles," Journal of Aircraft, vol. 42, no. 6, pp. 1530-1536, 2005.

[164] von Ellenrieder, K. D., Parker, K., and Soria, J., "Flow Structures Behind a Heaving and Pitching Finite-Span Wing," Journal of Fluid Mechanics, v. 490, pp. 129-138, 2003.

[165] von Ellenrieder, K. D., Parker, K., and Soria, J., "Fluid Mechanics of Flapping Wings," Experimental Thermal and Fluid Sciences, v. 32, 2008, pp. 1578-1589.

[166] von Karman, T., and Burgers, J. M., "Problems of non-Uniform and of Curvilinear Motion," in Aerodynamic Theory: A General Review of Progress, v. 2: General Aerodynamic Theory, Perfect Fluids, ed. W. F. Durand, pp. 304-310, Springer, 1935.

[167] Wakeling, J. M., and Ellington, C. P., "Dragonfly Flight I: Gliding Flight and Steady-State Aerodynamic Forces," Journal of Experimental Biology, vol. 200, pp. 543-556, 1997.

[168] Wang, Z. J., “Dissecting Insect Flight,” Annual Review of Fluid Mechanics, vol. 37, pp. 183-210, 2005.

[169] Wang, Z. J., “Vortex Shedding and Frequency Selection in Flapping Flight,” Journal of Fluid Mechanics, vol. 410, pp. 323-341, 2000.

[170] Wang, Z. J., Birch, J. M., and Dickinson, M. H., “Unsteady Forces and Flows in Low Reynolds Number Hovering Flight: Two-Dimensional Computations vs. Robotic Wing Experiments,” Journal of Experimental Biology, vol. 207, pp. 449-460, 2004.

[171] Warrick, D. R., Tobalske, B. W., and Powers, D. R., “Aerodynamics of the Hovering Hummingbird,” Nature, vol. 435, no. 23, June 2005, pp. 1094-1097.

[172] Weis-Fogh, Torkel, “Quick Estimates of Flight Fitness in Hovering Animals, Including Novel Mechanisms for Lift Production,” Journal of Experimental Biology, vol. 59, pp. 169-230, 1973.

[173] White, Frank, "Viscous Fluid Flow," 3rd ed., McGraw Hill, 2005.

[174] Williams, M. H., “Exact Solutions in Oscillating Airfoil Theory,” AIAA Journal, v. 15, n. 6, Jun 1977, pp. 875-877.

[175] Willert, C. E., and Gharib, M., “Digital Particle Image Velocimetry,” Experiments in Fluids, v. 10, pp. 181-193, 1991.

[176] Wilson, J. R., “Mini Technologies for Major Impact,” Aerospace America, vol. 36, no. 5, pp. 36-38, 41, 42, May 1998.

[177] Yavuz, M. M. and Rockwell, D., “Control of Flow Structure on Delta Wing with Steady Trailing-Edge Blowing,” AIAA Journal, v. 44, n. 3, pp. 493-501, Mar. 2006.

[178] Yen, S. C., and Hsu, C. M., “Flow Patterns and Wake Structure of a Swept-Back Wing,” AIAA Journal, v. 45, n. 1, pp. 228-236, Jan, 2007.

[179] Young, John, and Lai, Joseph C. S., “Mechanisms Influencing the Efficiency of Oscillating Airfoil Propulsion,” AIAA Journal, v. 45, n. 7, July 2007, pp. 1695-1702.

[180] Young, J., and Lai, J. C. S., "Oscillation Frequency and Amplitude Effects on the Wake of a Plunging Airfoil," AIAA Journal, v. 42, n. 10, Oct 2004, pp. 2042-2052.

[181] Young, John, and Lai, Joseph C. S., “Vortex Lock-In Phenomenon in the Wake of a Plunging Airfoil,” AIAA Journal, v. 45, n. 2, Feb 2007, pp. 485-490.

[182] Young, J., Lai, J. C. S., and Germain, C., "Simulation and Parameter Variation of Flapping-Wing Motion Based on Dragonfly Hovering," AIAA Journal, v. 46, n. 4, pp. 918-924, Apr 2008.

[183] Young, Larry A., Pisanich, Greg, and Ippolito, Corey; “Aerial Explorers,” AIAA Paper 2005-0912.

VITA

Taylor Alexander Swanson was born June 11, 1981. He earned a Bachelor of Science with honors in Aerospace Engineering from Iowa State University in 2003. While there, he was a member of the AIAA and served on its cabinet, was a member of the university honors program and Phi Kappa Phi honors society, and was president of the Iowa State University chapter of the aerospace engineering honors society, Sigma Gamma Tau. In May 2006, he earned a Master of Science in Aeronautical and Astronautical Engineering from the University of Illinois, Urbana. While there, he worked as a research assistant and a teaching assistant. His thesis was titled "Interaction of Laser Energy Deposition with a Normal Shock," and was advised by Prof. Gregory Elliott. Following this, he attended Missouri University of Science and Technology funded as a teaching assistant, with a Chancellor's Fellowship, and by the NASA Missouri Space Grant. His Doctor of Philosophy in Aerospace Engineering from the Missouri University of Science and Technology was earned in August, 2009. The dissertation title was "An Experimental and Numerical Investigation of Flapping and Plunging Wings," and was advised by Prof. K. M. Isaac.